Remote focusing to follow action potential transmurally in acute rabbit cardiac slices

Giedrė Astrauskaitė

Submitted in fulfilment of the requirements for the Degree of Doctor of Philosophy

University of Glasgow
College of Science and Engineering
School of Physics and Astronomy

June, 2025

Abstract

Electrical signals or action potentials (APs) originate in the pacemaker cells of the heart and travel through the organ in an orchestrated fashion. This electrical conduction governs mechanical contraction, making the heart an efficient pump. During a myocardial infarction (MI), oxygen deprived cardiac cells are rendered electrically inert as the scar is formed. This impairs the natural conduction pathways and can lead to life-threatening arrythmias. Therefore, understanding AP propagation in relation to the complex 3-dimensional tissue morphology of healthy and infarcted animal models is a pivotal step to establish diagnostic and therapeutic tools.

To indirectly investigate cardiac electrophysiology in large-scale intact tissue, optical mapping with voltage sensitive dyes (VSDs) is commonly employed [1]. Nevertheless, AP propagation in distinct cellular layers in depth below the epicardium is inaccessible with optical mapping. Conversely, two-photon fluorescence microscopy (2PM) allows cellular resolution and large tissue penetration depth with inherent optical sectioning [2]. In the ventricular wall of the heart, two directions of conduction can be considered: longitudinal, along the long axis of the cell and transmural, from the endocardium to the epicardium. Along the long axis of the cardiomyocytes, with 2PM, action potentials have previously been resolved as deep as 500 µm in distinct cellular layers of Langendorff-perfused rabbit hearts [3]. However, conventional microscopes cannot facilitate axial scanning fast enough to resolve action potentials and therefore transmural cardiac conduction has not yet been investigated with 2PM.

In remote refocusing (RF), a remote objective and a lightweight mirror in its focal plane are introduced in the optical system [4, 5]. Consequently, the 3-dimensional optical copy of the sample can be probed vertically by rapid remote mirror actuation. RF is compatible with high numerical aperture 2PM systems and offers the temporal resolution necessary to resolve transmural action potential propagation over a large refocusing range [4, 5]. Studies employing RF in multiphoton microscopes focus predominantly on deep tissue neural function [6, 7]. Nevertheless, the brain is significantly less scattering compared to cardiac preparations. Sarcomere length of cardiomyocytes was measured utilising RF, but only cardiac structure, not electrical function was investigated [8].

Therefore, the aim of this work is, firstly, to develop a 2-photon microscope system enhanced with RF for rapid axial scanning and capable of probing action potential propagation along both longitudinal and transmural directions within deep myocardium. Our implementation of a remote refocusing module retrofitted to a commercial Scientifica 2-photon microscope achieves 250 Hz axial scanning over a range of 100 µm while maintaining under 5 µm axial resolution. The necessary system power efficiency and dispersion optimisation [9] is discussed: 22 mW average power with 15.9% throughput and a close to transform-limited pulse duration of 156 fs at sample is allowed by the system. Secondly, the full experimental pipeline including the preparation, viability evaluation and imaging of the cardiac preparation is established. Acute rabbit ventricular slice model adapted from [10] and prepared from hearts that have previously been used for other experiments (in line with the University's strategy for reduction of animal research [11]) was tailored for 2P-RF imaging at room temperature. Live-dead staining (triphenyl tetrazolium chloride) of N=6 slices revealed no hypoxic core and gave a qualitative verification of slice viability in the central region of the preparations; slice contractility and action potential properties were characterised with optical mapping (CellOPTIQ system). The slices exhibit single-peak contractile traces throughout the entire preparation when stimulated at 0.3 Hz. Furthermore, in N=6 slices, the action potential duration was approximately 2 times shorter after increasing the concentration (from 15 mM to 30 mM) of 2,3-butanedione monoxime (BDM), an electromechanical uncoupler necessary for 2-photon imaging. The variation of AP duration from slice to slice at 30 mM BDM was characterised. Finally, the preliminary data to validate the use of our 2P-remote focusing to investigate cardiac AP propagation transmurally is presented. The time to acquire z-y planes in myocardium is reduced from minutes (conventional z-stack acquisition) to seconds with 122 Hz RF. When the remote refocusing module is bypassed, we resolve AP traces in electrically stimulated slices with rapid longitudinal galvanometric mirror scanning with SNR > 7 over the range of 120 µm in depth. Importantly, with the RF unit in place, action potential peaks were visible over approximately 60 µm range with static remote refocusing with SNR > 4. Therefore, we believe that the 2P-RF system presented will allow to resolve transmural APs with rapid axial scanning and enable a quantitative investigation how scar tissue impacts cardiac conduction in post-MI preparations.

Thesis overview and contributions

The contribution and significance of each chapter is outlined in the following summary. A publication based on Chapters 3-6 is in preparation, with an intention to obtain the final result (2P-RF dynamic transmural cardiac action potential imaging) within the following months.

Chapter 3

A custom optical system to facilitate remote focusing [5] was designed, assembled, aligned and integrated with a commercial 2-photon microscope. The system's optical performance was characterised and the microscope was optimised for functional imaging in highly scattering cardiac tissue. Costing just over approximately £9000 in off the shelf parts, this RF system substantially expands the imaging capabilities of the microscope and adds to the sparse literature of remote refocusing in non-linear microscopy.

Chapter 4

A protocol for preparation of acute rabbit cardiac slice model modified from [10] was established together with the pipeline for quality and viability assurance. The model was prepared from re-used rabbit hearts in accordance with the University's mitigation and refinement strategy on animal research [11] and tailored to be compatible with the imaging system (Chapter 3). As acute slices could still be obtained and characterised, the cardiac tissue that would otherwise be discarded can realistically enter another quantitative experimental pipeline, mitigating the number of research animals sacrificed. The optimised acute slice model is now embedded in the research group and will be employed in experimental protocols going forward.

Chapter 5

Fast structural imaging of acute cardiac slices (Chapter 4) under the 2-photon remote focusing microscope (Chapter 3) was facilitated, demonstrating reduced imaging time (compared to traditional scanning) required to obtain information on 3D sample structure. These proof-of-principle measurements underlined the functionality of the RF implementation in a highly scattering cardiac tissue sample.

Chapter 6

Combining the work from Chapters 3 and 4, the 2-photon remote focusing microscope was used to probe electrophysiology of electrically stimulated acute rabbit cardiac slices. Conventional galvanometric mirror line scanning allowed visualising action potential traces from deep tissue layers. When RF optics were included for static refocusing, AP signals were detected with longitudinal line scanning, albeit at a deteriorated signal-to-noise-ratio. Remote focusing modality was used to image action potential propagation transmurally, yielding a negative result. In Chapter 7, potential system and experimental protocol optimisation to allow transmural RF AP imaging is presented.

Publications and Presentations

Conference proceedings

1. **G. Astrauskaitė**, L. Williamson, S. Mohanan, S. M. Moreno, R. Kinegawa, E. Boland, E. Huethorst, G. Smith, and C. Müllenbroich, *"Fast Axial Scanning with Remote Focusing for Multiphoton Microscopy of Acute Rabbit Ventricular Slices to Follow Action Potentials Transmurally"*, in CLEO 2024, Technical Digest Series (Optica Publishing Group, 2024), paper SF2B.1. Oral presentation by Dr. Müllenbroich and manuscript.

2. **G. Astrauskaitė**, S. Mohanan, L. Williamson, E. Boland, E. Huethorst, R. Kinegawa, G. Smith, and C. Müllenbroich, *"Remote focusing for 2-photon microscopy to follow action potential propagation transmurally in acute rabbit cardiac slices"*, in: SPIE BiOS 2024, San Francisco, CA, USA, 27 January - 1 February 2024. Poster presentation and manuscript.

Presentations

1. **G. Astrauskaitė**, S. M. Moreno, S. Mohanan, L. Williamson, E. Boland, E. Huethorst, G. Smith, C. Müllenbroich, *"Resolving action potentials in acute rabbit cardiac slices with 2-photon remote focusing microscopy."* Oral presentation in Biophotonics IV, Photon, Institute of Physics, Swansea, 2024 September.

2. **G. Astrauskaitė**, S. Mohanan, L. Williamson, E. Boland, E. Huethorst, R. Kinegawa, G. Smith, C. Müllenbroich, *"Building a compact remote focusing module for a commercial 2-photon microscope: challenges and opportunities for cardiac imaging."* Oral Presentation in Glasgow Imaging Network Meeting, 2023 December.

3. **G. Astrauskaitė**, S. Mohanan, L. Williamson, E. Boland, E. Huethorst, R. Kinegawa, G. Smith, C. Müllenbroich, *"Remote focusing for 2-photon microscopy*

to follow action potential propagation transmurally in acute rabbit heart slices." Oral Presentation in Scottish Microscopy Symposium, Dundee, 2023 November.

Declaration

I declare that all work described in this Thesis which is not my own is appropriately identified and attributed to the respective authors. Furthermore, any material that has previously been submitted and approved for the award of a degree by this or any other University has been acknowledged.

The work presented in this Thesis is my own except for the following:

1. In Chapter 3, the single prism compressor was built together with another post-graduate researcher (PGR), Lewis Williamson. The results for pulse duration across the set-up with the custom in-line autocorrelator were obtained by Lewis Williamson entirely and are stated in this Thesis for completeness only (Section 3.6.1).

2. In Chapter 4, the animal sacrifice is performed by John MacAbney, a certified laboratory technician. Dr Erin Boland performed tissue staining with FluoVolt dye on a Langendorff-perfusion rig (Section 4.2.1). The solutions required for the cardiac slicing protocol were prepared by a PGR, Steven M. Moreno (Section 4.2.2), who also assisted me during the slicing itself. CellOPTIQ imaging of acute slices was facilitated by me together with Dr Eline Huethorst (Sections 4.3.4 and 4.3.5).

This Thesis is available for the Library on the understanding that it is copyright material and that no quotation from the Thesis may be published without proper acknowledgement.

Giedrė Astrauskaitė, December 2024

Contents

List of Figures

List of Tables

Chapter 1

Introduction

1.1 Multiphoton microscopy

Fluorescence microscopy has revolutionised biological imaging and is among the gold standard methods in fields including neuroscience and cancer research. Development of multiphoton systems allowed to further enhance the penetration depth and resolution at which the preparations can be investigated. In the following section, the fundamentals of single and multiphoton fluorescence excitation and how this process is utilised as contrast mechanism in microscope systems to probe biological sample structure and importantly, biochemical function is discussed. The advantages and requirements of multiphoton fluorescence microscopes are explained. Additionally, fundamental properties of microscopes such as resolution and aberrations are outlined together with the limitations of multiphoton fluorescence microscopes in terms of fast 3D imaging.

1.1.1 Fluorescence

Fluorescence is a process where light is absorbed by a molecule and after some non-radiative energy loss (phonon) a longer wavelength, less energetic photon is emitted as the molecule relaxes. A Jablonski diagram illustrating this is shown in Figure 1.1.

Consider a simplified molecule model with ground (S_0) and excited state ($S_{1,2}$) energy level bands. If these states are separated by some transitional energy ΔE, then to excite the molecule through absorption of light, a photon of energy

$$\Delta \mathrm{E} = h\nu$$

is required, where ν is its frequency and h is Planck's constant. This is a very fast process that occurs in femtosecond ($\sim 10^{-15}$s) timescales. Complex molecules in solutions typically have their excited and ground states broadened to a band of sub-levels associated with vibrational energy states. Therefore there is a range of frequencies

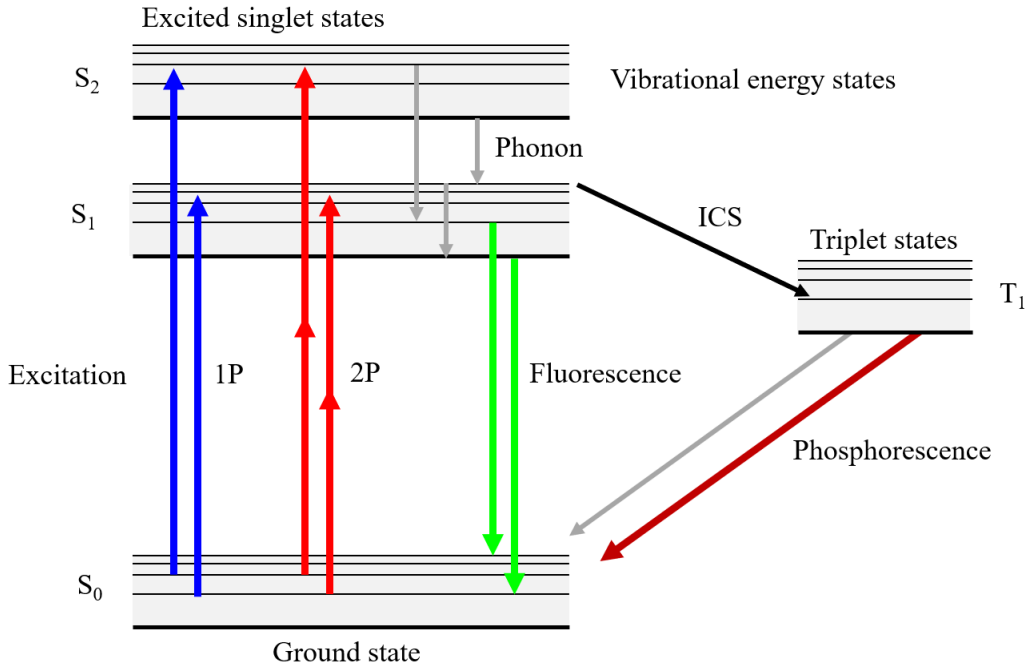

Figure 1.1: Jablonski diagram illustrating a three level model of a molecule and its interaction with light. The molecule can be excited from the ground state to the excited state by single (blue, 1P) or two (red, 2P) photon absorption. Non-radiative transitions are marked in grey. ICS stands for intersystem crossing. *Adapted from* [12].

that can be associated with the excitation and the absorption cross section (σ_a), which denotes the wavelength dependent likelihood for the photon to be absorbed. Note that if the conditions are right (further discussed in Section 1.1.3), the aforementioned excitation process can occur with two photons of frequency ν_2, where $\nu = 2\nu_2$. Once in the excited state, the molecule loses some of its energy through a non-radiative decay S_2 to S_1 ($\sim 10^{-14} - 10^{-11}$s). As the molecule further decays to the ground state from S_1 to S_0, a fluorescence photon is emitted in the timescale of nanoseconds. The fluorescence power emitted by the molecule can be written as a linear relationship

$$\Phi_{\mathrm{f}} = \mathrm{q}\sigma_{\mathrm{a}}\mathrm{I},$$

where I is the illumination intensity, q is the quantum yield or the efficiency of fluorescence emission given that the absorption has happened and σ_a is the absorption cross section. The energy difference between excitation and emission is called the Stokes shift [12] and allows spectral separation of the two, making fluorescence a useful contrast mechanism for imaging and microscopy.

While the full description is out of scope of this discussion, a more detailed model considers also the excited triplet state T_1. Through intersystem crossing, the molecule can end up in the triplet band. A radiative relaxation (phosphorescence) can then occur, although most transtitions from this state are non-radiative. It is called delayed

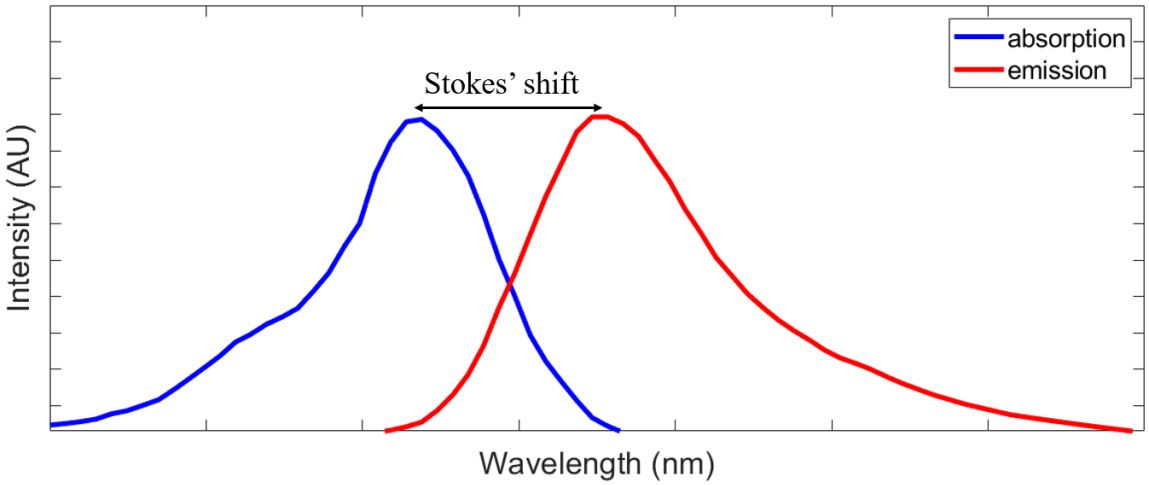

Figure 1.2: Stoke's shift describes the difference in wavelength of absorbed excitation and emitted fluorescence photons. *Adapted from* [12].

fluorescence, due to its long timescales ($\sim 10^{-3} - 10^{2}$s). The triplet state pathway of relaxation is alternative to fluorescence emission, in effect temporarily switching it off. On the other hand, photobleaching (or the destruction of the fluorophore) ends the molecule's ability to fluoresce permanently and is caused by illuminating the sample for a prolonged period of time or at higher light intensities. Because it is irreversible, photobleaching is a pertinent issue, especially in samples with weak fluorescence excitation or emission. For a mathematical description of molecular energy transitions involving the aforementioned processes, the interested reader should refer to [12].

1.1.2 Fluorescence microscopy

While the first fluorescence microscope was implemented by O. Heimstädt and H. Lehmann in the early 20th century, in the present day this method constitutes a significant branch of light microscopy. Specific cell groups or structural parts of cells such as the nuclei or plasma membranes can be labelled with fluorescent dyes through protein, enzymatic or genetic tagging. An example of a common dye is the lectin Wheat germ agglutinin, which labels the cellular membrane, conjugated with Alexa Fluor fluorophores of desired excitation and emission wavelengths. In addition to revealing structure of the sample, fluorescence microscopy also allows probing biochemical function, as the intensity of fluorescent reporters can be altered or even "switched on" during specific processes. For example, Fluovolt dye allows visualising the change of voltage across a cell membrane in cardiac muscle or neural electrical signaling (further discussed in Section 4.1.1).

As the excitation and emission light is of a different wavelength, a basic epifluo-

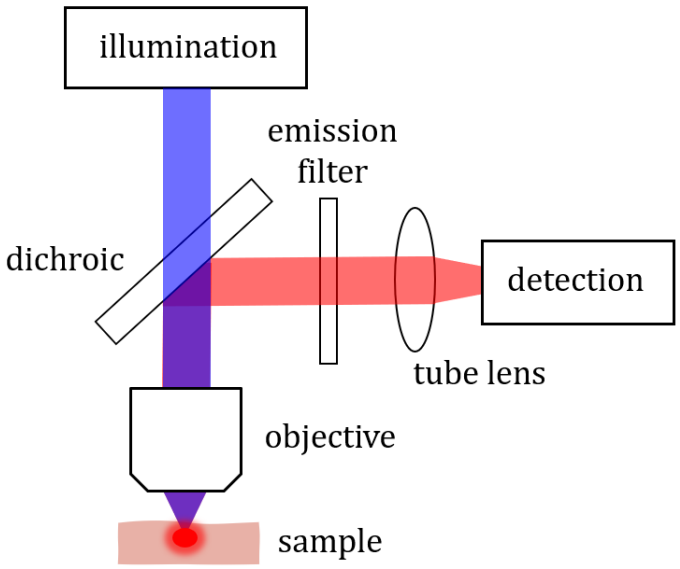

Figure 1.3: Schematic of a basic fluorescence microscope. The illumination from a laser or LED is focused on the sample. Note that in the case of LED illumination, an excitation filter is required. The generated fluorescence is collected through the same objective and focused on the detector.

rescence widefield microscope can be assembled (Figure 1.3). The light source is a continuous wave laser or a light emitting diode (LED). In epi-illumination both the excitation and emission light are on the same side of the specimen, as opposed to the in-transmission imaging scheme (fluorescence is collected with a different objective after the sample). This allows detecting low fluorescence photon fluxes that undergo scattering or are absorbed in transmission. The emitted fluorescence is reflected by the dichroic mirror and focused on the detector (e.g. a CMOS camera). An emission filter before the detection is placed to eliminate residual excitation light leakage or target a specific emission spectral range. The drawback of this method is the degradation of resolution due to the amount of fluorescence generated and collected from regions outside the focal plane. Additionally, no depth-specific information is available. Confocal microscopy tackles this issue by introducing a pinhole in the detection path. The pinhole is positioned in the plane conjugate to the focal plane at the sample, rejecting the light rays originating from outside this plane. This yields enhanced resolution and optical sectioning, however, a significant portion of emitted fluorescence is lost.

1.1.3 Multiphoton fluorescence microscopy

Although sub-cellular resolution imaging of biochemical dynamics within living preparations can be achieved with conventional fluorescence microscopy [13], and confocal method allows further improvements and optical sectioning, in both the fluorophores

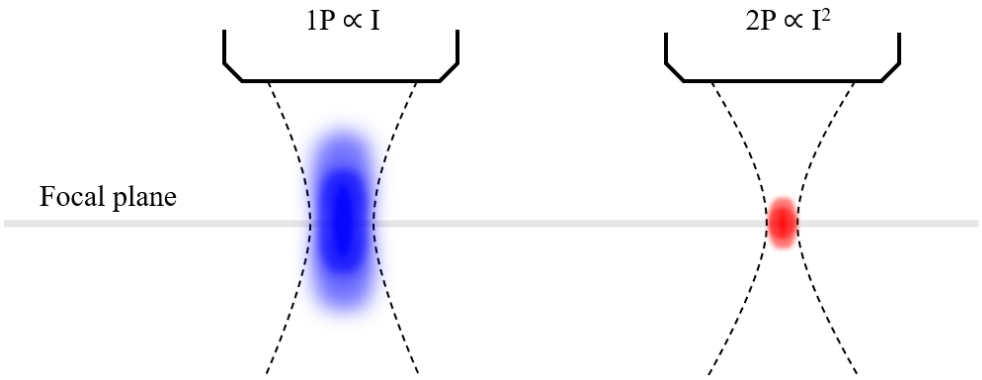

Figure 1.4: Difference in fluorescence excitation area in 1- and 2-photon absorption processes (left and right, respectively). Because 2-photon absorption probability scales nonlinearly with pump light intensity, excited fluorescence is confined within the focal volume.

are still excited and photobleached outside the focal volume. A more advanced imaging scheme is multiphoton microscopy, where two or more photons of the same longer wavelength are absorbed simultaneously as one to generate fluorescence (with a potential to photobleach) within a much smaller focal volume. For the purpose of this thesis, the discussion will be centered around 2-photon fluorescence microscopy (2PM). The interested reader should refer to [14] for description of 3-photon systems.

Two photon absorption was first theorised by Marie Göeppert Mayer in 1931 [15]. However, as the photons need to be confined both spatially and temporally to very high densities, only the invention of laser sources allowed 2-photon absorption to be experimentally realised 3 decades later [16]. The first 2PM images were reported by W.Denk, J.Strickler and W.Webb in 1990 [17]. Since then, 2-photon microscopes were further developed, commercialised and became a gold standard of imaging in biosciences. For example, 2PM was used to probe cardiac electrical signal dynamics in intact murine and rabbit heart preparations [3] and investigate spiking activity across large neuronal populations in awake behaving mice [18].

As 2-photon absorption is a nonlinear process, the generated fluorescence power scales quadratically with excitation light intensity as

$$\Phi = \sigma_{2\mathrm{f}} \mathrm{I}^2$$

where σ_{2f} is the two photon excited fluorescence cross section. Because of its nonlinear nature, this process is inefficient at low intensities. To generate sufficient signal, a high degree of spatiotemporal confinement of excitation photons is essential. As a result, 2-photon fluorescence only originates in the focal volume where the optical power density is the highest (Figure 1.4), yielding inherent optical sectioning without the need for a detection pinhole. This is particularly beneficial, as depth-specific information

within the sample can be accessed without any loss of light in the detection optics, with simultaneously reduced background and suppressed photobleaching. The excited fluorescence that scatters can also be collected, increasing the available signal, which is a significant advantage of 2-photon microscopy compared to confocal microscopy. Importantly, as longer near infrared (NIR) wavelengths used for excitation are less susceptible to scattering in biological tissue, the penetration depth is enhanced [19, 20].

Requirements for 2-photon microscopy

Requirements for the implementation of 2P microscopes are stricter compared to 1P. Even with high numerical aperture (NA) focusing, continuous wave lasers would not generate sufficient power densities. Ultrafast mode-locked laser sources are used for 2PM with pulse durations in the range of 100-150 fs at high repetition rates (around 100 MHz) [17]. The use of intense femtosecond pulses at high repetition rates allows imaging at biologically tolerable power levels, which can be in the range of tens of mW, although this is highly sample and focal spot size dependent. Nevertheless, this makes 2PM susceptible to dispersion induced pulse broadening, further discussed in Section 1.1.3 and many 2PM lasers employ inbuilt dispersion compensation. 2PM laser sources also tend to have a tunable wavelength range to cover the excitation range of commonly used fluorophores. For example, Titanium:Sapphire lasers can produce wavelengths from 700 nm to 1050 nm. Due to losses in microscope systems, 2PM lasers generally have average power outputs of at least 1 W. Evidently, the need for such light sources increases the complexity and cost of the microscope.

Because high NA objectives are used, the lateral dimensions of the cross-sectional area of the point spread function can be sub-micron with 2PM, while the focal volume dimensions are in the range of some cubic micrometers. To form an image, 2P microscopes are generally point scanning, as shown in Figure 1.5, where scanning is achieved with actuated galvanometric mirrors. Photomultiplier tubes (PMTs) are generally the detectors of choice due to their large dynamic range and high quantum efficiency. Furthermore, PMTs allow collecting as many emitted fluorescence photons as possible, regardless of their exact origin. Detection can be descanned, where the light passes through the scanning mirrors or whole area, where the detector is sensitive to emitted light from the entire image area at all times. Whole area detection employs a dichroic mirror and is more efficient than descanned detection as it avoids the optical losses by minimising the number of optical surfaces in the beam path. It should be noted that PMTs are prone to noise from ambient background light as well as the Poissonian shot noise [20].

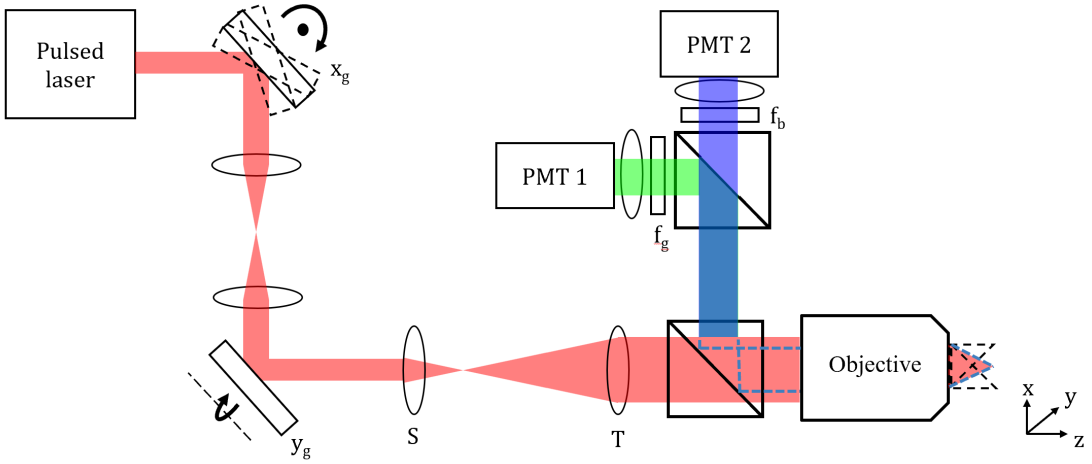

Figure 1.5: A schematic diagram of a conventional point scanning two photon microscope, employing two rotating galvo mirrors and a two channel detection. S and T are scan and tube lenses, respectively. After the excitation-emission dichroic, the blue and green bands are split. Filters f_b and f_g are used to isolate the desired colours and the light is focused onto the PMTs.

Dispersion of optical pulses

As dispersion broadens optical pulses in time and thus decreases fluorescence excitation efficiency, its management is critical in multiphoton microscopy. In the following section the fundamental concepts of pulse dispersion are introduced; for a more rigorous mathematical treatment, the interested reader should refer to [21, 22]. The pulse duration is inversely proportional to its spectral bandwidth; an optical pulse can be interpreted as a superposition of different frequency components, the interference of which results in the formation of the pulse. The shortest pulse than can be achieved for a given spectral bandwidth is called transform-limited.

The refractive index n describes how much the speed of light (v) of a certain frequency (or wavelength) slows down in a given material compared to its speed in vacuum (c):

$$\mathrm{v}(\omega) = \frac{\mathrm{c}}{\mathrm{n}(\omega)}.$$

Chromatic dispersion occurs in optical materials where the phase velocity (the speed of each of the frequency component within the optical pulse) and group velocity (the speed of the propagation of the pulse envelo pe)depend on its wavelength, which is largely a result of the interaction of light with electrons of the medium. For longer optical pulses (in the range of nanoseconds) dispersion effects can be neglected, as the wavelength bandwidth forming the pulse is narrow; ultrashort pulses are inherently susceptible to dispersion due to their broad spectral bandwidth. Consider a Gaussian pulse, the propagation of which through a medium can be described as

$$\mathrm{E(t)} = \frac{1}{\sqrt{2\pi}} \int \varepsilon(\omega) \exp^{\mathrm{i}(\omega \mathrm{t} + \phi(\omega))} \, \mathrm{d}\omega,$$

where $\phi(\omega)$ is the spectral phase and $\varepsilon(\omega)$ describes how much of that frequency is present in the pulse. Taylor expansion of $\phi(\omega)$ yields

$$\phi(\omega) = \phi(\omega_0) + \left.\frac{\partial \phi}{\partial \omega}\right|_{\omega=\omega_0} (\omega - \omega_0) + \frac{1}{2} \left.\frac{\partial^2 \phi}{\partial \omega^2}\right|_{\omega=\omega_0} (\omega - \omega_0)^2 + ... \tag{1.1}$$

The carrier-envelope phase or the phase difference between the central wavelength of the pulse and the carrier wave is described by the $\phi(\omega_0)$ term in Equation 1.1 [21]. The first order term $\frac{\partial \phi}{\partial \omega}$ is the group delay or the propagation time of the pulse envelope through the optical material. For distance L, the group velocity v_g of the pulse envelope can be defined. Individual spectral components within the pulse propagate at their own phase velocity v_p. In idealised situations (vacuum), group velocity dispersion (GVD, units of $\mathrm{fs}^2/\mathrm{mm}$) is 0, thus $v_p = v_g$ and the wavelength components of the pulse travel at the same velocity, rendering the temporal pulse shape constant. For most transparent solids, $v_p > v_g$, resulting in change of pulse duration. The second order term $\frac{\partial^2 \phi}{\partial \omega^2}$ is the group delay dispersion (GDD) (units of fs^2). This term denotes that difference between spectral components components depends on frequency. GDD can be calculated considering the GVD accumulated for some length L travelled in the dispersive medium:

$$\mathrm{GDD} = \mathrm{GVD} \times \mathrm{L}. \tag{1.2}$$

Higher order terms (third order dispersion) are not significant in pulses used in 2PM. While chromatic dispersion in air is negligible, when pulses propagate through optical components, they acquire positive GDD and are broadened in time, as shown in Figure 1.6. Due to the dependency of the refractive index on the frequency of light, the low frequency (red) components of the pulse arrive before the high-frequency (blue) components; the pulse is therefore broadened in time and chirped. The frequency increases throughout laser pulses that are positively chirped, as the lower frequencies arrive earlier in time. The opposite is true for negatively chirped pulses [21]. To compensate for these effects, negative dispersion needs to be introduced. If inbuilt laser dispersion compensation is insufficient, this can be achieved by external pulse compressors that utilise angular dispersion of optical gratings and prisms.

1.1.4 Imaging properties of fluorescence microscopes

In the following section the properties that characterise the performance of both single- and multi- photon fluorescence microscopes, namely the optical resolution and its

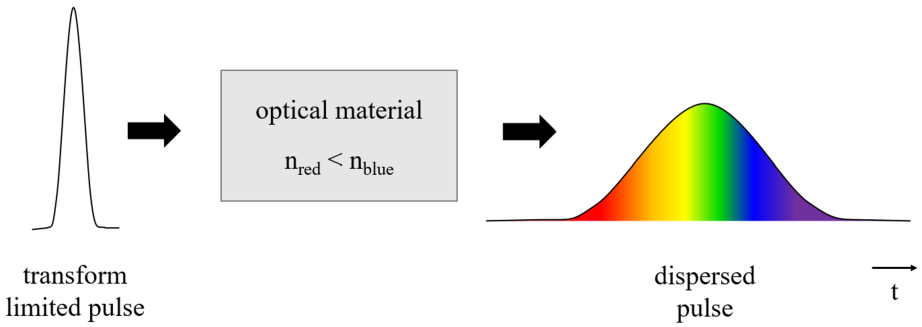

Figure 1.6: Positive dispersion of optical pulses due to propagation through optical materials (e.g., optical glasses or crystals). The pulse is stretched temporally as shorter wavelength components traverse the media at slower velocity.

degradation due to aberrations, are described.

Resolution

A perfect imaging system would produce an exact copy of a point object in the object space at a given image plane. However, the wave nature of light implies that it is subject to diffraction effects. Light waves diffract as they encounter apertures, such as a circular aperture of a lens or an objective. This yields an Airy disk pattern at the imaging plane comprised of a bright centre and a series of cocentric rings of decreasing intensity. The Airy disk imposes a limit on how small the focal spot of the microscope objective can be. In other words, it defines the diffraction-limited resolution of the imaging system and how will diffraction affect the image of an ideal point object produced by the optical system. Figure 1.7 illustrates this effect. The diameter of the Airy disk depends on the wavelength of the light (λ), the size of the aperture (D) and the focal length (f):

$$\mathrm{W_{Airy}} = \frac{2.44\mathrm{f}\lambda}{\mathrm{D}}.$$

Note that N is the f-number of the lens given by the ratio of the focal length f to the diameter of the entrance pupil D. As $\frac{f}{D} = N = \frac{1}{2NA}$ for well corrected objectives,

$$\mathrm{W_{Airy}} = \frac{1.22\lambda}{\mathrm{NA}}.$$

It follows that with increasing wavelength the resolution decreases. When considering fluorescence microscopy, different features of the sample could be assumed to be incoherent luminescent point sources. Each of them will therefore be subject to this resolution limit. For self-luminous objects, the Rayleigh criterion denotes the distance between the central maxima and first minima in the diffraction pattern as the minimum

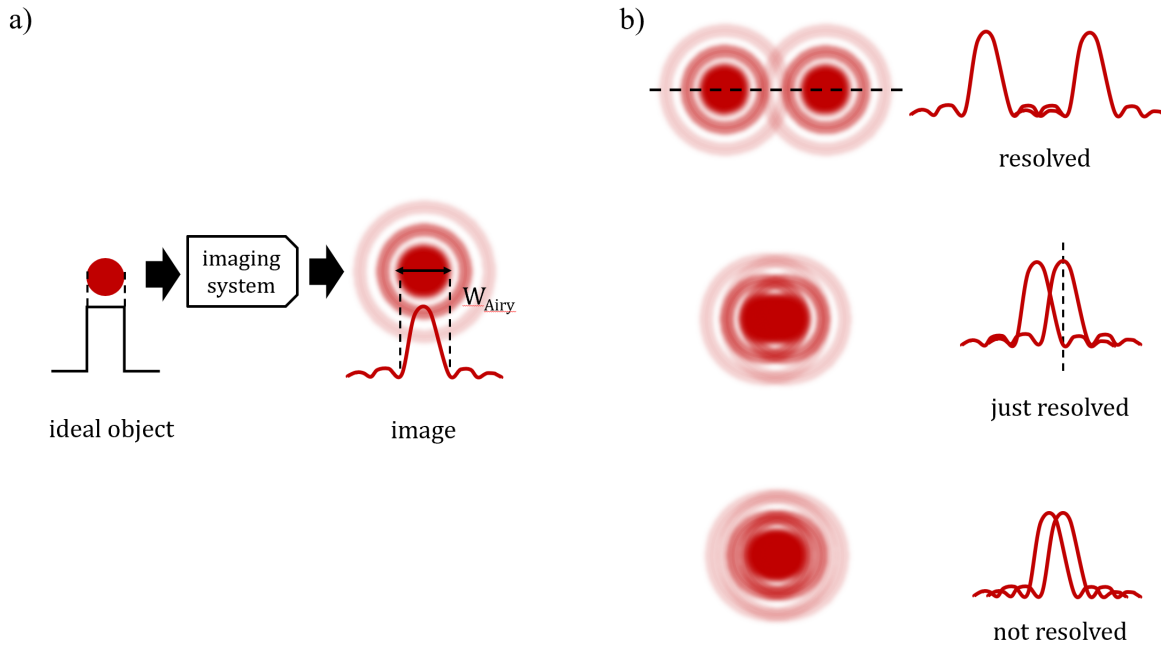

Figure 1.7: Diffraction limited response of imaging. a) An ideal point source profile is imaged as an airy disk. b) Two objects can be distinguished by the imaging system if the resulting diffraction patterns are separated. When the peak of one resulting airy disk coincides with a minima of another, they are considered to be just resolved. Moving the objects closer together would make them undistinguishable to the imaging system.

resolvable distance

$$W_{Airy} = \frac{0.61\lambda}{NA}$$

while the axial depth of field is written as

$$DOF = \frac{2n\lambda}{NA^2},$$

where n is the refractive index. If fluorescence excitation wavelength is $\lambda = 800\,\text{nm}$, the NA 1 and the objective is water immersion, we get diffraction limited lateral and axial resolutions of 488 nm and 2.128 µm, respectively. Note that this is true only in idealised circumstances in aberration free systems. Additionally, it is assumed that the pupil of the objective is uniformly illuminated. This is not the case for laser beams as they have a Gaussian intensity profile. A common solution is to overfill the back aperture by expanding the beam to approximate uniform illumination.

It would seem that two times longer excitation wavelength in 2PM worsens the resolution twice. While true in single photon systems, in 2PM this effect is outweighed by suppressing out-of-focus fluorescence and robustness to scattering [2]. Consider a focused optical system. The point spread function (PSF) is effectively the instrument

response function, as it defines how the system images an idealised point object. As described in Webb et al. (2003), the 2P illumination PSF, $\mathrm{IPSF}^2(\mathrm{x},\mathrm{y},\mathrm{z})$, denotes intensity in the excitation focal volume, which is enough to estimate the effective 2PM lateral

$$\mathrm{FWHM}_{x,y} = \begin{cases} \frac{0.320\lambda}{\sqrt{2}\mathrm{NA}} 2\sqrt{\ln 2}, & \text{if NA} \leq 0.7 \\ \frac{0.325\lambda}{\sqrt{2}\mathrm{NA}^{0.91}} 2\sqrt{\ln 2}, & \text{if NA} > 0.7 \end{cases} \tag{1.3}$$

and axial

$$\mathrm{FWHM}_z = \frac{0.532\lambda}{\sqrt{2}} \left(\frac{2\sqrt{\ln 2}}{n - \sqrt{n^2 - \mathrm{NA}^2}} \right) \tag{1.4}$$

resolutions. The change in resolution with different wavelength and NA of the objective calculated using Equations 1.3 and 1.4 is shown in Figure 1.8. Note that the back aperture of the objective needs to be overfilled to achieve optimum resolution. Additionally, deviations from this estimate can occur depending on the cross section of the fluorophore or laser power [2]. For example, with fluorophores of a relatively high 2-photon cross section, for sufficiently high powers, the probability of 2P excitation at the centre of the focal volume becomes 1 and saturates. Increasing the power increases the probability towards the edges of the focal volume, thus broadening the FWHM (full width at half maximum) of PSF (point spread function) overall [2].

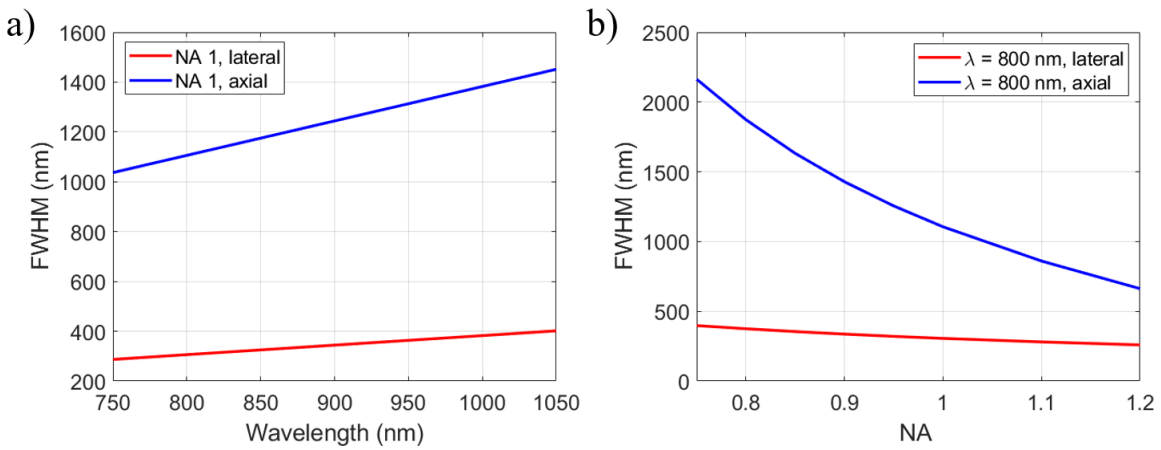

Figure 1.8: 2PM resolution change with different wavelength (a) and numerical aperture (b) for water immersion objectives. Axial resolution is more sensitive to λ or NA changes.

Aberrations

In the paraxial approximation light propagation through the optical system is described with an assumption that all the rays travel at a small angle φ with the optical axis. Therefore, it can be written that

$$\cos\varphi \approx 1, \qquad \sin\varphi \approx \varphi, \qquad \tan\varphi \approx \varphi. \tag{1.5}$$

This small angle approximation is used in first order ray tracing, but as the rays deviate from the axis at larger angles it becomes less accurate. The paraxial model cannot describe aberrations which cause the focal spot to be smeared out over some region in the image plane. This is particularly relevant for high-magnification microscope objectives.

If the approximations in Equations 1.5 no longer hold, the Taylor series expansion

$$\sin\varphi = \varphi - \frac{\varphi^3}{3!} + \frac{\varphi^5}{5!} - \frac{\varphi^7}{7!} + ...$$

is considered. The first two terms can be used to describe primary aberrations (spherical aberration, coma, astigmatism, field curvature and distortion) which were studied extensively by L. von Seidel in in the 1850s [23]. Remaining terms denote higher order aberrations. As correcting for the lower order aberrations improves the imaging quality most significantly, the detailed description of higher order aberrations is out of scope for this work. In terms of their nature, aberrations can be chromatic (arising because of the inverse dependence of the refractive index on the wavelength of light) and monochromatic, which are wavelength-independent. Monochromatic aberrations such as spherical, coma and astigmatism blur the image, while field curvature deforms it [23].

Spherical aberration occurs when rays further from the optical axis (peripheral rays) refract more strongly than the paraxial rays close to the optical axis. As a result, they are focused at different points along the optical axis (Figure 1.9). Spherical aberration can be mitigated by underfilling the lens, although in the case where high NA is required it is not feasible. Modern microscope objectives correct for spherical aberrations.

The wavelength bandwith of pusled lasers for 2PM is generally narrow ($\sim$10 nm). However, as various fluorophores are imaged with tunable wavelength lasers, the optical system needs to have a comparable performance over a wide wavelength range. As shown in Figure 1.10, blue light undergoes the largest refraction angle, followed by green and red light. This inability of the lens to bring different wavelengths to a single focus is chromatic aberration and results in colored fringes in the image plane. Achromatic doublets which are composite lenses of convex and concave counterparts with different dispersive properties correct for this effect. Modern apochromatic objectives bring red, green and blue wavelengths to focus using several combinations of doublet and triplet compound lenses for a more robust chromatic correction.

Other geometric aberrations include astigmatism, field curvature and coma. Co-

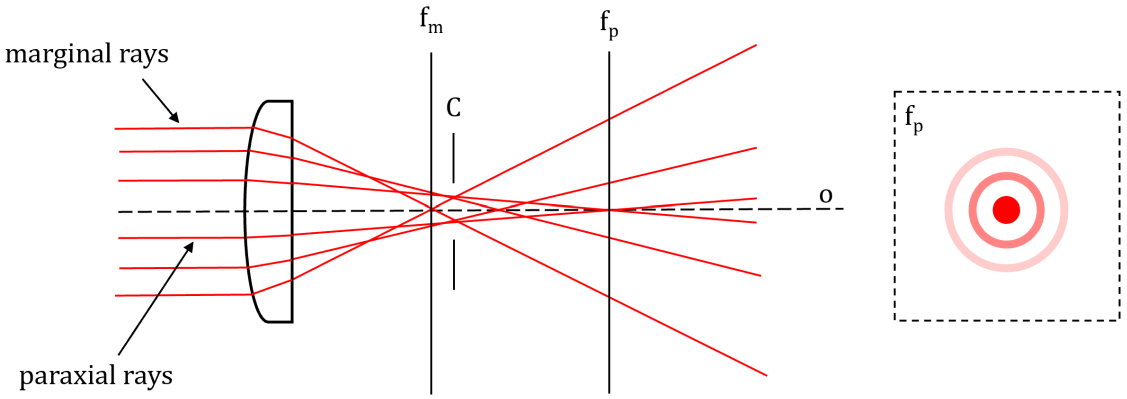

Figure 1.9: Ray diagram illustrating spherical aberration. Consider a monochromatic beam incident on a convex-plano lens. Its paraxial and peripheral rays are focused on a different point along the optical axis (o) with f_p and f_m, respectively. The point where the image is blurred the least is the circle of least confusion (C).

matic aberrations occur with off-axis objects or when the incident beam is misaligned to approach the focusing optics at an angle (1.11). With coma, a point source will be imaged asymmetrically, with a comet-like smeared shape. Astigmatism results in a non-uniform focusing strength along different axes of the lens, yielding an asymmetrical image. Finally, field curvature causes blur at the edges of the image plane. This is a direct result of the curvature of the lens. A planar object will be imaged as a plane only in the paraxial region, while the marginal rays will be focused along a curved image surface. Large field of view (FOV) objectives are designed to mitigate this effect.

1.2 3D imaging and methods of axial refocusing

In conventional microscopes, 2D x-y frames at the focal plane of the objective can be obtained in timescales from several milliseconds to some minutes, depending on modality (point-scanned or widefield) and exposure time. With point-scanning, pixel dwell time and step size increases the time needed to acquire the frame. However, as biological samples have complex structural and biochemical function variation in 3 dimensions, this 2D snapshot offers an incomplete picture. To access the deeper layers of the sample volume, either the detector, the sample or the objective is moved, as shown in Figure 1.12a, b and c, respectively.

With either method, individual 2D frames at multiple depths can be acquired and concatenated into a z-stack, although the method in Figure 1.12a would incur significant spherical aberration (further discussed in Section 1.3.1). Reslicing the z-stack offers insight into the 3D structure in the sample volume, as illustrated in Figure 1.13a. Nevertheless, it can take as long as 30 minutes or even hours to obtain a complete stack.

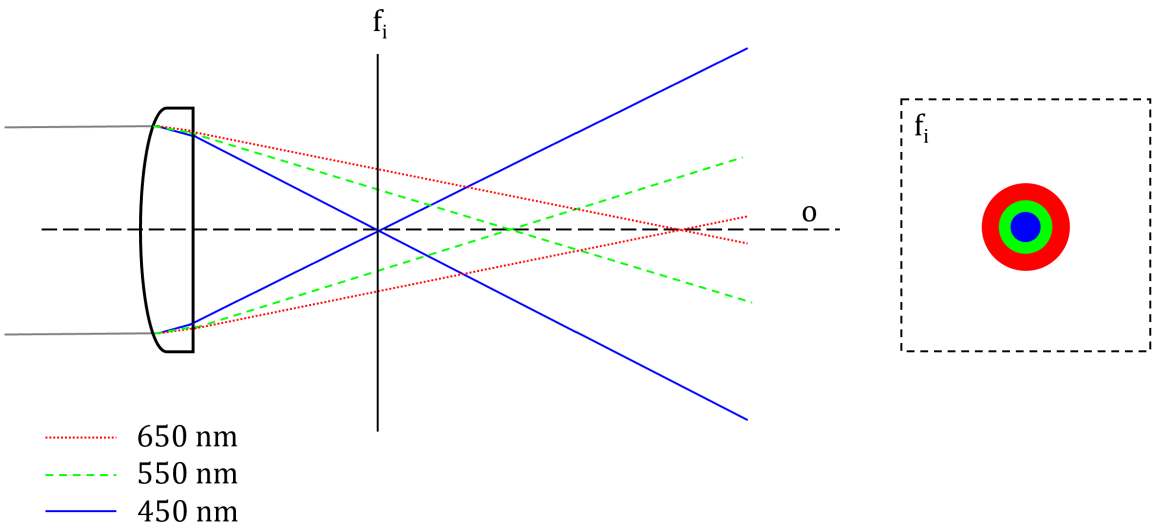

Figure 1.10: An exaggerated ray diagram illustrating chromatic aberration. Different wavelengths have a different focal length along the optical axis (o), resulting in coloured fringes in the image plane (f_i).

This is because although with coarse sampling in x-y, a frame can be acquired within 10-1000 ms, fine steps in z to obtain axial information (for example, 0.1 µm) increase the duration of the scan significantly. Overall, the acquisition duration depends on the pixel dwell time, z range and z step size. Apart from being extremely time consuming, this method prohibits any functional investigation in the axial direction, as electrophysiological or biochemical processes typically occur at timescales of milliseconds. It is possible to line scan axially with e.g. piezoelectric actuators. However, due to the inertia of the bulky sample objective, this is typically limited to a few Hertz. Importantly, during refocusing the sample experiences mechanical agitation, which perturbs its biochemical function and structure.

As traditional axial refocusing methods are slow or cause sample disturbances, multiple alternative refocusing approaches have been proposed to acquire z-y or z-x frames directly, as shown in Figure 1.13b. Electrically tunable lenses (ETLs) and tunable acoustic gradient lenses have a variable range of axial focus [24, 25]. In particular, ETLs are commonly used to axially sweep the focal spot in light sheet microscopes [26]. However, these active refocusing methods are not suited for high NA systems [24–26]. Adaptive optics such as spatial light modulators (SLMs) and deformable mirrors (DMs) can be used for axial refocus [24, 27, 28]. Nevertheless, SLMs are costly and introduce significant power losses while DMs require complex calibration. An advantage of the aforementioned is that by tailoring the device response, other aberrations in the system can also be corrected [24]. Remote focusing (RF) allows fast refocusing by introducing a remote objective and a lightweight actuated remote mirror [4, 5]. This creates an optical copy of the sample which is axially probed by rapidly translating the

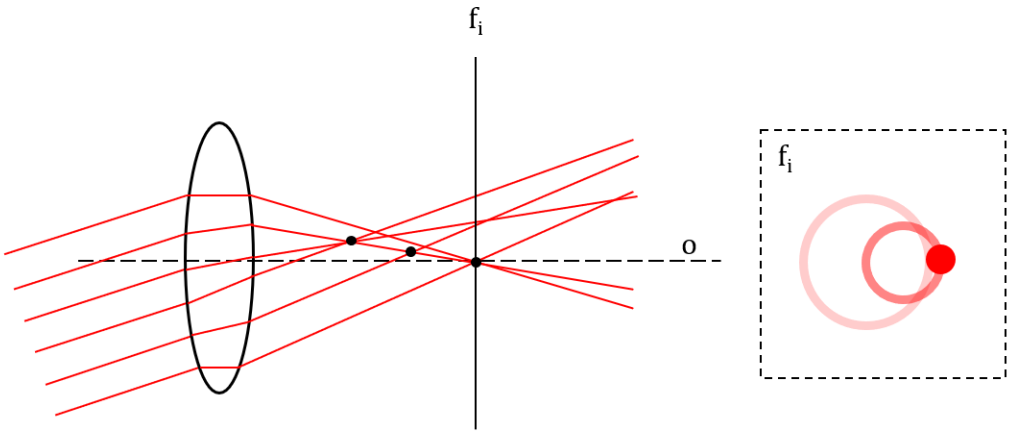

Figure 1.11: Illustration of comatic aberration with the light approaching the lens at an angle with respect to the optical axis (o). This results in an assymetrical smear of the focal point in the image plane.

mirror. This technique is suitable for high NA focusing, has the temporal resolution necessary to follow the propagation of electrical wavefronts while maintaining cellular spatial resolution over a large depth [4, 5]. Multiple studies employ RF to enhance the scanning throughput of conventional microscopes and/or to probe biological function or structure. Single photon-optogenetics [29], light-sheet [30–33] and spinning disk [34] microscopes with RF have been developed. As RF systems require careful design and alignment, characterising the tolerance of these systems to misalignment of various key components has also been subject to study [35–37].

1.3 Principles of Remote focusing

In the following section the fundamental theory behind remote focusing is outlined. For the full description the interested reader should refer to [4].

1.3.1 Sine and Herschel conditions

Consider a perfect imaging system that produces a stigmatic image of a point object not only in the paraxial region and on-axis, but also when it is displaced within some 3D imaging volume. In such an idealised system all rays from a single point source in object space converge to a single spot in the image space without inducing aberrations discussed in Section 1.1.4.

Recall the conventional microscope setup depicted in Figure 1.12. Here, a high NA infinity-corrected objective lens yields planar wavefronts that are focused by a tube lens on some detector to form an image. This optical system obeys to a significant

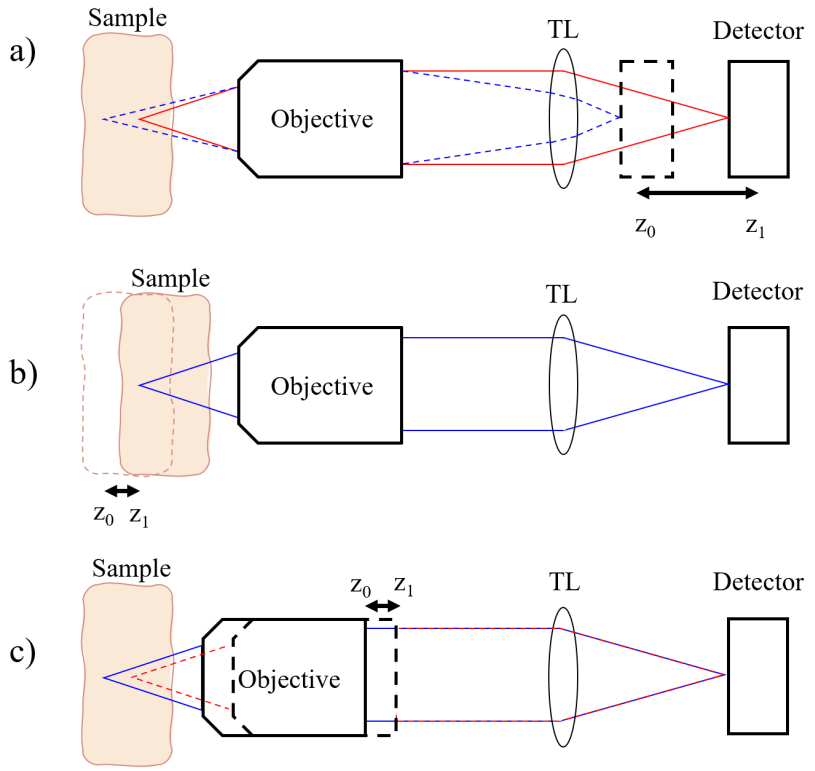

Figure 1.12: Imaging different planes in the sample requires translating the detector (a), the sample (b) or the objective (c). TL is tube lens.

degree the Ernst Abbe Sine condition, where all objects at the nominal focal plane of the objective, both those on- and off-axis, are imaged sharp in the image plane at the detector [4]. Otherwise, for off-axis objects, significant comatic aberration would be introduced towards the edges of the field of view. This is shown in Figure 1.14a. For the sine condition to be met, the object-space angle β_1 is related to the image space angle β_2 as

$$\frac{n_1 \sin \beta_1}{n_2 \sin \beta_2} = |M_L|. \tag{1.6}$$

This ratio is constant for all corresponding image and object space ray angles and represents the absolute value of lateral magnification M_L. As the sine condition is met in the objective's focal plane only, to image a different plane, the sample itself is translated axially (as detailed in Figure 1.12b). Displacing the detector and imaging outwith the nominal focal plane of the objective results in spherically aberrated image and non-uniform axial magnification. In general, the better the system is optimised to follow the sine condition and the better the off-axis coma is corrected.

On the other hand, points situated along the optical axis are imaged stigmatically if the system meets the Herschel condition, as illustrated in Figure 1.14b. Mathematically, this is expressed as

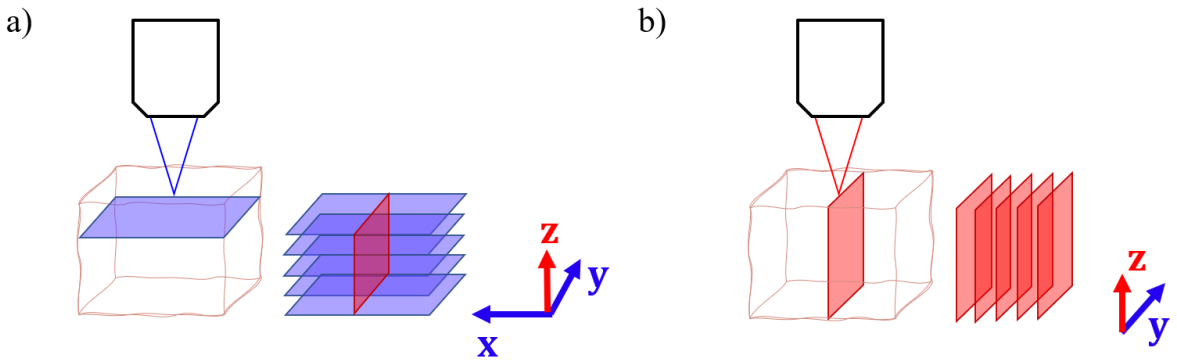

Figure 1.13: 3D imaging strategies: a) acquisition of a z-stack comprised of 2D x-y planes, b) axial refocusing allows directly obtaining z-x or z-y planes.

$$\frac{\mathrm{n_1}\sin^2\left(\frac{\beta_1}{2}\right)}{\mathrm{n_2}\sin^2\left(\frac{\beta_2}{2}\right)} = |\mathrm{M_A}|.$$

Here, the imaging system is designed to ensure constant axial magnification for objects displaced along the optical axis. Evidently, as β increases, the two conditions directly contradict each other and a trade-off must be made for high-NA systems. Those optimised for the Herschel condition can perform stigmatic imaging within restricted lateral FOV for an extended depth of field. Conversely, systems optimised for sine condition can image stigmatically only within the nominal focal plane, displacement from which incurs significant spherical aberration. If the magnification $M_A = M_L = \frac{n_1}{n_2}$, then $\beta_1 = \beta_2$ and both Herschel and sine conditions are satisfied simultaneously. Generally such a close to unity magnification system is of limited use in microscopy context where a high degree of magnification is required. Remote focusing is a method that allows both sine and Herschel conditions to be satisfied simultaneously in high NA systems.

1.3.2 Remote focusing schemes

In remote focusing, an intermediate optical copy of the object volume is created within the imaging system and then probed without disturbing the sample or its objective. Two possible schemes to implement RF are shown in Figure 1.15. In Figure 1.15a, the first two objectives O_1 and O_2 create a diffraction limited remote copy of the sample volume at the focus of O_2. For this to be true, the pupil plane of O_1 is imaged onto that of O_2 with the relay lenses in telecentric alignment and magnification of

$$\mathrm{M} = \frac{\mathrm{n_2 f_2 M_1}}{\mathrm{n_1 f_1 M_2}}.$$

Note that $f_{1,2}$ are the manufacturer's design tube lens focal lengths and $M_{1,2}$ are

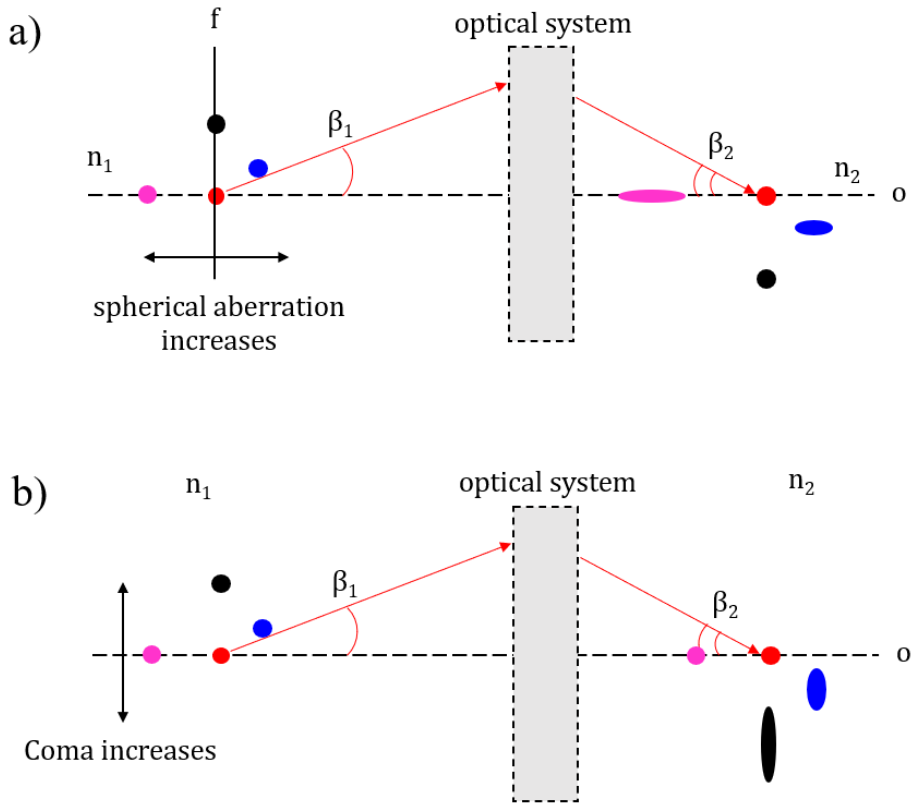

Figure 1.14: Optical system performance when sine (a) and Herschel (b) conditions are satisfied at the interface of two refractive indices n_1 and n_2. *Adapted from* [4].

the magnifications. A detector placed anywhere within this volume would image its planes without spherical aberration. Nevertheless, the pixel dimensions of conventional cameras are not compatible with spatially sampling these planes. Therefore, objective O_3 is translated to refocus within the optical copy without agitation of the sample and the tube lens forms a magnified image at the detector. In Figure 1.15b, O_3 is replaced by a lightweight mirror in a folded geometry setup. The mirror can be axially agitated at much higher refocusing frequencies than those limited by the inertia of the bulky O_3 [4, 5]. As a result, RF is a suitable method for high-speed and high-NA imaging.

Mathematically, RF allows stigmatic imaging of axially displaced objects outwith the nominal focal plane because the spherical aberration induced in the sample objective by illuminating it with curved wavefronts is compensated by the aberrations of the opposite sign in the remote objective. This is a consequence of the odd parity of the pupil function: $\Psi(\rho, \phi, -\mathbf{r}) = -\Psi(\rho, \phi, \mathbf{r})$, detailed in [4]. It can be shown that if an objective obeys the sine condition, the phase profile generated in the pupil plane for a point source located at the position (x,y,z) in the focal region of O_1 can be written as

$$\Psi_1(\rho_1, \phi) = \mathrm{k n_1} \sin\alpha_1 \left(\mathrm{x}\rho_1 \cos\phi + \mathrm{y}\rho_1 \sin\phi + \mathrm{z}\left(\frac{1}{\sin^2\alpha_1} - \rho_1^2 \right) \right) \tag{1.7}$$

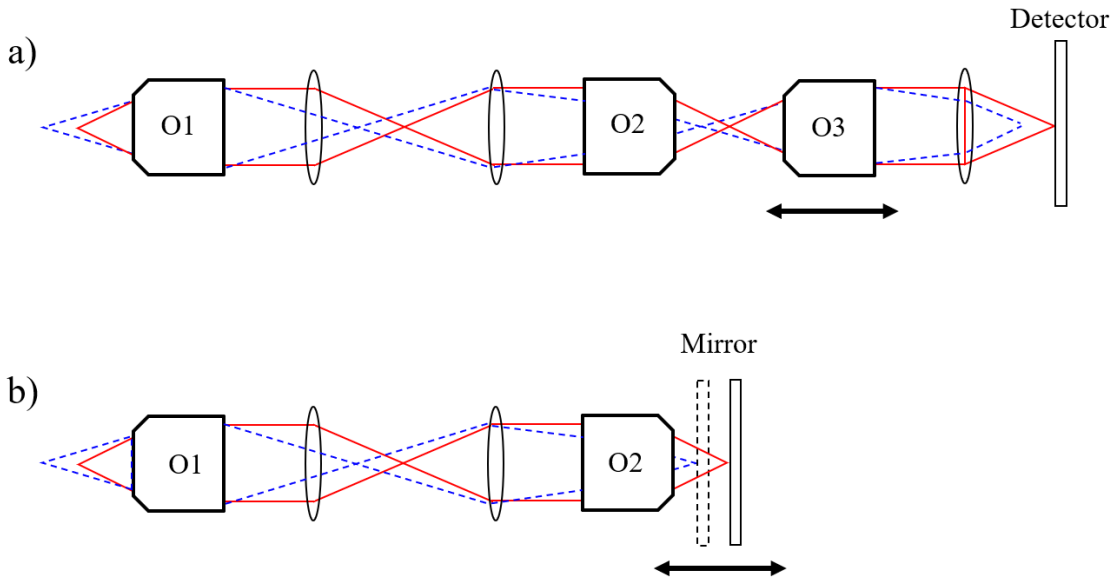

Figure 1.15: Two remote focusing schemes. *Adapted from* [4].

Additionally, the phase profile required to focus all the rays stigmatically to a point located at $\frac{n1}{n2}$ × (x,y,z) in the focal region of O_2 can be expressed as

$$\Psi_2(\rho_2, \phi) = \mathrm{kn_2} \sin\alpha_2 \frac{\mathrm{n_1}}{\mathrm{n_2}} \left(\mathrm{x}\rho_2 \cos\phi + \mathrm{y}\rho_2 \sin\phi + \mathrm{z} \left(\frac{1}{\sin^2\alpha_2} - \rho_2^2 \right) \right). \tag{1.8}$$

If the $4f$ system mapping the pupil planes together has magnification $M = \frac{\rho_2}{\rho_1} = \frac{\sin\alpha_1}{\sin\alpha_2}$, the Equations 1.7 and 1.8 are identical and the point source is imaged without aberrations in the focal region of O_2. This optical system images a three-dimensional volume with a uniform magnification factor of n_1/n_2, meeting the requirements of a perfect imaging system discussed in Section 1.3.1 [4].

1.3.3 Golden rules of remote focusing

For implementation of diffraction limited RF systems, there are three "golden rules" that must be adhered to. Firstly, the ratio of the refractive indices of the sample n_{sample} and its remote replica n_{RR} must be equal to the magnification of the setup:

$$\mathrm{M_{RR}} = \frac{\mathrm{n_{sample}}}{\mathrm{n_{RR}}} \tag{1.9}$$

For instance, as the remote objective is generally for air (with n_{RR}=1), M_{RR} = 1.33 for a water immersion primary objective. Relay telescopes between the sample and remote objectives are introduced to meet this condition. For diffraction-limited refocusing, the relay lens alignment should be telecentric. Secondly, to ensure maximum

allowed numerical aperture of the system, the remote objective should have an angular acceptance angle greater or equal to that of the sample objective or

$$\frac{\mathrm{NA_{RR}}}{\mathrm{n_{RR}}} \geq \frac{\mathrm{NA_{sample}}}{\mathrm{n_{sample}}} \tag{1.10}$$

Finally, the apertures of the optics need to be large enough so that no wavefronts are clipped. This is important as the light leaving the remote objective may have large divergence at "defocused" mirror positions.

1.4 Published remote focusing microscopes and their applications

Since remote focusing was proposed by Botcherby et al. in 2008 [5], it has been employed in many studies to enhance the imaging throughput of microscopes to probe biological function or structure in both dynamic and static configurations. Single photon-optogenetics [29], light-sheet [30–33, 38] and spinning disk [34] microscopes with RF have been developed. Additionally, multiphoton microscopes featuring RF have been implemented [6–8, 27, 39–41]. To achieve dynamic refocusing, deformable mirrors [27], custom built actuators [6, 8], piezoelectric actuators [29, 34] and voice coil actuators have been used [39, 42, 43]. In the following section a review of published RF systems, their characterisation and applications is presented. The literature review is divided into three sections. Firstly, studies detailing the criteria and alignment of optically robust remote focusing systems are discussed. Secondly, published systems are distinguished between application of the RF in the imaging or the excitation side of the microscope.

1.4.1 Optical robustness of RF systems

To begin with, as RF systems require careful design and alignment, characterising the tolerance to misalignment of key optical components has been subject to study [35–37]. As discussed in Section 1.3, the pupil planes of the sample and remote objectives should be imaged onto one another as precisely as possible. In Mohanan et al. (2022) [35], the sensitivity of RF microscopes to magnification mismatch was characterised with a computational model for objective pairs with different numerical apertures. A folded RF system was built with three different relay lens magnifications to verify the theoretical findings, where the residual spherical aberrations were quantified with a Shack Hartmann wavefront sensor. Evidently, higher NA systems (air and oil for remote and sample objectives, respectively) were more sensitive: the range of diffraction limited

PSF can be reduced by 50% for a magnification mismatch as low as 1% [35]. While the aforementioned study considered only the on-axis aberrations, system performance over the three-dimensional imaging volume was evaluated in Hong et al (2023) [37]. In addition to a description of an advanced RF alignment scheme, microscope performance as a function of axial misalignment of the remote and sample objective and its tube lens was characterised. Additionally, the impact of lateral displacement and focal length change of the remote Plössl tube lens was assessed. For each case, the point spread function and integrated signal was measured with sub-resolution fluorescent beads to evaluate the resulting distortion. Displacement of the sample objective by ± 1 mm caused a 43% reduction in the diffraction-limited imaging volume. The system was less sensitive to axial misalignments of the tube lenses. However, the lateral displacement of the remote tube lens by as little as 0.13 mm reduced the diffraction-limited imaging volume by up to 93%. Although the study only characterised a single microscope, not a generalised RF system, the findings are comparable to those in [35]. Overall, the consensus is that the imaging quality of RF systems is highly susceptible to misalignment or magnification mismatch. Finally, in Corbett et al. (2014), geometry and preparation of a volumetric calibration sample to account for RF system distortions was proposed. Zemax simulation was compared to experimental data produced by different axial and lateral positions of the remote objective. The novel 3D sample was used to correct for induced distortion and improve the accuracy of cardiac sarcomere structure imaging in post-processing [36].

1.4.2 Imaging RF systems

Remote focusing in both folded or extended geometry is commonly incorporated in the imaging arm, predominantly in light sheet microscope (LSM) systems. Oblique plane microscopy (OPM) introduced in Dunsby (2008) [44] is a notable example [44–46]. In LSMs, sample dimensions are often restricted due to the working distances of the illumination and detection objectives and the requirement for the objective lenses to be placed orthogonally to each other. Furthermore, to avoid introducing defocus, high numerical aperture microscopes require that the illumination and detection planes overlap with micrometer-scale accuracy. In OPM, this is circumvented by implementing the oblique light sheet in the epi-illumination scheme, which is compatible with standard cell culturing well plates. Cylindrical lenses can be used to create the light sheet and if the excitation beam is incident at the edge of the back focal plane of the sample objective, a tilted light sheet is formed at the objective's focal plane. A galvanometric mirror can be used to both translate the oblique excitation light sheet in the object space and de-scan the fluorescence emission. Remote focusing in unfolded geometry is key in OPM, as it is used to image the fluorescence from the oblique plane

onto the detector. In OPM, the off-axis orientation of the remote objective restricts the effective NA of the imaging system [44]. Interestingly, a custom cuvette between the RF objectives providing a water-air interface with a coverslip at the intermediate image plane allows preserving the high NA of the system. This is because the refractive index mismatch between the remote objectives compresses the light cone angle. In [38], sub-micron resolution was achieved within the imaging volume ($70 \times 20 \times 100\,\mu m$ in y, x and z, respectively) and the system was used for multicolour imaging of endogenously labelled human embryonic kidney preparations [38]. Importantly, OPM has been employed to study the electrophysiology of isolated cardiomyocyte preparations [45, 46]. In [46], calcium dynamics in cardiac muscle cells were probed in 2-dimensional planes and at 926 frames per second and in 3-dimensions, at 21 volumes per second. In [45], the OPM with two spectral channels allowed simultaneous imaging of calcium dynamics and visualising the sarcolemma and transverse tubule structures at the location of origin of spontaneous calcium waves.

A bi-modal LSM with RF to enhance temporal resolution of the imaging arm was developed in Sparks et al. (2020) [33]. In particular, RF optics were used for 25 Hz sweeping of the focal plane in the detection arm, allowing multiple studies of electrophysiology in various cardiac preparations [31, 32]. High spatial resolution mode of the LSM allowed resolving the T-tubule and sarcomere structure, while the high temporal resolution mode yielded video rate imaging and visualisation of calcium dynamics in live cells [31, 33]. Furthermore, the LSM was used to evaluate the electromechanical coupling between human stem cell-derived and adult mouse cardiomyocytes in co-culture [32]. Here however, while dynamic RF increased the throughput of the system, unlike in [38], the geometry of oblique LSM does not accommodate larger preparations where the cardiac cells function within their intact, native environment in tandem with hundreds of healthy or diseased neighbouring cells. For more RF-LSM microscope implementations, the interested reader should refer to [47, 48].

While the aforementioned studies employ static or slow RF, in [43], FLIPR or flipped image remote focusing was introduced, allowing light-efficient voltage imaging at 500 Hz volumetric rate with 150 µm refocusing range. RF optics were introduced in the detection arm of a light sheet microscope, where the coupling of light was achieved with a microscope knife edge mirror and retroreflector. In detection fluorescence is not polarised so the traditional RF implementation with polarisation optics would reject half of the light. Instead of placing a mirror in the remote image plane, the authors used a microscopic retroreflector to flip and fold the image back into the remote focusing arm and spatially separate incoming and outgoing light. The system was applied for zebrafish neural imaging.

A noteworthy system employing dynamic RF in detection to probe the sample at

oblique angles is described in Anselmi et al. (2011), [29]. Here, spatial light modulator holography was used to generate structured light for optogenetics within an epi-fluorescence microscope to probe neural calcium dynamics. Remote focusing was implemented in a folded geometry to allow a refocusing range of 300 µm. Additionally, placing the remote mirror on a rotating gimbal mount allowed scanless imaging of tilted dendrites of hippocampal neurons in murine brain slices.

1.4.3 In-excitation RF systems

Remote focusing optics in the excitation arm of microscopes have also been implemented, predominantly in multiphoton systems [6–8, 41], and most often in neural tissue. For instance, calcium transient responses were measured from neurons 200–300 µm below the mouse cortical surface with a 2P-RF microscope capable of 2.7 kHz axial scan rates [6]. Here, the remote mirror was translated rapidly with a custom made actuator comprised of two galvanometers to scan the Ti:Sa excitation beam. In conjunction with the microscope's lateral scanning unit, the system achieved arbitrary scanning of 3D trajectories. The same system was used in Botcherby et al. (2013), where sarcomere length of cardiomyocytes was measured at 2.7 kHz rate scanning [8]. Here, two perpendicular oblique planes within an intact, Langendorff-perfused heart were rapidly imaged to extract a more precise sarcomere spacing value that is corrected for cardiomyocyte cell orientation angle. Here, only cardiac structure, not function was studied. Another arbitrary scanning 2P-RF system was described in Sofroniew et al. (2016) [41]. A commercialised large FOV 2-photon random access mesoscope with a RF module allowed imaging anywhere within the mouse brain in cylindrical segments of 5 mm diameter and 1 mm height. The imaging objective of 0.6 NA yielded nearly diffraction limited resolutions of 0.66 µm laterally and 4.09 µm axially. The RF mirror is moved by a voice coil actuator and dispersion compensation is implemented in the system. However, this microscope is patented and uses expensive custom objective manufactured specifically to enhance the transmission of the RF module in the IR range, rendering it rather inaccessible [41]. An important observation is that in [6], RF is implemented after lateral scanning. On the other hand, in [41], the beam passes RF optics before subsequent lateral scanning, thus relieving the requirements on acceptance angle of the remote objective. Additionally, both studies highlight the limitation of power at sample imposed by the etching of remote mirror due to tight focusing on its surface. An integrated 2- and 3-photon microscope for calcium neural imaging is presented in Weisenburger et al. (2017) [39], where spatiotemporal multiplexing, one-pulse-per-pixel excitation, remote and temporal focusing methods were combined. A linear voice coil actuator was used to move the remote mirror at 17 Hz to achieve volumetric scanning ($1 \times 1 \times 1.22$ mm) of neurons in *in vivo* murine cortical

depth. Similarly to [41], in the aforementioned study a voice coil device is used to translate the remote mirror and RF is implemented before the lateral scan unit.

Remote focusing in excitation arm can also be employed for multiplane imaging. In Chong et al. (2019), a 2P-RF microscope with two illumination paths probed genetically encoded GCaMP calcium dynamics in the planes 120 µm and 250 µm below the brain surface in *in vivo* mice [40]. An acousto optical deflector was employed to rapidly switch (timescale of µs) between the illumination paths, one of which contained the static remote focusing optics. High NA aspheric lenses designed to correct for on-axis spherical aberration were used in the RF path to cut down the cost. While objective lenses also have well-corrected off-axis performance, only on-axis correction is required if the focusing system is placed before the lateral scan mirrors. To account for specimen induced motion artifacts, the depth of focus was extended to 12 µm by underfilling the back aperture of the sample objective to ensure that the neuron structures of interest stay within the imaging region [40]. Similarly, RF was used also with 3PM [7] to image two static planes 600 and 650 µm deep in mouse cortex, at the rate of 7 Hz. Note that like in [40], high NA lenses were used for RF instead of an objective [39].

While the aforementioned microscopes integrate RF optics in a particular set up, in Rupprecht et al. (2016) [42], a cost effective RF-based z-scanning module assembled with off-the-shelf optomechanics and compatible with commercial multiphoton microscopes was developed, employing high NA lenses and a voice coil to translate the remote mirror. The RF module was designed to be positioned before the x-y scanning unit of a general microscope, compatible with high NA objectives and featured a large z-scan range (more than 300 µm). A voice coil actuator to scan at several tens of Hertz speeds was employed. Two configurations were presented, one with and one without an additional telescope for magnification matching. Although not ideally magnification matched to every system, the authors argue that their simplest RF z-scan unit provides a satisfactory performance, because multiphoton microscopy does not rely on the formation of an image on the detector. The system was verified in zebrafish brain calcium imaging to inspect activity patterns across more than 1500 neurons with single-neuron resolution.

1.4.4 Summary

A few themes arise in the reviewed studies. Most RF implementations are in the imaging arm of light sheet microscopes [31, 33, 38, 47]. If multiphoton in-excitation systems are concerned, RF optics are generally placed before the lateral scanning unit [39, 41, 42]. The requirements for power and pulse duration for efficient 2PM complicate the implementation of high NA systems, particularly due to power density incident on the remote mirror, potentially etching it [6]. Mitigating power losses after the reflection

from RF mirror is crucial [41]. Nevertheless, when the material of the mirror of choice is mentioned, standard protected silver is used [6, 39, 41]. Regarding the scanning speed, voice coil actuators are a popular choice due to their smooth motion in the range of up to some hundreds of Hertz in both LSM and multiphoton systems [39, 41–43]. For faster speeds, custom made scanning units as in [6] are employed. The applications of RF in multiphoton microscopy are predominantly focused on neural tissue electrophysiology [6, 7, 39, 40]. Nevertheless, the brain is significantly less scattering compared to, for example, cardiac preparations. The studies that use RF to probe cardiac preparations only do so to assess the structure with 2PM [8] or investigate the electrophysiology in single photon oblique light sheet modality. Additionally, the samples in the LSM studies include isolated cardiomyocytes or engineered tissue preparations of limited size [30–32], preventing imaging of large scale tissue such as Langendorff-perfused hearts. The work described in this Thesis contributes to the body of published literature with the development of a voice coil actuator based RF module for a commercial 2-photon microscope, geared towards functional deep-tissue cardiac imaging. The optimisation of the optical system is described as well as the detailed sample preparation protocol, ensuring its compatibility with 2P-RF imaging.

Chapter 2

Fundamental structure and function of the heart

The heart is essential to maintaining the body alive; it is an efficient pump, distributing oxygenated blood from the lungs throughout the body. The following Chapter outlines briefly the structure and mechanical function of the heart (Section 2.1). Furthermore, the underlying electrical signal propagation that governs this mechanical contraction is explained (Section 2.2).

2.1 Cardiac structure and mechanical function

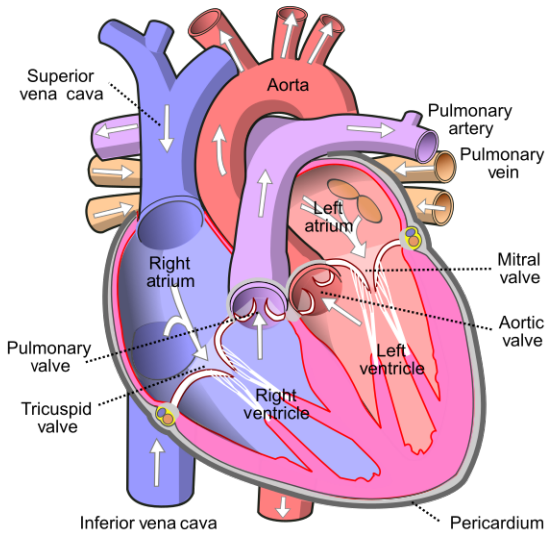

Figure 2.1: Structure of the heart and the pathways of oxygen rich (red) and oxygen depleted (blue) blood. *Adapted from* [49].

On a whole organ scale, as shown in Figure 2.1, the heart has four chambers,

namely the right and left atria and the right and left ventricles. These core parts enable the organ to pump blood. The oxygen-depleted blood from the upper body flows to the heart through the superior vena cava vein, while the blood from the lower body enters through the inferior vena cava. As a result, the right atrium is filled. The blood then travels to the right ventricle (RV) through the tricuspid valve and to the pulmonary artery, passing yet another valve upon its entrance. Here is is re-routed to the left and right lungs, where the alveoli allow enriching the blood with oxygen as the CO_2 is discarded. Oxygenated blood can then re-enter the heart through the pulmonary vein to the left atrium and travels to the left ventricle (LV). The LV is the main chamber of the heart; its thick wall and larger volume (compared to RV) allows pumping the oxygenated blood through the aorta into the complex network of blood vessels, efficiently distributing it throughout the body [50].

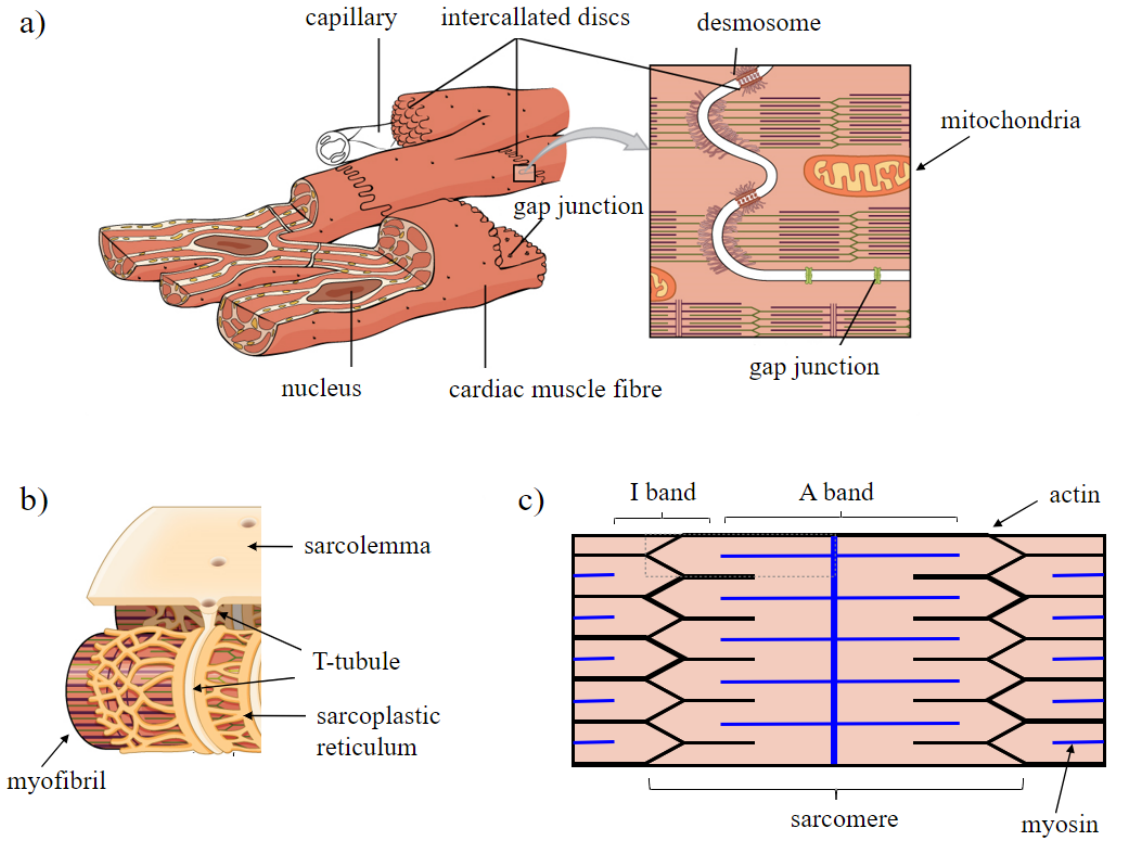

Figure 2.2: Cellular structure of the cardiac muscle. Branched cardiomyocytes are connected with intercallated disks containing gap junctions which facilitate cell to cell electrical conduction (a). In b), the structure of the cell membrane (sarcolemma) is illustrated. T-tubules play a key role in intracellular calcium concentration regulation. The myofibril strands run along the long axis of the cells and facilitate mechanical contraction. In c), a schematic of actin and myosin filaments within the myofibrils is is shown. *Adapted from* [51, 52].

On a cellular scale, the cardiac muscle is comprised of orderly cardiomyocyte layers

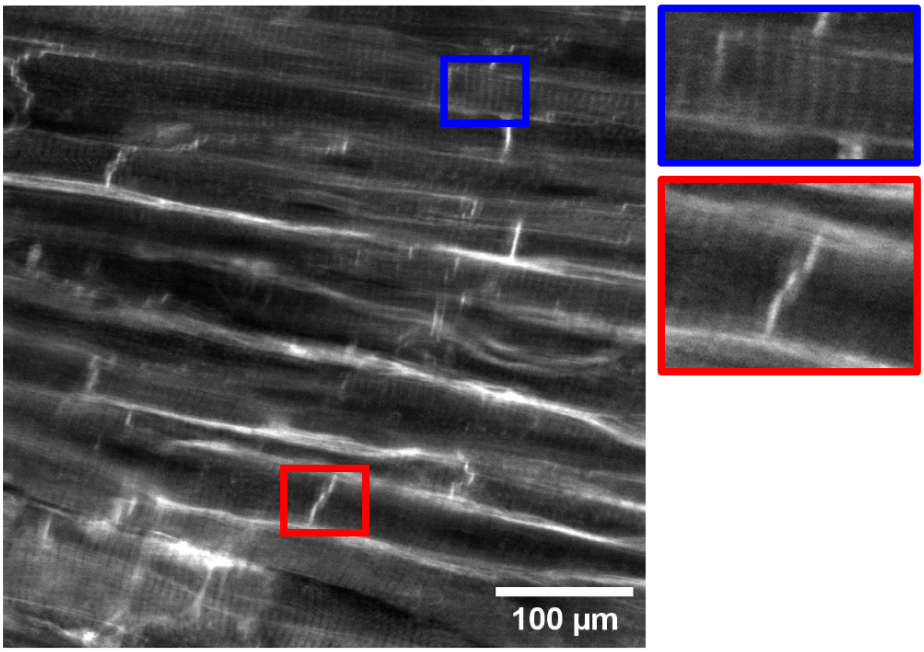

Figure 2.3: FluoVolt labelled cardiac muscle imaged with 2PM. FluoVolt primarily labels the cellular membrane. Intercallated disks connect adjacent cardiomyocytes (red ROI). Actin-myosin band striations are shown in the blue ROI.

which contract in the presence of electrical stimulation. Individual cardiac cells are generally approximately 20 µm thick and 200 µm long and can be branched (Figures 2.2a and 2.3). The cell membrane (the sarcolemma, Figure 2.2b) accommodates ion channels that open and close as the potential difference across the membrane changes, thus allowing the charge carriers to migrate in and out of the cell. Additionally, the desmosomes within the membrane hold the cells together. The intercallated disks (Figures 2.2a and 2.3, red ROI) are key in cell to cell electrical signalling. The striations (Figures 2.2c and 2.3, blue ROI) in cardiomyocytes are visible because of the sarcomeres comprised of myosin and actin filaments. The interactions between the aforementioned facilitate mechanical contraction of the muscle, further outlined in Section 2.2.1.

2.2 Action potential propagation

Electrical signals or action potentials originate in the natural pacemaker cells of the heart and travel through the organ. These wavefronts propagate in an orderly fashion through the internodal pathways (Figure 2.4), resulting in systematic contraction. Depolarisation is a phase in an action potential during which the cell's charge rapidly changes and becomes more positive than its environment. Generally, in a healthy heart, the depolarisation propagates from the top right to the bottom left. In the sinoatrial node, cells can depolarise by themselves, independently from the nervous system, ex-

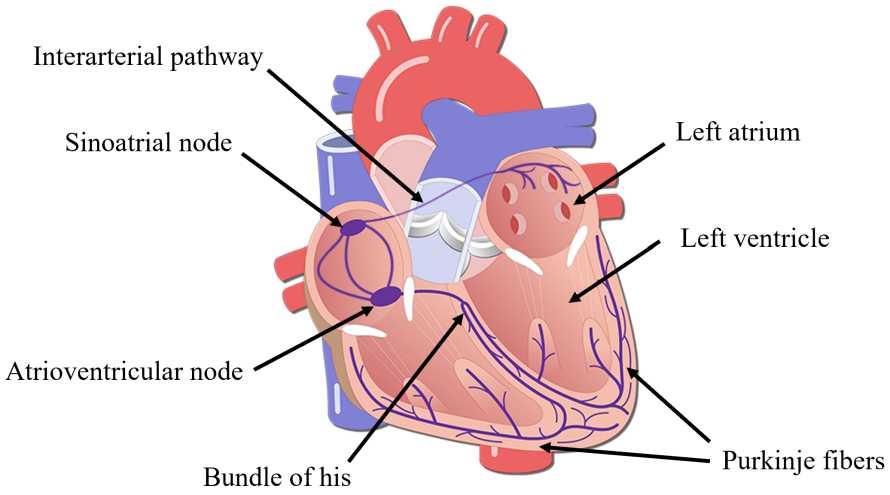

Figure 2.4: Internodal pathways for action potential propagation in the heart. *Adapted from* [53].

hibiting automaticity. Consequently, the neighbouring cells also depolarise and this electrical wavefront propagates to the left atrium and the atrioventricular node. In the lower regions of the organ, cardiac conduction is slower; the electrical wavefront is spread through the Purkinje across the myocardium in the ventricular wall. In the LV of rabbit, a commonly used animal model in cardiovascular science, the action potential has two propagation speeds: longitudinal (along the long axis of the cell) and transmural (along the short axis of the cell, from the innermost to the outermost layers of the ventricular myocardium). The longitudinal conduction velocity is approximately 75 cm/s while the transmural equivalent is slower, around 30 cm/s.

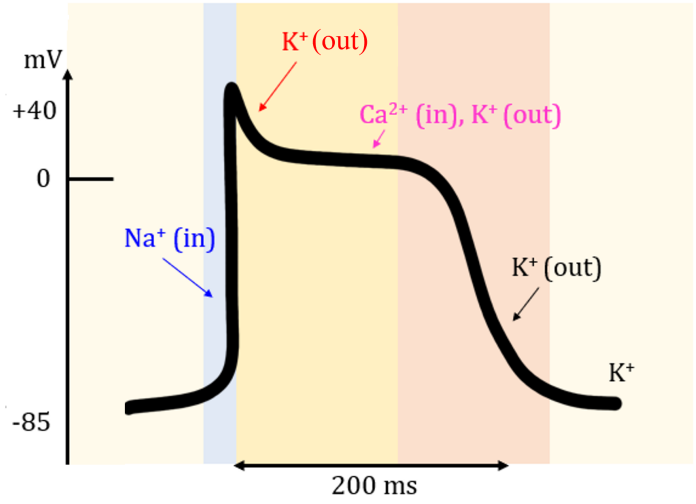

Figure 2.5: Schematic diagram of a rabbit action potential and its phases. An action potential, induced by the pacemaker cells in the sinoatrial (SA) and atrioventricular (AV) nodes, is conducted to cardiomyocytes through gap junctions. Migration of charged ions in and out of the cell during different phases of the AP cause opening and closing of different ion channels thus resulting in this potential change across the cell.

The schematic of rabbit action potential is shown in Figure 2.5, the duration of which in the LV is approximately 200 ms under physiological conditions. The resting potential of the cell is approximately -85 mV, as the charge entering and leaving the carciomyocyte is balanced. An influx of Na^+ ions to the cell trigger a rapid depolarisation phase, causing the overall cell charge to become significantly more positive. For this process to be initiated, another action potential from the neighbouring cell is transmitted though the gap junction: as the voltage difference across the membrane exceeds the threshold slightly above resting potential, the aforementioned sodium channels open. When Na^+ channels close, the potassium leaving the cell makes it more negatively charged. Here the plateau phase begins, where the membrane potential is maintained approximately constant through the balance of Ca2+ and K+ entering and leaving the cell, respectively. As the repolarisation begins, the positive potassium concentration decreases significantly, returning the cell to its resting potential. Note that cardiomyocytes have multiple refractory phases. From depolarisation to well into the repolarisation, no new depolarisation wave can occur irrespective of electrical stimulus strength, as the sodium channels are inactivated. Towards the end of the repolarisation, a stronger electrical stimulus is can initiate another action potential in the cell. After that, cardiac cell excitability returns to normal [54].

2.2.1 Excitation-contraction coupling in the heart

Excitation-contraction coupling governs how electrical events result in mechanical events within the myocardium. Overall, with the voltage change across the sarcolemma, the influx of Ca2+ ions to the cell causes the myosin filaments to slide along actin filaments (shown in Figure 2.1) shortening or lengthening the sarcomere. The relative timing of these events is illustrated in Figure 2.6.

As discussed in Section 2.2, the opening of calcium channels results in an influx of Ca2+ ions to the cell, governing the relatively constant potential difference during the plateau phase (Figure 2.5). The aforementioned migration as well as the additional release of Ca2+ through the sarcoplastic reticulum within the cell raise the concentration of free intracellular calcium ($[Ca2+]_i$) within the cytoplasm. Subsequently, the intracellular calcium interacts with the troponin-C protein and the troponin complex moves away from the actin binding site. This removal of the troponin complex frees the actin and initiates the contraction, as the myosin head pulls the actin filaments toward the center of the sarcomere. This process requires adenosine triphosphate or ATP which is an energy carrying molecule. As the concentration of $[Ca2+]_i$ within the cell decreases, the bond between troponin and calcium disassociates, resulting in delayed muscle relaxation. For a detailed explanation of Ca2+ pathways in and out of the cell, the interested reader should refer to [55].

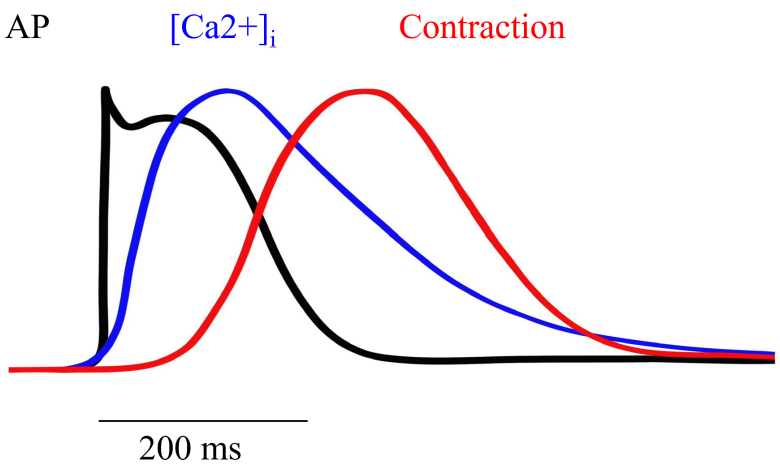

Figure 2.6: Cardiac excitation-contraction coupling. The relative timing of the action potential, the changing intracellular calcium current and the contraction in rabbit heart is illustrated *Adapted from* [55].

Thesis motivation

Understanding the aforementioned voltage change and calcium dynamics across the cardiac cell membrane is crucial for development of diagnostic interventions; the shape and temporal properties of AP helps to infer how different drugs or therapies affect cardiac function. Voltage measurements in cardiac models can be facilitated directly and invasively with intracellular electrodes or non-invasively with optical methods [1]. The optical methods employ voltage sensitive fluorescent dyes (VSDs), which allow both surface level optical mapping [56] and deep tissue investigation with multiphoton microscopy [3]. Nevertheless, the electrical conduction across the myocardium is a highly 3-dimensional phenomenon, where variation in cell type distribution influences electrical wavefront propagation. While multiphoton microscopy allows probing electrical function in distinct cellular planes within the myocardium [3, 57, 58], the transmural action potential propagation from the endocardium to the epicardium remains inaccessible directly, as conventional microscopes cannot provide a rapid axial scan without disturbing the sample. Commonly used piezoelectric actuators can move bulky microscope objectives at some tens of Hz directly close to the sample. The resulting mechanical perturbation can affect its biochemical function. Furthermore, this method is too slow to resolve cardiac AP properties. Nevertheless, remote refocusing, reviewed in Section 1.3 can provide the rapid axial scan and is compatible with 2-photon microscopy that allows optical sectioning and deep tissue penetration.

Importantly, deep tissue cardiac function has not yet been investigated with RF-enhanced microscopy. As discussed in Section 1.4.4, design optimisation is not discussed in detail especially in the context of coupling RF to a commercial microscope

for deep imaging in a highly scattering cardiac tissue where signal is scarce. The core aim of the thesis is therefore to develop a 2P-RF microscope capable of functional imaging in cardiac preparations along the transmural and longitudinal directions. Furthermore, a secondary aim is to develop a pipeline for imaging, including establishing a viable acute cardiac sample preparation protocol. In Chapter 3, building and characterisation of the 2P-RF system will be discussed. In Chapter 4, the prepraration and quality assessment of acute rabbit ventricular cardiac slice model will be outlined. In Chapters 5 and 6, 2P-RF system will be applied to image the structure and electrophysiological function of the cardiac slices, respectively. Finally, Chapter 7 will detail future prospects of this work, translating the system to allow following the AP in physiological conditions as well as the scope and possible methods for correlative function-structure imaging.

Chapter 3

Development and characterisation of RF-2PM system

As discussed in Section 1.3, conventional microscope systems are not capable of rapid axial scanning. Therefore, to probe cardiac electrical wavefront propagation transmurally, a custom remote refocusing module was assembled and retrofitted to the commercial Scientifica 2-photon microscope installed in the laboratory. In the following chapter all stages of the imaging system implementation are discussed, including optical design (Section 3.1), alignment (Section 3.3) and characterisation of the 2P-RF microscope resolution, power efficiency and dispersion (Sections 3.4, 3.5 and 3.6, respectively). Finally, temporal resolution and voice coil performance were assessed in Section 3.7. We demonstrate that the system is optimised for cardiac function imaging, yielding axial refocusing speed of up to 250 Hz, 152 fs pulse duration and 22 mW average power available at sample.

In the following chapter all work is my own with the exception of dispersion compensation, detailed in Section 3.6. Here, the single prism compressor was assembled together with another PGR Lewis Williamson and the in-line autocorrelator to measure pulse duration was implemented entirely by him based on the system in [59]; the corresponding result of pulse duration measurement at the focal plane of the sample objective is stated in this Thesis for completeness only.

3.1 Optical design considerations

In the following section, the optical design of the RF module is detailed. Firstly, the theoretical refocusing range of the module is estimated for the choice of objectives and relay lenses which ensure magnification matching. The optomechanics and custom parts are put together in a CAD Fusion 360 model for verification of the design.

3.1.1 Objective choice and the theoretical diffraction limited range

The choice of objectives for RF systems is important, as the experimental requirements (e.g. immersion media), cost, power efficiency and the achievable refocusing range have to be considered. Furthermore, once the system is designed for the particular objective pair, they cannot be replaced without complex redesign and realignment. The 20X Olympus XLUMPLFLN with 1.00 NA was chosen as the sample objective. It is specifically designed for electrophysiology (water dipping with a large 2 mm working distance) and is compatible with cardiac samples immersed in Tyrode's solution. The remote objective was chosen to be the Nikon CFI Plan Fluor with 0.75 NA and 40X magnification. As discussed in Section 1.3.3, it provides an angular acceptance greater or equal to that of the sample objective (according to $\frac{NA_{RF}}{n_{RF}} \geq \frac{NA_{sample}}{n_{sample}}$) needed for diffraction limited remote refocusing. Additionally, its 660 µm working distance allows the remote mirror to be translated distances yielding a large enough refocusing range when the coverslip thickness (170 µm) is accounted for. Importantly, both remote and sample objectives have favourable transmission at near infrared wavelengths (approximately 77% and 69% at 800 nm, respectively). This is particularly important to mitigate losses in the 2P-RF system, as discussed in Section 1.4.4. Additionally, the objectives are corrected for field curvature and chromatic aberrations.

Strehl ratio allows evaluation of imaging quality. It is often defined as the ratio of peak measured intensity to peak ideal intensity in a diffraction-limited system. In [4], Strehl ratio is used to determine the theoretical range of a general RF system for a given wavelength and objective NA, according to the equation:

$$\mathrm{S} = 1 - \frac{4\mathrm{n}^2\mathrm{k}^2\mathrm{z}^4(3 + 16\cos\alpha + \cos 2\alpha)\sin^8\frac{\alpha}{2}}{75\mathrm{f}^2(3 + 8\cos\alpha + \cos 2\alpha)} \tag{3.1}$$

where $k = \frac{2\pi}{\lambda}$ is the wavenumber, z is the RF mirror displacement, α is half of the objective's light cone acceptance angle and f is the effective focal length. Additionally, the image of the point object will be axially displaced from the correct position in the remote volume even with perfect RF system alignment [4]. This defocus, δz is defined as

$$\{\delta z = -\frac{12z^2\cos^2\frac{\alpha}{2}(3 + 6\cos\alpha + \cos 2\alpha)}{5f(3 + 8\cos\alpha + \cos 2\alpha)}. \tag{3.2}$$

Note that both S and δz are symmetric around the origin therefore the effective range is doubled for bidirectional remote mirror displacement from the nominal focal plane.

In Figure 3.1 the Strehl ratio and defocus along the refocusing range is calculated

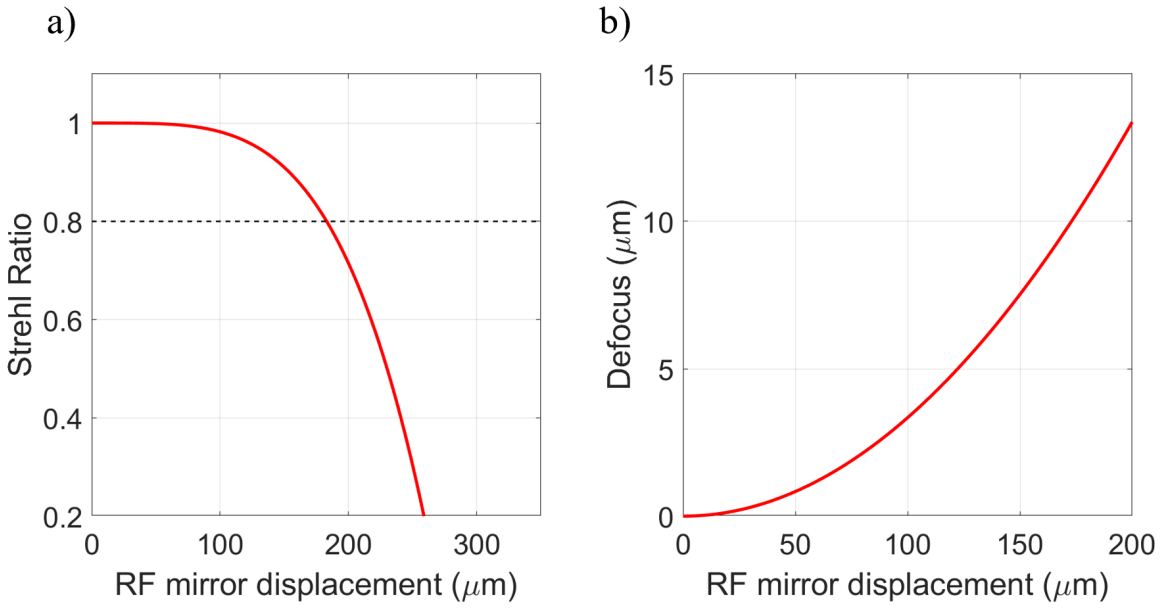

Figure 3.1: Theoretical RF range allowed by our system. The remote objective with the lower light acceptance angle ($\sin(\alpha) = 0.75/1$)
limits the range of refocus (a). The defocus for different refocusing positions is shown in b).

for the objectives of our choice. It is evident that the remote objective (0.75 NA) is more limiting to both the achievable RF range and distance with minimal defocus. Strehl ratio above 0.8 is maintained for approximately ±180 µm refocus, constituting 360 µm range of refocusing allowed by the system. The defocus introduced due to the uncompensated higher order spherical aberration at the extremities of this displacement range is approximately 10 µm. The defocus effectively causes distortion in the z-direction of the final image. This is likely to be negligible when compared to aberrations due to misalignment and is smaller than the cardiac cell dimensions in the axial direction (approximately 20 µm).

3.1.2 Choice of relay lenses and magnification matching

To achieve diffraction limited refocusing, the magnification between the imaging volume and its remote copy has to be matched and accounted for the immersion media refractive index difference $M_{RF} = \frac{n_{sample}}{n_{RF}}$, as discussed in Section 1.3.3. In our case, the remote objective is in air (with n_{RF}=1), therefore M_{RF}=1.33 for water immersion primary objective. The lens pairs between the objectives O1 and O2 were therefore carefully chosen to meet this condition. Importantly, the focal lengths of the lenses had to be sufficiently long enough to allow the folded geometry of the RF module and re-imaging of the back focal plane of the remote objective onto the galvo mirrors within the microscope chassis. Furthermore, the beam size at the back aperture of both objec-

tives has to be large enough to achieve the maximum NA. The resulting magnification for the chosen lens pairs was calculated to be M_{RF}=1.36, with a 0.03 (2.3%) mismatch from the desired 1.33 which is within acceptable range [35]. Note that a non-disclosure agreement was signed with Scientifica to obtain information on the focal lengths and the positions of the lenses within the 2-photon microscope chassis.

3.1.3 Fusion 360 design of the portable RF module

Alongside the precise positions of the lenses based on their focal lengths, the design requirements for the RF module were as follows: low footprint on the optical bench, low cost, portability and compatibility with retrofitting to other multiphoton microscopes. A CAD prototype of the RF module design was assembled first in Autodesk Fusion 360, as shown in Figure 3.2. The module comprises primarily off-the-shelf components (Thorlabs and Newport). The optics were assembled on a small breadboard (Thorlabs MB2025/M) with vibration dampening pillars (Thorlabs SWB/M) to mitigate any impact of the voice coil vibration. The two pillars (XT34, Thorlabs) employ 34 mm rail width optomechanics to hold the 30 mm cage system rods securely. The beam path is changed with mirrors in periscope mounts (KCB1/M, Thorlabs). The objective is positioned in the SM1ZA (Thorlabs) mount allowing fine tuning its axial position. This folded vertical geometry reduces the system's footprint on the optical bench. Additionally, it prevents the remote objective from sagging due to gravity, which would be the case in horizontal mounting. The voice coil actuator is positioned on the Newport tip-tilt stage (M-37 Series) to ensure the mirror surface is flat and perpendicular to the incoming beam. The custom adapter for the voice coil actuator to the tip-tilp stage was designed in Fusion 360 and machined from aluminium (Figure 3.2b).

3.2 Experimental set-up

The following sections describe in detail the excitation and detection paths in the 2P-RF system.

3.2.1 Excitation

The schematic of the 2P-RF illumination setup is shown in Figure 3.3. The power output of a pulsed Ti:Sa laser source (Coherent, Vision 2, 80 MHz, 800 nm) is attenuated with a Pockels cell (Conoptics, 350-80 LA) and is directed to a custom built single-prism pulse compressor. Efficient power coupling into the folded-geometry RF module is ensured using waveplates. The horizontally polarized beam is transmitted by the polarizing beam splitter. The quarter wave plate in the RF module is positioned with

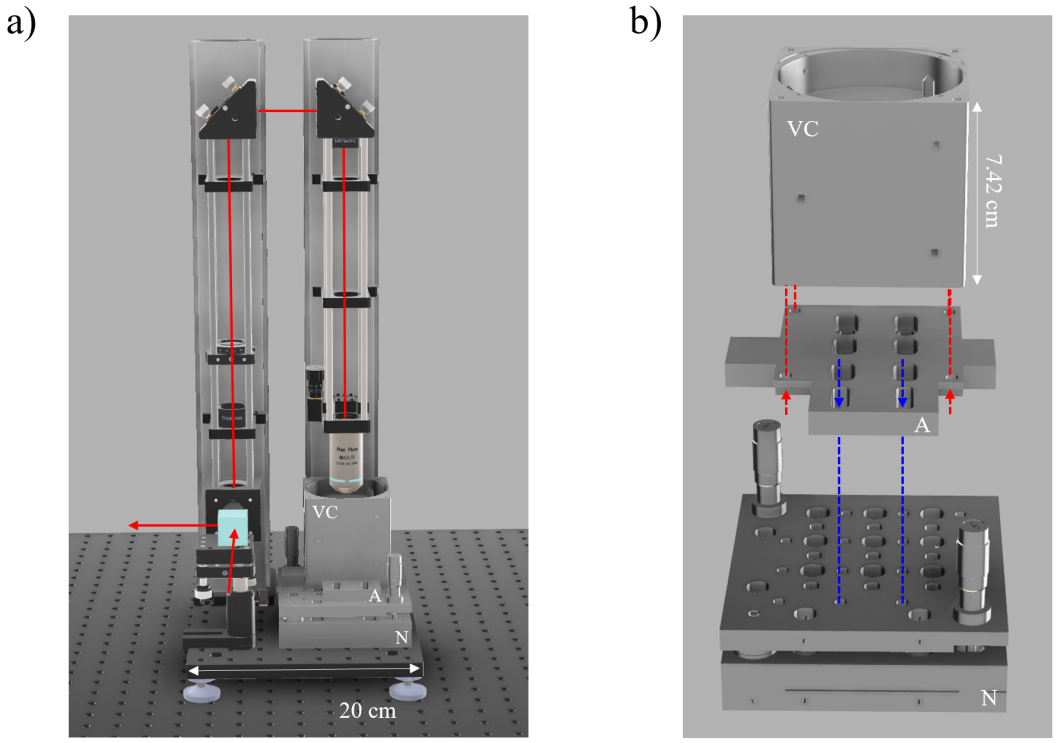

Figure 3.2: Autodesk Fusion 360 model of the portable RF module compatible with retrofitting to commercial microscopes. The full setup assembled on a 20×20 breadboard is shown in a. Red line marks the beam path, VC: voice coil actuator, A: custom adapter plate, N: Newport tip-tilt stage (M-37 Series). In b, the assembly of the adapter, the actuator and tip-tilt stage is shown. Arrows indicate the direction in which the connecting screws are facing. The extrusions on the left and the right hand side of the adapter allow additional clamping to the tip-tilt stage. 3D models of the components were obtained from the respective manufacturers.

its fast axis at 45 degrees relative to the incident polarization to obtain a circularly polarized state. The beam undergoes expansion to overfill the back aperture of the remote objective (Nikon Plan Fluor, 40X, NA 0.75, air). At its focal plane, the lightweight remote mirror (Thorlabs, UM05-0A, low-GDD mirror, 720-900 nm, 0° angle of incidence) is positioned on a linear voice coil actuator (Equipment Solutions LFA-2010 Linear actuator). The waveform generated for the microscope's fast galvanometric mirror is re-scaled and used to drive the voice coil actuator in RF imaging. Upon reflection, the circular state handedness is flipped. The quarter wave plate retrieves vertically polarised light, which the polarising beam splitter reroutes to a commercial 2-photon microscope (Scientifica, HyperScope). The microscope is controlled with SciScan 1.2 Labview-based acquisition software. Here the sample objective (Olympus XLUMPLFLN, 20X, NA 1, 2 mm WD, water dipping) is used to probe the preparation in a custom designed sample chamber filled with Tyrode's solution. The solution is kept at 21 °C and is enriched with medical grade oxygen before the experiment. As discussed in Section 3.1.2, deviations from magnification matching between the sample

and its remote copy lead to considerable deterioration of refocusing range. The lenses L3, L4, L5 and L6 with focal lengths of 125, 200, 175 and 100 mm were carefully chosen with consideration also of the telescopes inside the microscope itself.

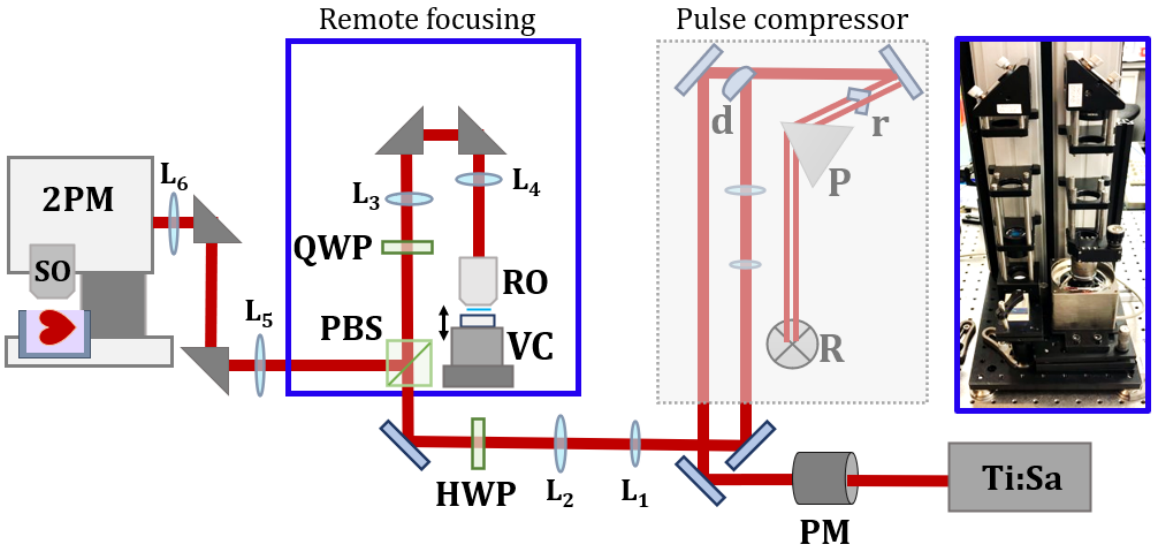

Figure 3.3: Experimental set up with an ultrafast laser as excitation source for a commercial 2-photon microscope with custom-built remote focusing and pulse compression units. QWP, HWP: quarter- and half-wave plates. PBS: polarizing beam splitter. VC: voice coil actuator. PM: power modulation. RO: remote objective. SO: sample objective. d, r: d-shaped and roof mirrors, respectively. P: prism (N-SF11 glass, Thorlabs, PS855), R: retroreflector. The arrow indicates the direction of remote mirror actuation.

3.2.2 Detection

The 2-photon microscope operates in epi-fluorescence mode and the generated fluorescence is collected with the sample objective. The primary dichroic mirror (665 nm) redirects the emission light to an Olympus UME-1 fluorescence cube after an IR blocking filter (680 nm). Another dichroic (DMLP605R, Thorlabs) reflects the entire Fluovolt emission range to the first PMT with a higher sensitivity for green wavelengths (Hamamatsu H10770B-40). This is to ensure the best possible detection efficiency. The long wavelength collection with a single red-sensitive PMT is used for autofluorescence (Hamamatsu H10770B-50). The signal from the PMTs is digitised with a data acquisition board connected to National Instruments PCI-6110 card, allowing 12-bit imaging.

3.3 Alignment of 2P-RF system

As described in Section 1.4.1, alongside magnification mismatch, misalignment of RF system components deteriorates the refocusing range achieved. Careful consideration

of the telecentricity as well as positioning of the remote objective and its tube lens is critical [37]. Nevertheless, when the dimensions of the cardiac cells are considered, the requirements are less strict as a degree of tolerance of some tens microns is allowed. A typical cell is around 200 µm and 20 µm in width and height, respectively. Resolving sarcomere spacing requires sufficient precision and resolution, while cell membrane can be visualised easier. Importantly, for the primary purpose of AP tracing, the requirements are even less stringent - the distortion due to misalignment or residual magnification mismatch should not exceed the dimensions of cardiac cells.

3.3.1 Alignment of RF module components

Alignment mode of the Ti:Sa laser is used to correctly position RF module optics. Firstly, the incident beam height is fixed with two irises. The module breadboard is positioned perpendicular to the incident beam and with no lenses in, using SM1 fluorescent disks (Thorlabs, VRC2D1), the beam is aligned parallel to the vertical cage rods. The remote mirror is placed on the VC actuator in enabled state, midway through its travel range. The tip and tilt stage is adjusted so that the mirror is flat (the reflection travels along the path of the incoming beam). The remote objective (RO) is inserted in a z-axis translation mount (Thorlabs, SM1ZA). A 50:50 beam splitter is introduced so that the back-reflected beam is directed to a shearing interferometer (Figure 3.4). The objective's axial position is adjusted until the fringes are parallel to the indicated line. This implies that the remote mirror is in the focal plane of the objective, as both the incoming and back-reflected beams are collimated. Relay lenses (L) are then introduced following the same method. Note that in practice the fringes are not entirely straight and curve slightly at the edges due to a small residual amount of spherical aberration after the double passage through RO. Once the lenses are in place, the polarising beam splitter is inserted, redirecting the beam perpendicularly into the Scientifica microscope periscope (Figure 3.3).

3.3.2 Alignment of RF module to the microscope

The lens pairs shown in Figure 3.3, namely L3-L5 and L5-L6 need to be in telecentric alignment. To achieve this, the beam is rerouted in the opposite direction so that it approaches L5 and is collimated by L3. The shearing interferometer is used to ensure they form a 4-f system. The same for the L5-L6 lens pair is also verified separately.

Within the microscope it is necessary to reimage the back focal plane of the remote objective onto the first galvanometric mirror. The position of the mirror with respect to the chassis was obtained by signing a non-disclosure agreement with Scientifica. Nevertheless, it is difficult to place L6 correctly. Collimation cannot be verified with

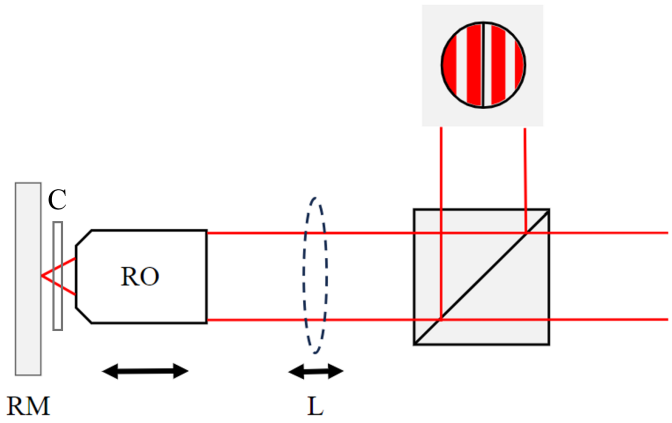

Figure 3.4: Alignment of focusing elements in RF module. A 50:50 beam splitter directs the reflected beam to the shearing interferomenter. Fringes parallel to the reference line indicate that the beam is collimated. RM: remote mirror, RO: remote objective, C: coverglass, L: lens.

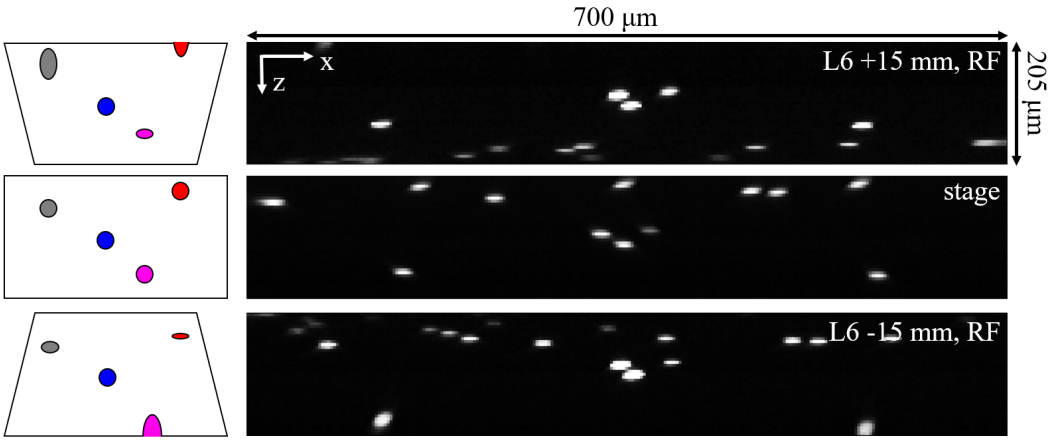

Figure 3.5: Effect of L6 axial displacement on axial magnification. On the right, summed intensity projection of resliced z-stacks is shown for RF (top and bottom) and microscope translation stage (middle) scans. At extreme cases of L6 axial displacement (±15 mm from the starting position), a significant axial magnification gradient is present. Images have their contrast adjusted.

a shearing interferometer, as after the microscope the beam is expanded with its intensity is not concentrated enough to observe the fringes. Therefore, L6 is tentatively positioned with calipers and its correct location is determined by imaging a preparation with fluorescent beads (Dragon Green, 7.32 µm in diameter, Bangs Laboratories, FSDG007) suspended in 1% agarose. As shown in the exaggerated cases of Figure 3.5 (±15 mm displacement of L6 in the top and bottom images, respectively), the axial magnification gradient is inverted across the nominal L6 position. By displacing L6 incrementally and comparing a maximum intensity projection of a resliced z-stack obtained with the microscope's translation stage to the RF scan equivalent, the best overlap of the two can be found (further discussed in Section 3.3.3). If the optimal

placement of L6 is significantly different from its starting point, L5 and L6 as well as L5 and L3 pairs should be re-aligned telecentrically. This requires iteratively translating the module closer or further to the microscope.

3.3.3 Comparison of microscope stage and RF scanning

To investigate the residual distortion in the 2P-RF system, 7.32 µm Dragon Green beads in 1% agarose suspension were prepared. Multiple x-y planes were imaged at different z depths and summed in a resliced projection, as shown in Figure 3.6. The red and blue channels correspond to RF mirror refocusing and conventional refocusing by translating the sample objective, respectively. The agreement of positions of stuctures is seen in the overlay. Around z=0 (RF mirror in zero RF position), there is good match in lateral and axial positions of the beads (magenta). However, towards the extrema of the scan, a lateral shift is visible. Axial position mismatch is smaller and is non-uniform throughout the refocusing depth. As in Figure 3.6b), at the extrema of the scan within the central region of the FOV (dashed red ROI) the discrepancy of the central bead positions is well within cardiomyocyte dimension, as the largest lateral (white) and axial (cyan) discrepancies are 30 µm and 15 µm respectively. As the microscope's primary aim is to perform line scanning to trace the APs along the centre of the FOV, discrepancy at the edges of the FOV can be disregarded. For minimal distortion, the scan range of ±50 µm from nominal RF position could be chosen.

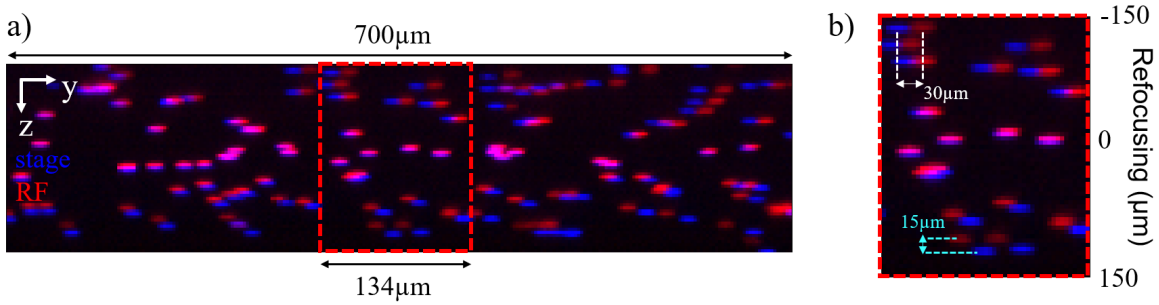

Figure 3.6: RF-induced distortions are well under cardiac cell dimensions: a) a RF (red) and microscope stage (blue) scan of 7.32 µm bead suspension in 1% agarose is shown. b): At the scan extrema within the central region of the FOV, lateral and axial shift of bead position is approx. 30 µm and 15 µm, respectively.

The residual distortion shown in Figure 3.6 implies alignment errors. Firstly, uncertainty in position of L6 could have contributed. Additionally, the nominal mirror position could have been misplaced towards negative refocusing and the beads close to z=0 region only overlap as a result of a slight axial magnification gradient. Attempts were made to find the optimal overlap and fix the lateral shift which was presumed to be due to tilted RF mirror position. Subsequently altering the aforementioned in

small increments and repeating the scan did not show improvements without making the back-reflection from the remote mirror follow a significantly different trajectory. Due to the scale of the distortion and the dimensions of cardiac cells, the alignment in Figure 3.6 was accepted.

Finally, the sample objective cannot be positioned with its back focal plane and the rear focal plane of the remote objective re-imaged onto one another. This location is physically inaccessible within the microscope chassis. The back focal plane location of the Olympus XLUMPLFLN 20X objective is $-48.1\,\text{mm}$ (inside the objective barrel). In practice, we move the sample objective stage as close as possible to the chassis, ($300\,\mu\text{m}$ below its highest allowed position). Nevertheless, the mismatch between this position and the back focal plane at the focal length of the tube lens (subject to non-disclosure agreement) is estimated to be up to several centimetres. The precise distance between the objective and the tube lens is unknown (not disclosed). While this does not impact conventional 2P imaging with an infinity corrected objective lens, in remote focusing this mitigates the achievable diffraction-limited range [37], further discussed in Section 3.4.

3.4 Assessment of 2P-RF system resolution

An important and more precise measure of system performanc is the point spread function (described in Section 1.1.4). The larger the refocusing, the more significantly the 2^{nd} order spherical aberration contributes to the degradation of the PSF.

Microscope resolution was evaluated by imaging sub-resolution 0.196 nm diameter Dragon Green fluorescent beads (Bangs laboratories, FCDG003). The beads were suspended in distilled water and to prevent formation of clumps, the eppendorf was submerged in an ultrasonic bath (Grantt instruments) for 10 minutes. A small drop of water-bead solution was then placed on a microscope coverslip which and allowed to evaporate for the beads to adhere to the coverslip. A droplet of water was then added carefully for the water dipping objective. Some beads were detached from the coverslip, however most remained stuck for imaging. This method was more reliable than suspending the beads in 1% agarose as the focal spot of the high NA 2PM melted the agar and caused the beads to drift, at the power levels required to get enough signal intensity. Z-stacks were obtained at different positions of the remote mirror. The coverslip with beads was placed on a vertical translation stage to bring it back to focus. Z-stacks were resliced and then summed-projected in Fiji (ImageJ). A line profile was used to select intensity values axially and laterally over the visible beads. MATLAB was used to fit a Gaussian function and retrieve the axial and lateral FWHMs. An example of such fits for $0\,\mu\text{m}$ and $-100\,\mu\text{m}$ refocusing is shown in Figure 3.7. At

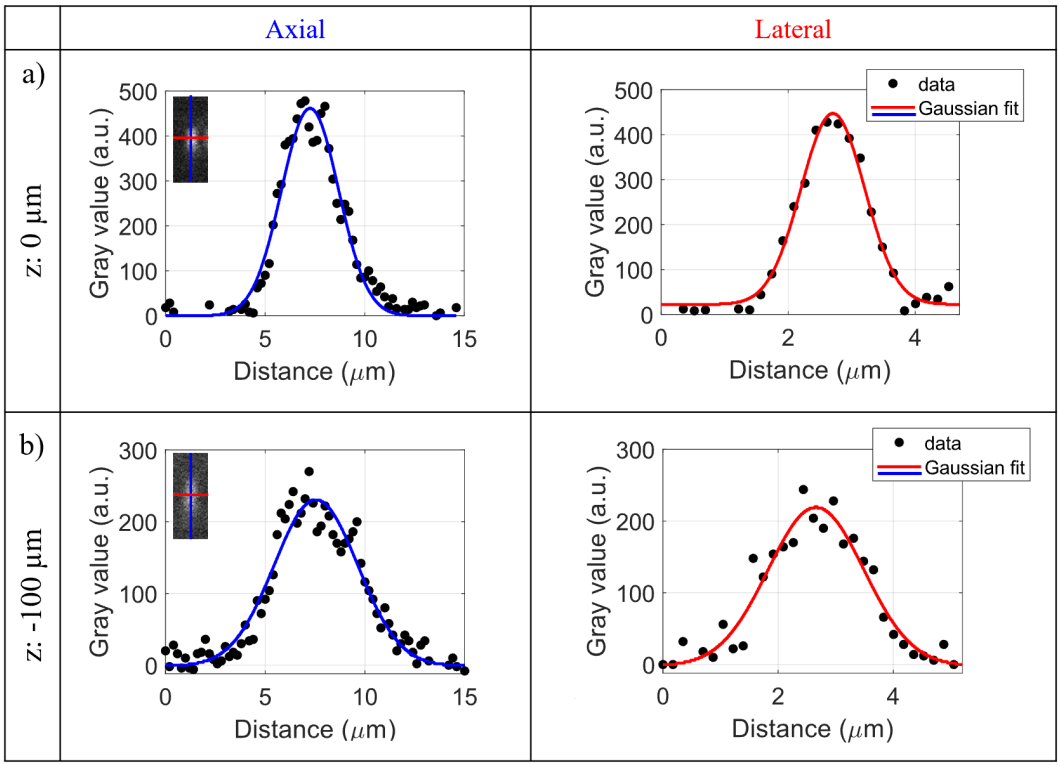

Figure 3.7: Example of PSFs at 0 µm and -100 µm refocusing shown in a) and b), respectively, measured by imaging sub-resolution beads. Black markers denote the data points and the solid lines show the corresponding axial (right) and lateral (left) fits.

RF mirror position of zero remote-refocus (Figure 3.7a), the axial FWHM was fitted as 3.37 µm and lateral as 1.74 µm; the corresponding goodness of fit was R^2=0.953 (axial) and R^2=0.929 (lateral). At -100 µm refocusing (Figure 3.7b), 4.83 µm axial and 1.74 µm lateral FWHMs are estimated with 0.813 and 0.927 R^2, respectively. The corresponding variation of resolution across the full range of 200 µm is displayed in Figure 3.8. The uncertainty was estimated as the standard deviation of the FWHM values of the beads visible in each resliced z-projection for a given RF depth (2<N<7). Both the lateral and axial PSFs degrade towards the extrema of refocusing range; it can be considered acceptable when cardiomyocyte dimensions are considered. Additionally, in the central range of approximately 100 µm the axial PSF is under 5 µm. Comparing these results to the 360 µm theoretical diffraction limited range, established in Section 3.1.1, it is evident that significant degradation is present. Furthermore, when the 2P microscope resolution is estimated using the same method and bypassing the remote focusing module, axial and lateral fits return 2.35 µm and 1.08 µm, respectively. This renders the axial and lateral resolutions after including RF module 43.4% and 16.7% worse at zero remote-refocus mirror position. While the most significant culprit is the previously discussed mismatch of the pupils of the sample and remote objectives,

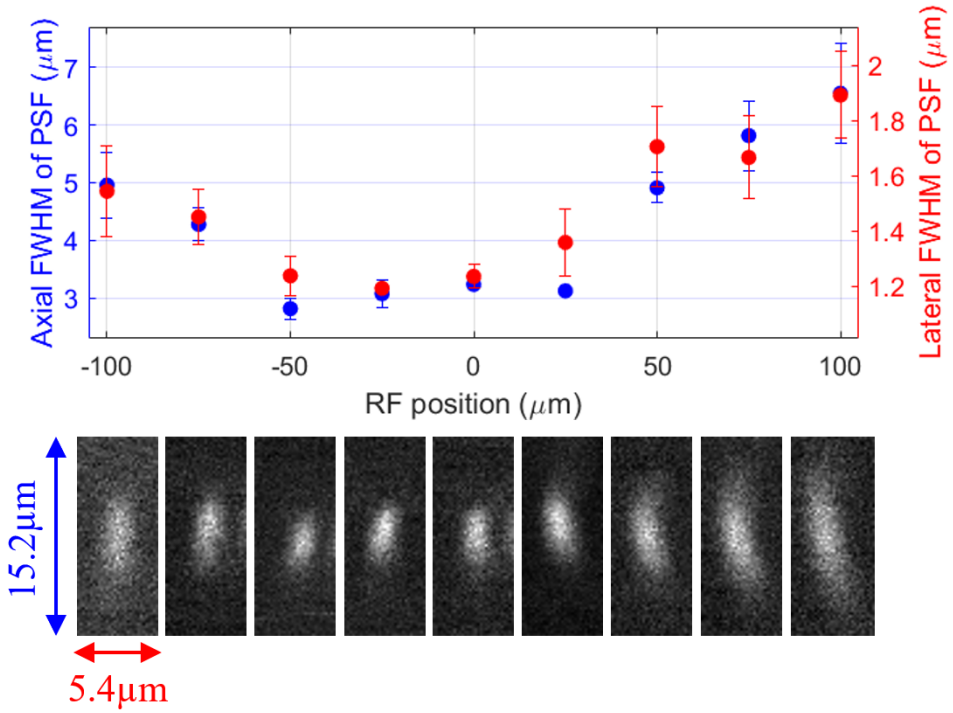

Figure 3.8: Resolution variation over RF range obtained by imaging sub-resolution fluorescent beads. Below 5 µm axial resolution over the range of 100 µm refocus is maintained. In lower panel representative ZX projections of a single bead at the corresponding RF position are shown.

it is also possible that during the scan, the beads drifted in their axial position due to the laser focus. If the precise position of the lens with respect to the chassis was disclosed by the manufacturers, a symmetric displacement of the remote objective with respect to its tube lens could cancel out the effect. Nevertheless, considering the height of a cardiomyocyte (20 µm), the 100 µm with under 5 µm resolution is sufficient and coincides with the refocusing range with minimal axial and lateral distortions (Figure 3.6).

3.5 Power throughput of the 2P-RF microscope

To achieve diffraction limited refocusing, all the optics shown in Figure 3.3 are required. A large number of optical elements warrants an assessment of the system power efficiency; this is particularly relevant for imaging deep in highly scattering cardiac samples. While the average power needed is highly preparation, numerical aperture, pulse duration and wavelength dependent, in [58], to image 300 µm deep in FluoVolt-stained mouse ventricular myocardium approximately 22 mW were used with 840 nm excitation light and NA=1 objective. In our 2P-RF system, due to the high power output at 800 nm of the Ti:Sa laser, optical losses before the remote mirror are

not limiting. However, when the remote mirror is at the zero remote refocus position, the beam is focused onto its surface with a 0.75 NA objective, resulting in etching if the power density is too high (Figure 3.9). This is a significant issue in 2P-RF systems [6, 41] and optical losses after the remote mirror must be minimised to achieve sufficient power at sample. Power measurements in the following section were carried out with a photodiode power sensor (Thorlabs, S121C).

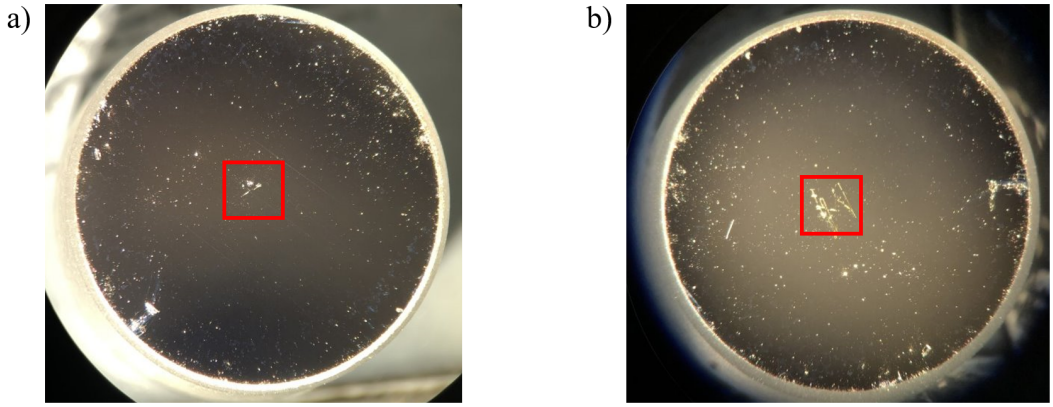

Figure 3.9: Etching due to tight focusing of the laser beam (approximately 15 mW average power) at the remote mirror position of zero refocus. A half-inch protected silver mirror (Thorlabs, PF05-03-P01) was placed under the remote objective with high incident average power. After moving it around, more damage on its surface was observed under a dissection microscope (b).

3.5.1 Optical losses

By considering of the expected losses of all components in the optical path it is possible to estimate how much power can be delivered at the sample. Each achromatic lens in the set up has an anti-reflection coating for infrared light (Thorlabs, B-coating, average reflection is less than 0.5% for 650 - 1050 nm wavelengths). Objective lenses incur most significant losses - 69% and 75% of power is retained with the sample and remote objectives, respectively, the latter traversed twice. For $\lambda = 800$ nm protected silver mirrors yield a 4.5% power loss with each reflection. Therefore, ultrafast enhanced silver coated mirrors (Thorlabs, UM10-AG) were used instead, yielding <0.5% absorption upon each incidence. It was estimated that this change reduces mirror-associated power loss from 24.1% to 4%. As shown in Figure 3.10, if the power incident to the RF module constitutes 100%, 31.5% is transmitted through the RF module and directed to the Scientifica microscope. The microscope's optics and the sample objective further reduce this to 15.9%. This is close to estimated values; possible contribution to the the discrepancy could have been the different transmission properties of the optics inside the microscope (precise specifications unavailable, Thorlabs IR coating and protected

silver mirrors were assumed).

Importantly, a broadband, ultrafast, 0° angle of incidence dielectric mirror (Thorlabs, UM05-0A) with a centre wavelength of 800 nm was used as the remote mirror. The aforementioned mirror change from protected silver to dielectric enhanced available power at sample by 3.3 times (from 6.6 mW to 22 mW) at λ=800 nm before RF mirror was etched. This is comparable to the average power used to image mouse myocardium at up to 300 µm depth in [58].

Typically, dielectric mirrors are used with a collimated beam and with minimum deviation from their nominal angle of incidence. It should be noted that 0.75 NA focusing yields k-vectors of arcsin(0.75) = 48.6°. As the angle of incidence strays from the nominal value, the central wavelength for the dielectric mirror also shifts. Additionally, reflectance can also change as a function of angle of incidence. Therefore, rays focused from the edges of the beam may undergo losses, effectively decreasing the NA of the system. Nevertheless, the broad range of the UM05-0A mirror (700 - 930 nm) is expected to prevent that.

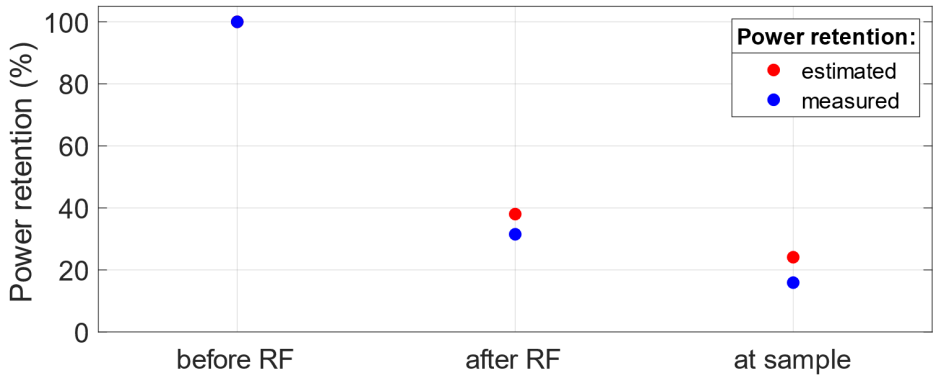

Figure 3.10: Optical power retention in the set up. As we are not limited by the power before the beam enters the RF module, the incident power is 100%. After the module, 31.5% of power retention is measured (blue). After passage through the microscope and the sample objective this is further reduced to 15.9%. The estimated power retention (red) is 38% and 24.1% after the RF module and at sample, respectively. Each data point was acquired with a power meter measurement averaged over 10 s.

3.5.2 Losses due to aperture clipping

In addition to back-reflection and absorption, beam clipping due to apertures can introduce losses. When the RF mirror is displaced from its nominal position, beam size incident on the optics changes. The key limiting elements here are the quarter wave plate (0.5 inch diameter) and x galvo mirror (3 mm in diameter). In Figure 3.11, the normalised power at sample for different RF mirror displacements, measured after the PBS in the RF module and after the Scientifica microscope is shown. Power loss

due to clipping is below 10% over a refocusing range of 200 µm. Additionally, as the power change follows the same trend before and after the microscope body, apertures within the Scientifica microscope do not introduce additional losses along the useful range of RF scan (approximately ±50 µm). As this behaviour is reproducible, in the future implementations of the system, a power modulation gradient could be applied on the Pockel's cell drive voltage to compensate for the aforementioned losses and achieve uniform power at sample throughout the extended refocusing range.

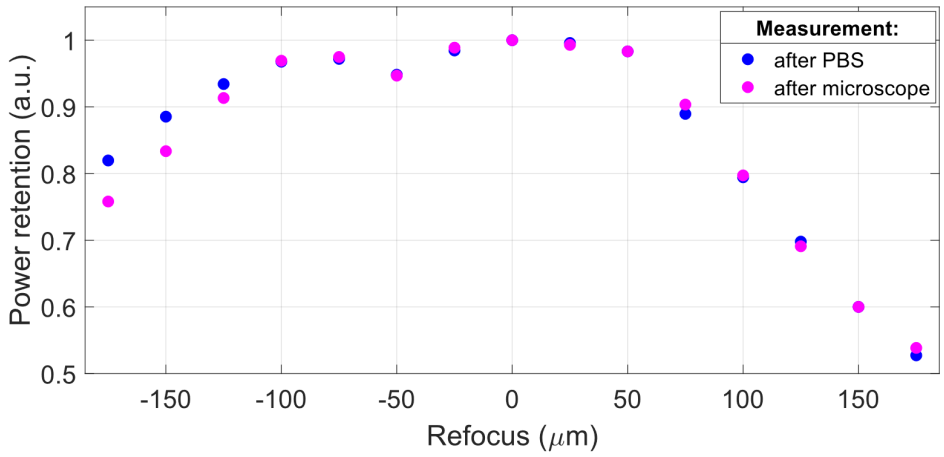

Figure 3.11: Loss due to aperture clipping of the beam over the refocusing range in the Scientifica 2P microscope. The range of over 80% transmission is approximately 280 µm. Each data point was acquired with a power meter measurement averaged over 10 s. The error bars are not shown as the uncertainty of the power measurements was in the scale of a few µW and therefore negligible compared to the values measured.

3.6 System dispersion management

It is evident that the power available at the sample in the 2P-RF system is limited. As discussed in Section 1.1.3, temporal pulse elongation due to dispersion is a prominent issue in multiphoton microscopes as the laser beam propagates through optical elements such as lenses and objectives. The efficiency of 2-photon absorption induced fluorescence depends strongly on pulse duration, thus achieving a transform-limited pulse is critical with the increased complexity of additional RF optics. Most commonly, pulses of around 100-140 fs are used in 2PM [2].

Using fewer optical components mitigates group delay dispersion, but in 2P-RF module it is unavoidable. Firstly, the achromatic doublets are comprised of convex and concave lenses cemented together to correct for chromatic aberration. Generally, they are thick (around at least 10 mm). The 6 nm bandwidth of the laser pulse will not cause significant chromatic aberration when using thinner non-achromatic lenses. However, focal length shifts for different wavelengths within the laser's tunable range for different

fluorophores would occur if achromatic doublets are not used, potentially skewing the alignment of the RF system. Importantly, the sample and remote objectives also introduce significant GDD. In essence, remote focusing systems (introduced in Section 1.3.2) make up three microscopes instead of one.

Pulse compressors exploit angular dispersion of prisms or diffraction gratings to induce negative GDD. For the former, the apex angle β and the angle of incidence ϕ_0 can be defined. When light is incident on an interface between two media with different optical properties, a portion of it is transmitted (refracted) and a part of it is reflected, according to the Fresnel equations. The Brewster condition states that for P-polarised light, where the electrical field oscillation is parallel to the plane of incidence (and perpendicular to the optical surface), there is an angle of incidence ϕ_0 at which no reflection occurs. With S-polarisation, reflection losses are larger and there is no angle ϕ_0 with no reflection. The polarising (or Brewster) angle is wavelength and material dependent, expressed as

$$\theta_{\mathrm{B}} = \tan^{-1}(\mathrm{n}_2/\mathrm{n}_1). \tag{3.3}$$

For the N-SF11 glass (Thorlabs, PS855) prism, the refractive index at 800 nm is n_2=1.7646 [60] and θ_B=60.4597°. The following section details the 2P-RF system dispersion estimation and management.

3.6.1 2P-RF system dispersion estimation

Dispersion in the set up was estimated by considering the material and thickness of each optical component. GVD value for different wavelengths and glasses was found at the Refractive Index Information Repository [60]. The information on thicknesses and geometry of each optical component was obtained from the manufacturers. For example, at $\lambda = 800\,\mathrm{nm}$, a Thorlabs achromatic doublet, AC254-125-B-ML, consists of 6 mm of N-BK7 and 6 mm of N-SF8 glasses with GVD of 44.651 fs^2/mm and 134.06 fs^2/mm, respectively. A single passage through the lens therefore incurs extra GDD of 1072.266 fs^2. The resulting pulse elongation can be calculated as

$$\tau = \tau_0 \sqrt{1 + \left(4 \ln 2 \frac{\mathrm{GDD}}{\tau_0^2}\right)^2} \tag{3.4}$$

where τ_0 is the initial pulse duration. Estimated dispersion of different parts of the microscope system is displayed in Table 3.1. The RF module is expected to contribute a significant 15 226 fs^2 to the total GDD. Overall, the optics of the RF module and Scientifica microscope frame are likely to broaden the pulse approximately 4 times, from 140 fs to 572 fs at 800 nm

	Cummulative GDD (fs^2)	**Estimated pulse duration (fs)**
Initial pulse duration	0	140
Before RF module	5499	177
After RF optics	20726	434
At the sample	28011	**572**

Table 3.1: Estimated GDD incurred and resulting pulse duration in the 2P-RF system.

Note that this estimation is approximate. Firstly, the GDD induced by the sample and remote objectives was obtained from the manufacturers, who offered a calculated value, based on design parameters, not a measured one. Additionally, GDD induced within the Scientifica microscope by the relay telescope between the galvo mirrors as well as the scan and the tube lenses was approximated based on commercially available options on Thorlabs. The information on their dispersion was not subject to non-disclosure agreement. Finally, any sample-induced dispersion is neglected.

3.6.2 Implementing a single prism compressor for the 2P-RF system

As Coherent Chameleon laser allows for $-22\,515\,\mathrm{fs}^2$ compensation at 800 nm, a custom single prism pulse compressor [9] was built to supplement that, based on the model proposed in [9] (Figure 3.12). The picture of the assembled setup is displayed in Figure 3.13.

Using a protractor, the angle of incidence ϕ_0 to the prism was selected to be approximately 60.5°, following Equation 3.3. The rotation stage on which the prism was mounted allowed fine tuning so that the beam leaving the prism travels parallel to the breadboard on which the compressor was built. Adjustment of a HWP before the compressor allowed to identify optimal polarisation by minimising reflection intensity. Note that as the system is not power-limited before the remote mirror, therefore some reflection loss is acceptable.

Firstly, the compressor on its own was characterised (the beam was directed through the Pockels cell and Chameleon laser precompensation was set to $0\,\mathrm{fs}^2$; this is close to the shortest measurable pulse length immediately after the laser output). A commercial APE Mini TPA autocorrelator was used to measure the pulse duration. Four scans were averaged to acquire the autocorrelation function. A sech^2 fit was assumed for femtosecond pulses. In Figure 3.14, an example of the autocorrelation (black) and the corresponding sech^2 fit (red) is shown for the $145\pm(3.3\times10^{-2})$fs pulse (autocorrelation function FWHM is 225 fs).

Measured pulse duration with increasing separation between the prism and the

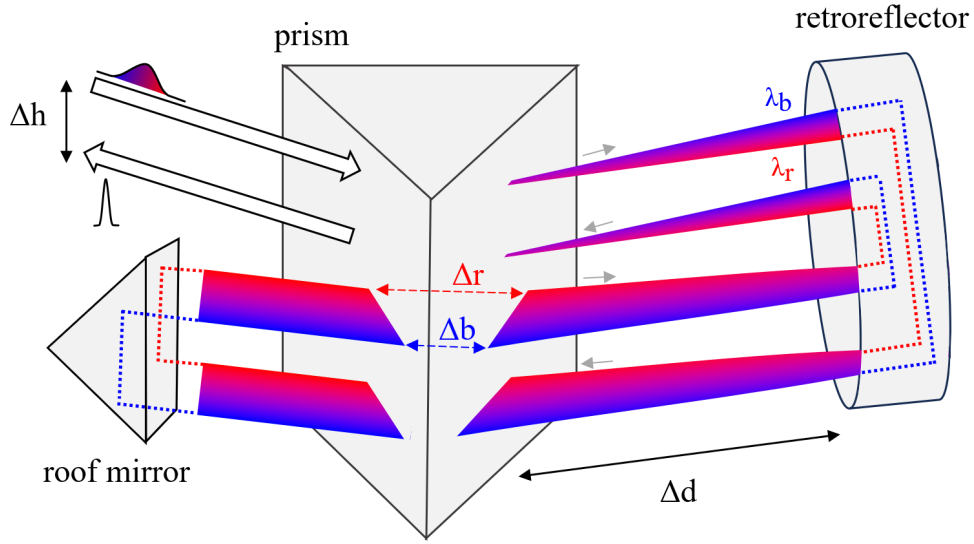

Figure 3.12: Schematic of a single prism compressor. A dispersed pulse with a positive chirp enters the prism where the refraction angle for short λ_b and long λ_r wavelengths is different. As it is redirected back to the prism via a retroreflector, the λ_r component traverses a longer distance (Δr) in highly dispersive glass compared to λ_b (Δb). This results in pulse compression, as λ_b wavelengths that were lagging behind catch up with the long wavelength component within the pulse. As λ_b is still slowed down by the glass more than λ_r, a balance must be struck between the angle of refraction and the distance the beam travels in the prism. The compressed pulse leaves the prism at a different height Δh and can therefore be spatially separated from the incident beam. Note that the larger the distance Δd between the prism and the retroreflector is, the more negative GDD can be induced, as the spatial separation of λ_r and λ_b components increases. *Adapted from* [9].

retroreflector, Δd, as well as the corresponding negative GDD incurred by the compressor is shown in Figure 3.15a) and b), respectively. It is evident that the shortest pulse duration is achieved at approximately Δd=35 cm with $-7804\,\mathrm{fs}^2$ GDD compensation. This evidences the dispersion induced by the Pockels cell. As the RF optics are added into the light path, Δd needed to achieve the optimal duration will be larger even when the laser's inbuilt precompensation is employed. Overall, the compressor could compensate for up to $12000\,fs^2$ GDD by moving the retroreflector by 46 cm.

It is complicated to quantitatively measure the pulse duration at the sample directly after the microscope optics and the sample objective. After the objective, the divergence angle is very large. Even if the objective is removed, the expansion of the beam to overfill the back aperture of the objective is significant and additional optics would be needed to direct it to an autocorrelator, potentially skewing the measurement. An in-line photodiode-based autocorrelator set up was built by another PhD student Lewis Williamson and used to measure the pulse duration in various locations within the system. The following results are stated in this Thesis for completeness only. For

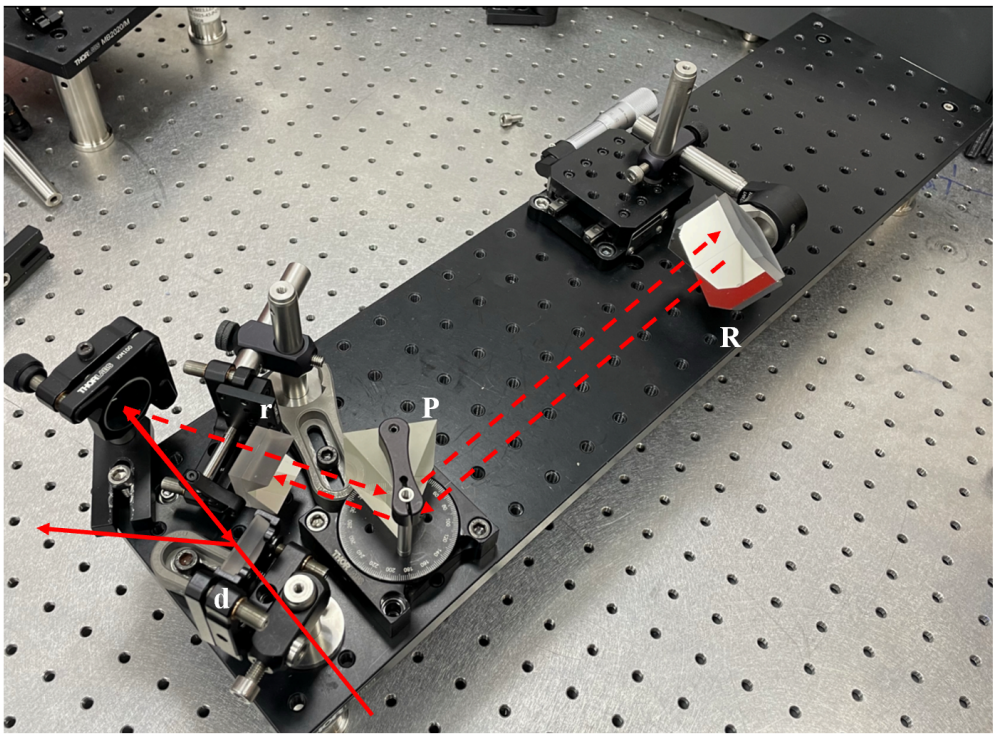

Figure 3.13: The assembled single prism compressor. Solid red line indicates the beam path. Dashed lines denote double passes for simplicity. d, r: d-shaped and roof mirrors, respectively. P: prism (N-SF11 glass, Thorlabs, PS855), R: retroreflector. *Picture taken by Lewis Williamson (PGR) and adapted by me.*

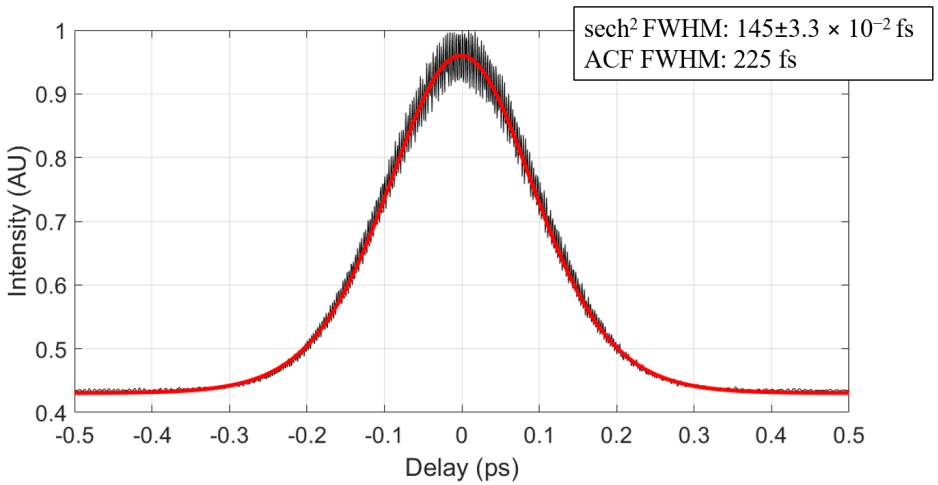

Figure 3.14: Example autocorrelation trace (black) from APE Mini TPA. The corresponding sech^2 fit (red) is shown for the $145\pm(3.3\times10^{-2})$fs pulse (autocorrelation function FWHM is 225 fs). Signal-to-background ratio > 2.

details on in-line autocorrelation, the interested reader should refer to [59]. After the Pockels cell, the pulse is broadened from 140 fs to 172 fs. After the sample objective, the pulse duration was measured to be 487 fs at the sample, which is 85.14% of the estimated value. The pulse is compressed down to 156 fs at sample when employing full

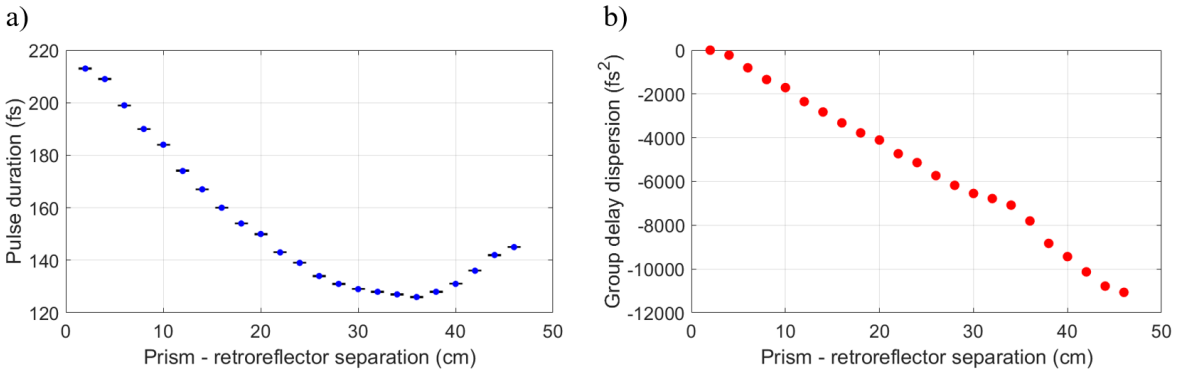

Figure 3.15: Pulse compressor characterisation: a) pulse duration without any laser precompensation with different Δd distances between the prism and retroreflector measured with the APE autocorrelator, assuming a sech^2 pulse shape. The error bars denoting the mean square error on the fit are negligible. In b), the corresponding negative GDD incurred with the compressor is shown (calculated using Equation 3.4).

laser pre-compensation and setting Δd distance to approximately 40 cm. This is 16 fs longer than the pulse coming from the laser and 19 fs longer than the minimum value achieved after the compressor with no additional optics. This was deemed acceptable as significant compression was achieved.

Ensuring maximum fluorescence intensity at sample

If not aligned properly, prism-compressors may deteriorate the beam profile (by elongation perpendicular to the propagation direction or clipping of the beam). To ensure that fluorescence efficiency is indeed increased when the compressor is utilised, a sample of Fluorescein (Sigma Aldrich, 46960) in distilled water at a concentration of 10 mg/100 ml was prepared. The diffusion of liquid in the bath recirculates it thus countering any bleaching effects. While the prism and retroreflector separation was kept fixed, the laser's GDD compensation was altered. It was ensured that the power at the sample was the same for all measurements (8.91 mW average over 10s; the standard deviation was under 100 µW and deemed negligible, as measured with Thorlabs S121C powermeter). For each GDD value, 20 frames (1.907 fps) of 37 µm $\times$ 37 µm dimensions in the fluorescein bath (Figure 3.16a) were obtained. The background was subtracted from the averaged frames and the resulting mean gray value was determined for each GDD precompensation setting. The uncertainty on the mean gray value was estimated from the FWHM of the Gaussian fit of the histogram of the mean frame (Figure 3.16b). The normalised results are shown in Figure 3.17. At the same average power at sample the peak mean gray value achieved is almost 2 times larger when using the pulse compressor. Therefore any deterioration of beam quality incurred by the prism compressor is negligible. It should be noted that long distance of travel in

air leads to beam expansion. Therefore an extra telescope after the prism compressor was used to demagnify the beam.

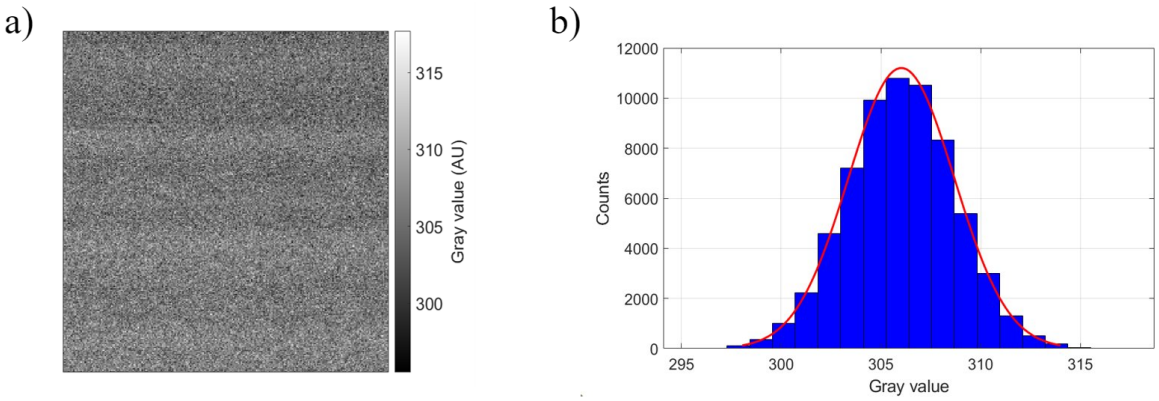

Figure 3.16: Representative x-y frames of fluorescein in water a). The corresponding histogram used to estimate the peak intensity value (306) and its uncertainty (σ=2.66, FWHM is $2\sqrt{2 \cdot \log(2)} \cdot 2.66019 = 6.2643$) in MATLAB is shown in b).

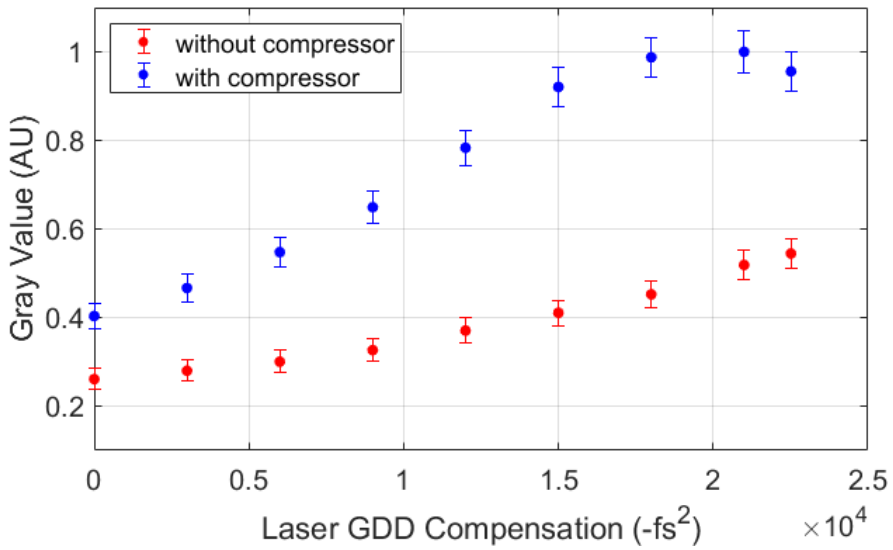

Figure 3.17: More fluorescence is excited at the same average power (8.91mW) in a fluorescein sample when the compressor is utilised.

3.7 Temporal properties of 2P-RF system

The temporal characteristics of the VC used to facilitate axial refocusing and how they impact the imaging performance is discussed in the following section. In Section 3.7.1 the working principles of the device are outlined. Then, the ability of the VC to execute scanning waveforms at increasing frequencies is discussed (Section 3.7.2) and

the considerations of synchronising remote axial scanning with the Scientifica system (Section 3.7.3) are detailed.

3.7.1 Working principle of voice coil actuators

Voice coil actuators are a type of electro-mechanical motors that can move mass in a straight line or rotationally. For the purpose of this work, linear motion is considered. A schematic of the working principle of these devices is displayed in Figure 3.18. VCs employ two key components: a permanent magnet and a moving coil, to generate the driving force, yielding high acceleration and frequency. Furthermore, as the moving components are not physically in contact with the stationary parts and the driving electrical waveform is converted directly to magnetic force, a motion profile that is virtually cogging- and hysteresis-free can be achieved [61]. The linearity and reproducibility of positioning is higher than in devices that employ gears.

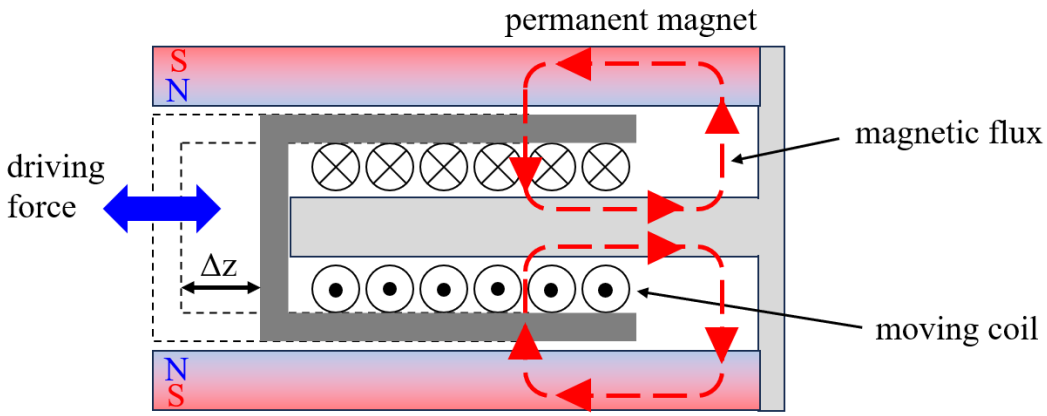

Figure 3.18: Illustration of the working principle of voice coil actuators. A permanent magnet is fixed in the device. A moving coil is attached to a lightweight frame. When a current is passed through the coil, magnetic flux is induced. Depending on the direction of the current, the induced magnetic flux direction changes, causing the stage to move. Dots and crosses denote the coil current flow direction towards and away from the page, respectively. *Adapted from* [61].

The motion in VC devices is due to the Lorentz force. For a current (I) carrying wire, it is defined as the cross product of the length of the wire segment (L) and the magnetic flux density (B), with N the number of conductors and k material related constant:

$$F_L = kNI(L \times B).$$

Assuming that friction and other obstructing forces can be overcome, this wire would experience displacement in the direction of F_L. In VCs, the permanent magnets facing the coil are all the same polarity (as shown in Figure 3.7.1). The central pole

is a ferromagnetic core completing the fixed magnetic field permeating the moving coil. If the magnetic flux density is constant (as is the case in VCs), the amplitude and direction of the magnetic force scales proportionally with the current applied to the coil (or by the changing voltage waveform imparted across the two coil leads). Desired motion characteristics and stroke lengths can be achieved with a different coil length or permanent magnet choice while ensuring uniform translation throughout the travel range of the coil. Commercial VCs have travel ranges of some millimetres (Equipment Solutions LFA-2010 Linear actuator) to several centimeters (VC500/M, Thorlabs). Voice coils are commonly used in loudspeakers as the electrical waveform can be converted to sound waves. As discussed in Section 1.4, voice coil actuators have been employed in multiple published RF systems [39, 42, 43].

3.7.2 Frequency response

For an actuator, the frequency response describes its steady-state response to sinusoidal driving wavefronts and how well they are executed or, in the case of VCs, converted to mechanical translation.

Frequency response of the Equipment Solutions LFA-2010 voice coil actuator was characterised by recording the feedback waveform which is scaled to the same voltage range as the commanded waveform and is directly proportional to the motor position. The electronic circuit board of the device contains test points corresponding to the commanded and feedback positions; these were recorded with an oscilloscope connected to the points. The remote mirror as well as its mounting screws were present on the VC stage to account for the impact of the inertia on the motion.An example of such a trace for 120 Hz actuation at 550 mV amplitude is displayed in Figure 3.19. Both the commanded and the feedback signals are of approximately the same amplitude. It should be noted that while the resulting mechanical motion approximates the commanded triangular wave, it will always tend to a sinusoid. When facilitating RF scanning for imaging, a larger scan amplitude was generally chosen (overscanning) to compensate for the rounded motion profile at the extremities of the scan and allow more of the sample to stay within the linear region of motion.

Triangular voltage waveforms (as are used in bidirectional refocusing) of four amplitudes (50, 100, 150 and 200 mV) and frequencies from 20 Hz to over 300 Hz were generated with a simple signal generator and passed to the VC actuator. The recorded feedback traces were analysed in MATLAB. Firstly, the removal of high-frequency noise (>360 Hz) was carried out by application of a low pass filter. Secondly, the mean peak-to-peak amplitude was extracted for each frequency trace by subtracting the voltage value of all peaks and throughs (identified with MATLAB's findpeaks() function). The data points and the interpolated response curves are shown in Figure 3.20a.

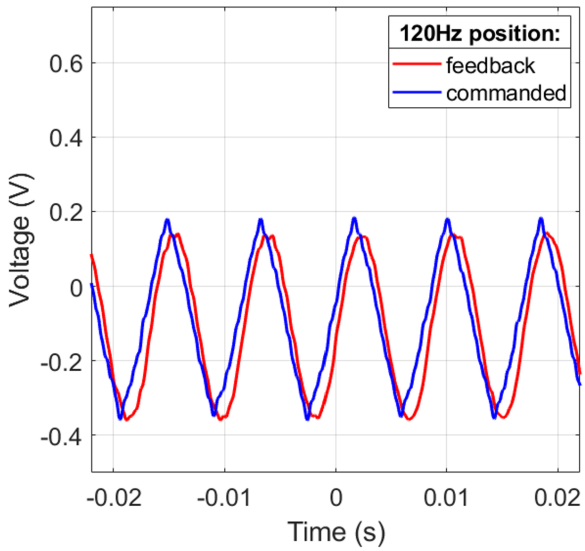

Figure 3.19: Commanded and actual position wavefront executed by the voice coil actuator at 120 Hz.

Interestingly, the response did not change significantly for voltage amplitudes in the range from 50 to 200 mV. At up to 130 Hz, the feedback response was approximately constant and attenuated by a factor of 0.8. At higher frequencies this factor increased up until 200 Hz, followed by a sharp decline. By tuning the gain parameters (proportional, integral and velocity gain) associated with the voice coil actuator control scheme (proportional-integral-derivative control) [62], different frequency response profiles can be achieved. While they can be made more linear, they taper off at a much lower actuation frequency. The profile shown in Figure 3.20 of the circuit allows high frequency motion components to be executed. This includes the regions in the triangular wave where the direction of motion changes and general ability to translate mass at high frequency (>100 Hz) sinusoidal motion. Note that if the actuator gain parameters are chosen so that it is underdamped, ringing could increase the settling time of the device and interfere with controlled positioning; the oscillatory response would in turn cause additional blur in high speed remote refocused frames. While the Figure 3.20 shows the overall frequency response profile of the device, additional tests on settling time and motion purity could be conducted in aim to improve RF imaging. Qualitatively, no significant artifacts were observed in high-frequency triangular motion waveforms recorded. The interpolated voltage factor was calculated by averaging the curves acquired for different amplitudes (Figure 3.20a) and then interpolating the resulting profile. This factor was used to adjust the voltage-to-distance conversion if the stage of the device is actuated as opposed static translation.

Conversion of the frequency response curve to decibels can done as in equation

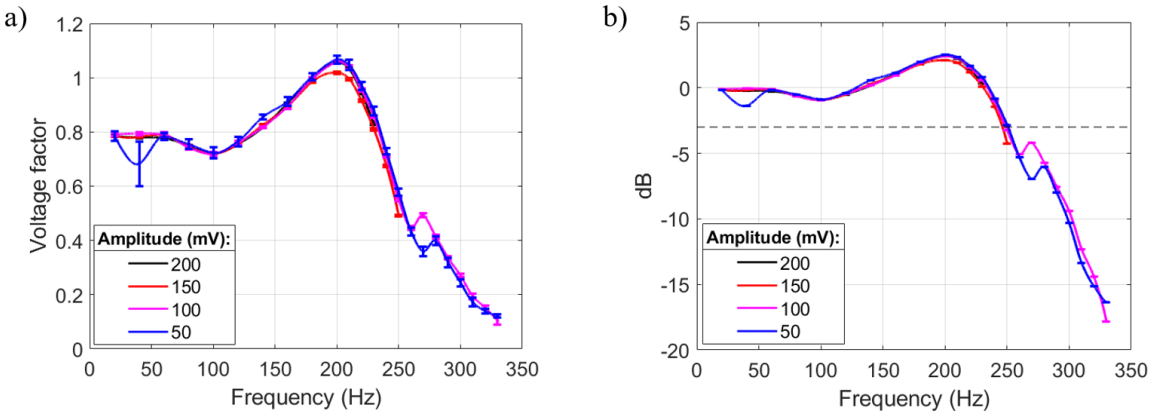

Figure 3.20: Response of the VC actuator to triangular driving wavefronts of differing frequencies and amplitudes with the mirror mounted. In a, the y-axis in a corresponds to the ratio of the measured feedback voltage to the commanded voltage. In b, the response curve is converted to dB. Dashed black line indicates the -3 dB point.

$$V_{dB} = 20\log_{10}\frac{V_2}{V_1}$$

where $\frac{V_2}{V_1}$ is the fractional change in voltage. From Figure 3.20b it can be seen that the -3 dB point where the amplitude decreases from baseline is at around 250 Hz. For voltage signals, this corresponds to about 70.7% of the peak value and marks the cut-off frequency. Above this frequency, the voice coil actuator experiences reduced efficiency and response amplitude.

3.7.3 Synchronisation with the 2PM

In bi-directional scanning driven by a triangular waveform, the acquisition of every second line becomes shifted relative to the one before it depending on the scan parameters. This image distortion effect is due to incorrect synchronization. Imposing a delay in the start of the movement between the scanning elements (start delay setting in SciScan 1.2 interface in LabView used to control the microscope) can correct for this shift. Otherwise, as explained explained in Figure 3.21, a sheared image is formed, or, if the delay mismatch is large enough, the features appear doubled. The slow galvanometric mirror (Y) is driven by a slow voltage ramp as shown in the solid black trace to sweep through y coordinates and form the frame. In that time, the fast mirror executes multiple triangular waveforms, forming the adjacent lines (blue and red). If the start times of both mirrors match up, the lines in the frame are filled in an orderly fashion (Figure 3.21a). In Figure 3.21b, the fast scanning element experiences an unaccounted for phase lag with respect to the slow element. This results in shearing of the lines: some pixels that should belong to blue lines are recorded in the adjacent red lines. In

the Scientifica 2PM, with the pixel dwell time of 0.08 ms, the start delay between the fast (X) and slow (Y) galvos that forms the image correctly is 453 tick periods of the DAQ card clock.

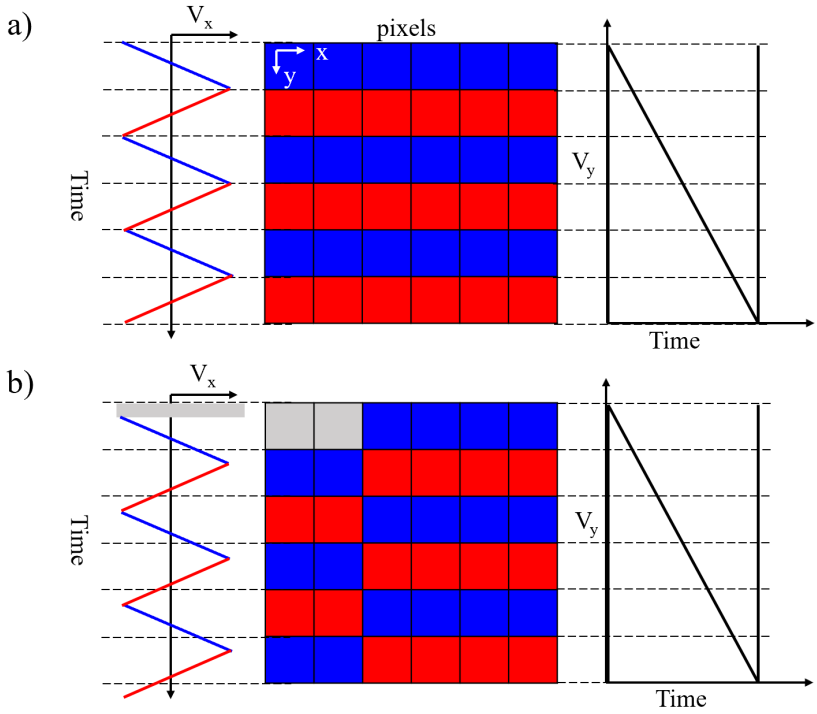

Figure 3.21: The impact of mismatched delay between the scanning components (galvo-galvo or galvo-voice coil actuator). In a, both components start scanning at the same time. In), the movement of the fast line-scanning component is delayed with respect to the slow component. This results in lines in the image appearing sheared or duplication of features with more significant mismatch.

To actuate the voice coil, the waveform used to drive the fast X galvanometric mirror is re-scaled in amplitude and re-routed with appropriate wiring. Rescaling option was implemented in the modified SciScan 1.2 interface in LabView. The microscope's scan mirrors are lighter than the mirror mounted on the voice coil stage. Furthermore, rotational motion associated with the galvo mirrors is easier to execute than linear translation. With different driving frequency and driving waveform amplitude settings, the optimal start delay value for the synchronised RF imaging will change more significantly than that for the galvo scan mirrors. Nevertheless, while look-up tables are commonly used for scan timing corrections, this approach was considered unnecessary, as manual fine-tuning of scan timing proved sufficient and could be adhered to with adequate precision in 2D live imaging mode in SciScan 1.2. It should be noted that the delay setting required to match the movement of the VC actuator and the slow galvo was significantly larger than that required to align the motion of the fast and the slow galvos together. SciScan interface was therefore modified to allow larger values of start delay.

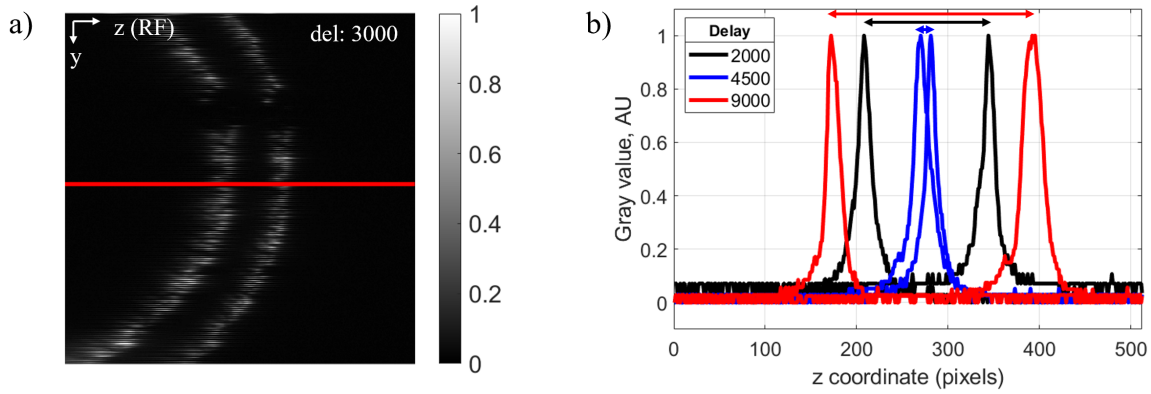

Figure 3.22: Determining separation of different features depending on start delay setting in a surface-stained bead sample. In a), adjacent lines are sheared. If normalised intensity profiled at the centre of the FOV (red line) are compared, in b) it can be seen that the adjacent line feature separation changes with delay.

The delay required for a representative Z-Y FOV (250×350 µm, 512×512 pixels, 122 Hz refocusing) was investigated by considering the separation of features in adjacent lines of an arbitrary sample (in Figure 3.22, large surface-labelled beads were used). With different delay setting, the distance between the features changed and this separation was identified in MATLAB for two lines central to the field of view (sample red line in Figure 3.22). Findpeaks() function was used to identify the precise position of corresponding features in the normalised intensity profile. In Figure 3.22b, it can be seen that at 2000 tick period delay, the features are mismatched. At around delay of 4500 tick periods, the spacing between them becomes very small and then at 9000 there is a cross over and the separation is large again. These separations plotted against the delay values for different VC scan settings are shown in Figure 3.23. It can be seen in 3.23a that with different voltage amplitudes similar to those used for RF-enhanced imaging, the delay value for zero separation between features in adjacent lines does not change significantly and is at approximately 4645 tick periods for 122 Hz. However, changes in scanning frequency impact the delay value (Figure 3.23b). While it is the same for 66 Hz and 122 Hz scanning, at 244 Hz the value almost doubles, from 4645 to 7484 tick periods. It should be noted that the optimal delay value differs over the field of view. This means that at nominal start delay setting for the features to align along the red line in Figure 3.22a, shearing can still be seen towards the edges. However, as the system is primarily geared towards AP line scanning (done in the centre of the FOV), finding an optimal delay value in the middle of the FOV is sufficient.

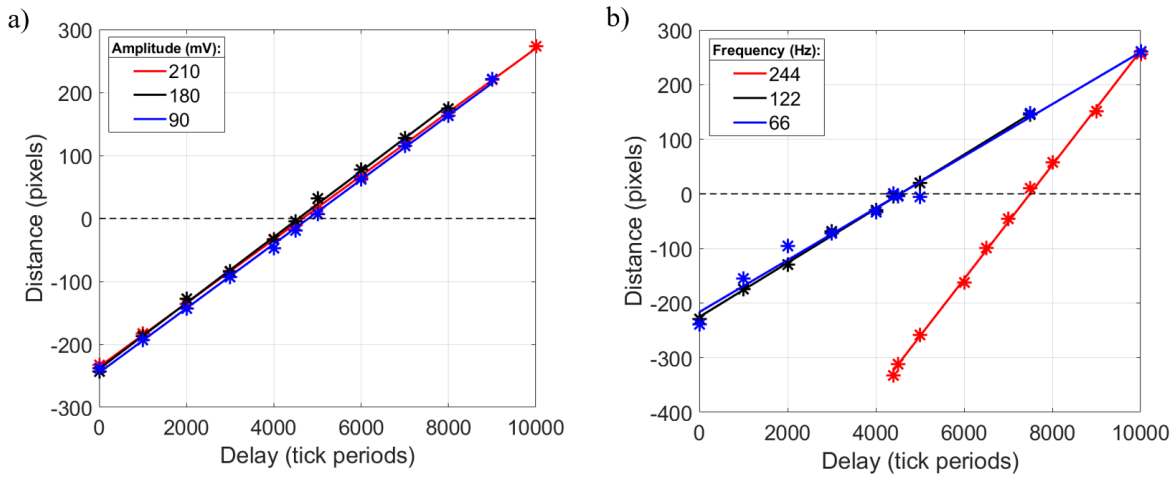

Figure 3.23: Impact of different amplitude (a) and frequency (b) of the VC scan on start delay value required to produce the image correctly.

3.8 Summary

To summarise, a custom built RF module compatible with retrofitting to a commercial Scientifica 2P microscope was designed (Section 3.1), built (Section 3.2) and characterised in terms of its optical throughput (Section 3.5), resolution (Section 3.4), pulse duration (Section 3.6) and frequency response (Section 3.7.2). We achieve axial refocusing at frequencies up to 250 Hz. Below 5 µm axial resolution is maintained over the range of 100 µm refocus. Optical distortions are acceptable (under 7 µm) axially and laterally over the refocusing range of approximately ±50 µm at the centre of the FOV. Although larger at the limits of the remote refocusing range (30 µm laterally and 15 µm axially), the distortions are acceptable compared to the size of cardiac cells. Better system alignment as well as a precision calibration sample [36] would allow increasing the imaging precision. The laser pulse broadened by RF optics is compressed from 487 fs to 156 fs using a single prism pulse compressor and the increase in fluorescence signal is verified experimentally with a Fluorescein-based sample. The 2P-RF system is optimised for fast AP imaging across both longitudinal and transmural directions in an acute cardiac preparation, for example, the acute rabbit ventricular slices.

Chapter 4

Acute rabbit ventricular slices

To utilise the 2P-RF system described in Chapter 3, an appropriate sample choice is pivotal. The following chapter introduces acute ventricular slices as a model to study transmural action potential propagation and places it in the context of other cardiac preparations (Section 4.1). Viable rabbit ventricular slice preparation protocol is detailed in Section 4.2 from excision and voltage sensitive dye loading to slicing, mounting and electrical stimulation. Importantly, assessment of sample viability is discussed in Section 4.3.

The contributions to the work detailed in this chapter are as follows. The rabbit was sacrificed by a licensed technician (Mr. John McAbney). Dr Erin Boland performed the Langendorff perfusion and Fluovolt dye loading. This is described in Section 4.2.1. Steven M. Moreno made Tyrode's solutions (Section 4.2.2) and helped with the design of the custom sample chamber for electrophysiology experiments, shown in Figure 4.6. My personal contribution involves dissection, slicing and mounting the acute slices as well as testing their viability (Sections 4.2.3-4.2.5 and 4.3). CellOptiq measurements were made by me with advice of Dr Eline Huethorst and Sasha Forbes.

4.1 Review of cardiac models

The choice of *in vitro* cardiac model determines the experimental conditions required to sustain functional viability. In addition to complexity of preparation, the cost, the number of animals sacrificed, importantly, the model's similarity to real *in vivo* conditions and human myocardial properties is considered. The ideal sample should maintain its electrophysiological properties and be structurally intact to embody the effects of multicellularity in *in vivo* hearts [63]. The model should also have the capacity to mimic both healthy and diseased conditions. A comparison of widely used cardiac models is shown in Figure 4.1.

Isolated cardiomyocytes obtained through enzymatic disassociation give insight into

Features:	Isolated cardiomyocytes 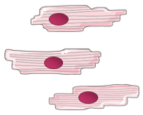	Engineered cardiac tissue 	Intact heart 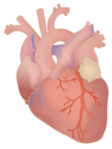	Viable cardiac slices 
Similarity to *in-vivo* structure and function	poor	medium	excellent	good
Cost	low	medium	high	low
Number of animals sacrificed	low	low	high	low
Capacity for culturing	poor	excellent	poor	good
Preparation difficulty	low	medium	high	low
Throughput	high	medium	low	high

Figure 4.1: Review of advantages and disadvantages of available cardiac models. *Adapted from:* [63].

cellular and subcellular electrophysiology. The preparation has a low cost and yields a significant number of samples from a single animal enabling high throughput experiments [64]. Moreover, these experiments can be highly controlled and automated in terms of experimental conditions such as biochemical environment or mechanical load on the cells. Nevertheless, the transferability of results to *in vivo* hearts is compromised, as isolated cells are no longer in their native, intact environment. This is because single cell contractility and electrophysiology is independent from the effects of multicellular structures and their variation, or the connection to extracellular matrix and intercallated disks. Generally, structural remodelling occurs within hours post isolation and the choice of isolation method can also impact the function of CMs [10, 63, 64].

Another option is engineered heart tissue which has gained popularity in recent years, especially in the field of regenerative medicine [65]. Human pluripotent stem cell-derived cardiomyocytes (hiPSCs) are predominantly used in these studies. The aim is to create artificial tissue with microstructures that mimic as closely as possible the three dimensional architecture and function of healthy *in situ* cardiac muscle. This potentially allows replacing electrically inert post-MI scar with conductive engineered cells to restore normal electrophysiology in treated hearts. Furthermore, hiPSCs are not subject to the same ethical implications as using research animals. Nevertheless, despite the progress made in the field, the calcium dynamics, structure, metabolism and electrical function of engineered cells are still considered immature when compared to adult cardiomyocytes [63]. Finally, sterility is critical for the engineered tissue especially during the cell culturing step.

On the other hand, whole intact hearts can be used as a model where the tissue is mature and intact on a micro- and macroscopic level [3, 57, 58]. Mouse, rabbit or rat models are often used, with high translatability of results to human heart physiology and pathology. For this project, the rabbit model was chosen, as its electrophysiology is much more similar to that of human hearts compared to rodent hearts. Intact hearts are Langendorff-perfused through the cannulated aorta in retrograde fashion with oxygenated perfusate containing salts and glucose to meet their metabolic needs. Therefore, physiologically relevant heart function can be maintained for several hours on the perfusion rig. For imaging purposes electromechanical uncouplers such as Blebbistatin or BDM (2,3-Butanedione monoxime) can be used to immobilise the organ while preserving electrical signal propagation. Nevertheless, intact heart experiments are costly and require many more animals to be sacrificed. Furthermore, maintaining viability requires significant technical expertise, and complex experimental design (e.g. advanced temperature and pressure control or robust prevention of air bubbles which can embolise blood vessels) [63].

Acute myocardial slices are thin (300-400 µm), precision-cut cardiac sections that encompass the advantages of both the intact heart and isolated cardiomyocyte models - considerable experimental throughput and reduced complexity are preserved, while most of the CMs are within their intact environment, connected via the extracellular matrix (ECM) and functioning in tandem with their neighbouring cells [10, 63, 64]. When prepared correctly, tissue damage is limited to the top and bottom surface of the slice (approximately 3% of cells [63]). Many slices can be made from a single organ, reducing the cost, and they do not require complex Langendorff perfusion system or a rigorous experimental set up to maintain viability. Moreover, as 200 µm is the upper limit for oxygen diffusion, unlike thicker tissue specimens, the slices do not need coronary perfusion to prevent hypoxia. Importantly, the sample dimensions is compatible with our 2P-RF system and covers the range of our remote focusing scan. Therefore, acute rabbit ventricular slices were chosen as an intermediate complexity model to validate 2P-remote focusing to track action potential propagation transmurally.

4.1.1 Voltage sensitive dyes

The most accurate method to directly measure action potentials or CM membrane voltage is with sharp microelectrodes [58]. Nevertheless, this is invasive, requires tissue perforation and is not suited for probing large scale, multicellular preparations. Optical methods are therefore widely employed to investigate cardiac electrophysiology of large scale, intact tissue. Voltage sensitive fluorescent dyes (VSDs) enable such measurement as their fluorescence intensity or spectral properties change with transmembrane potential. Two main classes of VSDs are electrochromic [66] and photo-induced electron

transfer (PET) based VSDs [67].

In electrochromic (ratiometric) dyes, the potential difference affects the wavelength of light emitted; the energy levels shift within the fluorophore due to the Stark effect. This is a very fast process and electrochromic dyes have sufficient temporal resolution to probe the rapid upstroke of the action potentials of cardiac cells. Furthermore, electrochromic shift allows high SNR AP detection, as the long and short wavelength parts of the emission curve are acquired with two PMTs [3, 57]. Taking the ratio of the signal on the two PMTs cancels out motion artifacts and mitigates the effect of non-uniform staining and photobleaching. An example of an electrochromic dye is Di-4-ANEPPS, which binds to the plasma membrane of the cell. A 100 mV potential difference reportedly yields a 10% change in fluorescence intensity ($\Delta F/F$) with femtosecond temporal resolution [66, 67]. Nevertheless, ratiometric dyes introduce a depth dependent bias as the two colour bands are scattered and absorbed differently in tissue. Theoretically, recalibration at different depths would be needed for precision measurements [68].

PET based VSDs rely on electron rich donors connected to a fluorescent reporter through a molecular wire spanning the cell membrane, as shown in Figure 4.2. Electric field variation across the membrane leads to change in the rate at which electrons are transferred along the wire and thus change in fluorescence intensity. When the direction of the electric field is aligned with the direction of electron transfer, the PET process is diminished and fluorescence is enhanced. Opposite is true for electric field antiparallel to the electron transfer direction [67]. Fluovolt belongs to this class of VSDs, reportedly yielding very high sensitivity ($\Delta F/F$ of 25% per 100 mV) and sub-millisecond response to change in electric field [67]. However, these specifications are sample dependent: in cardiomyocyte monolayers the reported $\Delta F/F$ was 12-20% while in neuronal cell cultures fractional change was lowered to 7%. In intact Langendorff-perfused mouse heart Fluovolt's response was around 10% [58].

Fluovolt was the dye of choice in our study. In [58], Di-ANEPPS-4 and Fluovolt were compared in terms of toxicity to the cardiac preparation, SNR and dynamic range. While Fluovolt's SNR was lower, it yielded fewer occurrences of transient and permanent atrioventricular blocks and ventricular tachycardia during dye loading [58]. Furthermore, Fluovolt staining facilitated imaging of deeper tissue layers due to the increase in $\Delta F/F$. The power at sample required was significantly lower with Fluovolt; for example, layers 300 µm below the epicardium were imaged with 20 and 75 mW average power with Fluovolt and Di-ANEPPS-4, respectively. This renders Fluovolt particularly suitable for our study due to RF power limitations discussed in Section 3.5. Finally, the peak excitation wavelength of Fluovolt (800 nm as reported in [58]) is suitable for our system whereas the available power output of our laser at the longer excitation wavelength required for Di-ANEPPS-4 is significantly lower [58].

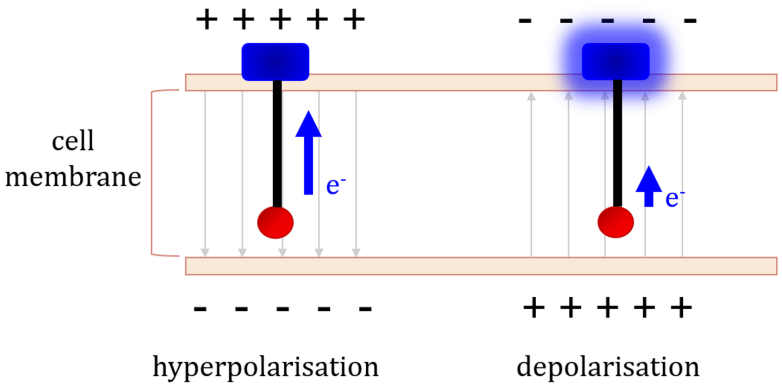

Figure 4.2: Schematic of the working principle of PET-based VSDs. A fluorescent reporter (blue) is connected to an electron source (red) through a mollecular wire. Change in membrane voltage affects the electron transfer through the wire and hence the intensity of emitted fluorescence. *Adapted from*: [67].

4.2 Preparation of acute cardiac slices

Myocardial slice preparation for our experiment follows closely the protocol outlined in Watson et al. (2017) [10]. The modifications made to better suit our experimental requirements are discussed and justified.

4.2.1 Fluovolt dye loading via Langendorff perfusion

Ethics statement

Animal handling and sacrifice was done at the University of Glasgow, School of Medical and Veterinary Sciences by licensed technicians. The protocol is in accordance with the UK Animals (Scientific Procedures) Act 1986. In all experiments male or female White New Zealand rabbits were used.

An injection of 1000 IU heparin was administered via the right marginal ear vein to prevent blood clotting together with 200 mg/kg sodium pentobarbitone for terminal anesthesia. The beating heart was rapidly excised and placed in ice cold heparinised Tyrode's solution to stop contraction and cannulated through the aorta onto a Langendorff perfusion rig. Tyrode's solution at 37°C was bubbled with a mixture of medical grade carbogen (95% O_2%, 5% CO_2) for tissue oxygenation and to maintain a 7.4 pH. A constant flow rate of 40 mL/min was selected, which corresponds to coronary perfusion pressure fluctuating between 60 and 80 mmHg. Fluovolt (15-17 µL in 500 ml of Tyrode's solution) was injected into the perfusate together with 150-170 µL pluronic acid to enhance binding and retention of the dye.

It should be noted that in order to mitigate the number of animals sacrificed, the

Reagent	Solution	Final concentration (mM)	1L
NaCl	Both	140	8.182 g
KCl	Slicing	9	0.671 g
	Recording	4.5	0.335 g
Glucose	Both	10.32	1.860 g
BDM	Both	30	3 g
HEPES	Both	10	20 mL of 500 mM stock solution
$MgCl_2$	Both	1	1 mL of 1M stock solution
$CaCl_2$	Slicing	1	1 mL of 1M solution
	Recording	1.8	1.8 mL of 1M solution

Table 4.1: Reagents required for Tyrode's solution preparation for slicing and recording [10].

heart underwent electrophysiological investigations for approximately 3 hours before the slicing procedure, requiring Blebbistatin to prevent motion artefacts during optical recordings. Cardiac viability after the protocol was confirmed via ECG recordings and visual verification of return of contraction after Blebbistatin was washed out for 20 minutes. The retention and contrast of Fluovolt is somewhat reduced with this additional time and exposure to light.

4.2.2 Tyrode's solutions

Tyrode's perfusate contains salts and glucose to maintain sample function and viability. In our experiment, two variations of Tyrode's solution are used - one for slicing and transportation and another for electrical stimulation and imaging [10], as shown in Figure 4.1. The differences in slicing and recording solutions are to protect the tissue during the cutting process and to encourage electrical activity when imaging. The slicing solution inhibits metabolism and electrical activity due to low temperature (around 4°C), increased potassium (9 mM) and decreased calcium concentrations (1 mM). Importantly, 30 mM BDM further immobilizes the tissue preventing mechanical damage if the tissue was to contract during slicing; the concentration was chosen as in [10]. In the recording solution, conversely, the 1.8 mM calcium concentration encourages sample electrical conduction in the recording solution which is kept at room temperature and used during imaging or visual inspection of contraction (in the absence of BDM). This is necessary for mechanical contraction to take place as 1.8 mM is the physiological extracellular calcium concentration.

In both solutions, HEPES (10 mM), $MgCl_2$ (1 mM) and $CaCl_2$ stock solutions are added, and the salts (NaCl, KCl), glucose (10.32 mM) and BDM (30 mM) are dissolved with a magnetic stirrer to achieve the stated final concentrations. The solutions are then filtered with a Millipore filter (pore diameter of 0.025 µm) and bubbled for 5

minutes with carbogen (95% O_2%, 5% CO_2) to oxygenate the solution prior to the experiment. This step is not required for pH maintenance due to the choice of HEPES buffer. Some Tyrode's recipes require sodium bicarbonate instead, however HEPES ensures preparation viability by preventing the pH drift more reliably, especially as the Tyrode's solution is exposed to atmospheric oxygen during the slicing procedure. Slicing solution is kept on ice after bubbling.

4.2.3 Rabbit cardiac tissue preparation for slicing

Key steps in the slicing protocol are shown in Figure 4.3. The intact heart is removed from the Langendorff perfusion system (Figure 4.3a). It is submerged in icy slicing Tyrode's solution. Firstly, to prepare the ventricular section, the aorta and the atria are cut off with surgical scissors as in Figure 4.3a, dashed red line. The opening of the left and the right ventricles becomes visible with the inner wall of the heart (the septum) between the two (Figure 4.3b). Cutting through the valves and along the edge of the septum allows removal of the LV (dashed red lines). If the excised LV tissue does not lay flat, the edges of the ventricular block should be trimmed. In Figure 4.3c) a flat left ventricular block is shown. The structure of the endocardium as well as the papillary muscles can be seen. Rabbit LV sections are big enough to make several blocks depending on the desired size of the slice. This procedure should be performed as fast as possible and the tissue should be periodically re-submerged to icy Tyrode's solution. Slices close to the epicardium surface have compact cardiac fiber arrangement and are prioritised for imaging. Therefore to save time, the first cut is generally made halfway through the ventricular block thickness.

4.2.4 Vibratome slicing of fresh cardiac tissue

Slicing is performed on a vibratome (Leica VT1200S) using ceramic blades (Campden Instruments, 7550-1-C). To mount the sample, an agarose sheet is prepared by pouring molten 4% agar in a large petri dish. Agar sheet is glued on the vibratome sample mount using a cyanoacrylate-based glue (Loctite). The vibratome blade is advanced through the top layer of the agar to cut off surface imperfections. The ventricular block is dried and glued onto the sheet epicardium down, ensuring the corners are firmly attached. A thick agar block at one of the edges of the tissue can be used to stop it from deforming as the blade cuts through. The sample is resubmerged in the icy slicing solution as soon as possible. The vibratome blade is advanced at 0.03 mm/s, the blade vibration amplitude is 2 mm at 80 Hz frequency. Slice thickness is 300-400 µm. Precise temperature control of the immersion solution is important as it regulates tissue metabolic needs. To this end, the ice in the vibratome bath is replaced regularly and the

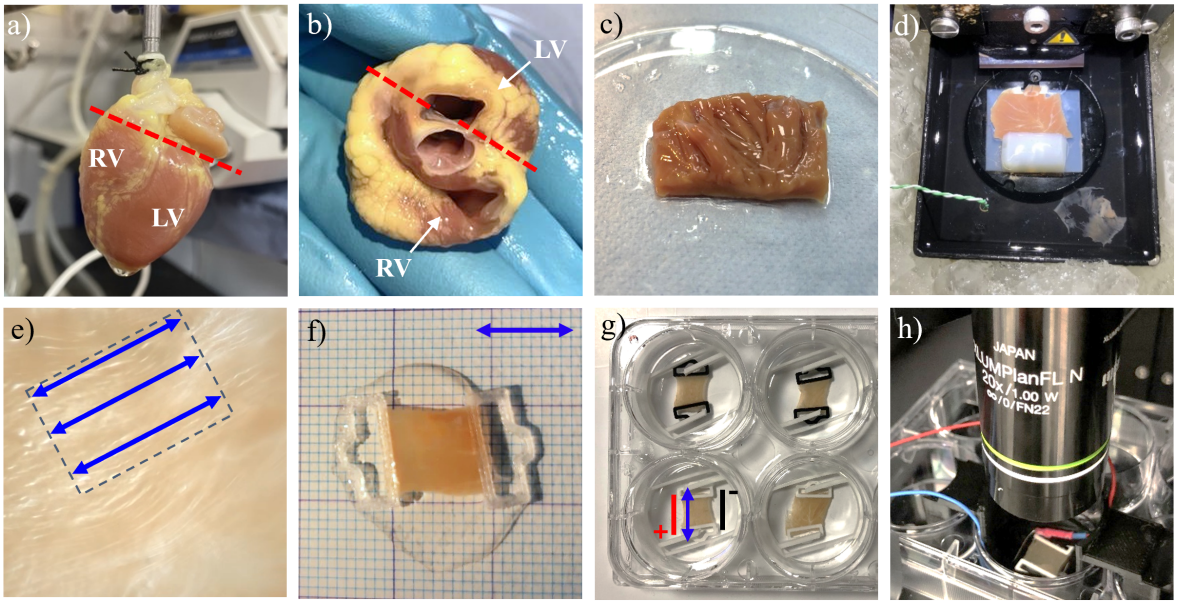

Figure 4.3: Acute cardiac slice preparation protocol. In a), the rabbit heart is secured on Langendorff perfusion rig with right and left ventricles indicated (RV and LV, respectively). The atria, aorta and the veins are cut off (red dashed line) as the heart is removed from the rig. This renders the ventricular openings and valves visible as in b). The wall of the RV is noticeably thinner than that of the LV; red dashed line indicates where a cut is made to separate the left ventricle. c): A flat LV section with the endocardium (innermost layer of the ventricle wall) facing up. This LV block is glued epicardium (outermost part of the ventricle wall) down on a sheet of agar attached to the vibratome stage shown in d). The bath is cooled with ice and a thermocouple (green wire, bottom left) is used to monitor the temperature of the Tyrode's solution. Under a dissection microscope the area where the fibre orientation is monodirectional (blue lines) within the slice is selected (black dashed line) e). f): A representative slice with 3D-printed hooks glued for convenient mounting. Blue arrow indicates the long axis of the fibre orientation. A standard 6-well plate is used to store the slices, which are fastened with a 3D-printed mount (white). Electrodes are also held across the slice in the groove of the mounts, parallel to the long axis of the cardiac fibres, as indicated in the illustration (red and black denote opposite polarities). In h), a slice is positioned under the 2P-RF microscope; 6-well plate and the mount accommodate the objective barrel and the electrodes (note that in h) a different version of the mount is shown compared to g).

temperature of the slicing solution is maintained ideally around 4°C, although below 10°C is acceptable (Figure 4.3d). While there is tolerance to temperature variations, freezing temperatures can result in small ice crystals within the tissue thus leading to damage as well as hypothermia. Regular temperature checks are therefore performed. We don't oxygenate the solution as the metabolic needs are considered negligible due to low temperature. It should be noted that one slice may take 10-15 minutes to obtain, depending on the size [10]. Detached slices are transferred to a standard 6-well plate with icy slicing solution for storage.

4.2.5 Slice preparation for mounting

In the LV close to the epicardium, cardiac fibers will rotate in the same plane (Figure 4.3e). Under a dissection microscope the region of unidirectional fibre alignment is identified (blue lines). A rectangular section is then trimmed with a razor blade (approximately 10 × 10 mm) to isolate the aligned region (black dashed line). It is significantly easier to inspect the slices with illumination from below, although the sample exposure to the heat of the lamp should be minimised. In rabbit cardiac tissue, the fibre orientation is also visible by eye.

3D printed plastic hooks are glued to the edges of the slices (Figure 4.3f). Tissue exposure to the glue kills the cells and this step requires precision. At all times direct manipulation of the tissue is avoided and the slices are positioned using water surface tension or a paint brush.

4.3 Slice viability assessment

Considerations for consistently producing viable slices are outlined in the following section together with methods to assess the quality of the preparations. Viability was assessed by live/dead cell staining and ensuring that slices contract with a consistent force when electrically stimulated (slice contractility estimation).

4.3.1 Maintaining slice viability

Firstly, the precision of the vibratome cut is important to maintain slice viability, as shown in Figure 4.4. Mounting the ventricular block epicardium down ensures that the planes of cardiac cell layers are aligned with the advancing blade consequently preventing tissue damage. If the axis of the cut is not along these planes, too many cells can be damaged, leading to non-functional preparations (Figure 4.4c). Additionally, while we did not recalibrate for z-axis deflection angle as suggested in [10] as the Vibrocheck device was not available, the vibratome is regularly serviced. Furthermore,

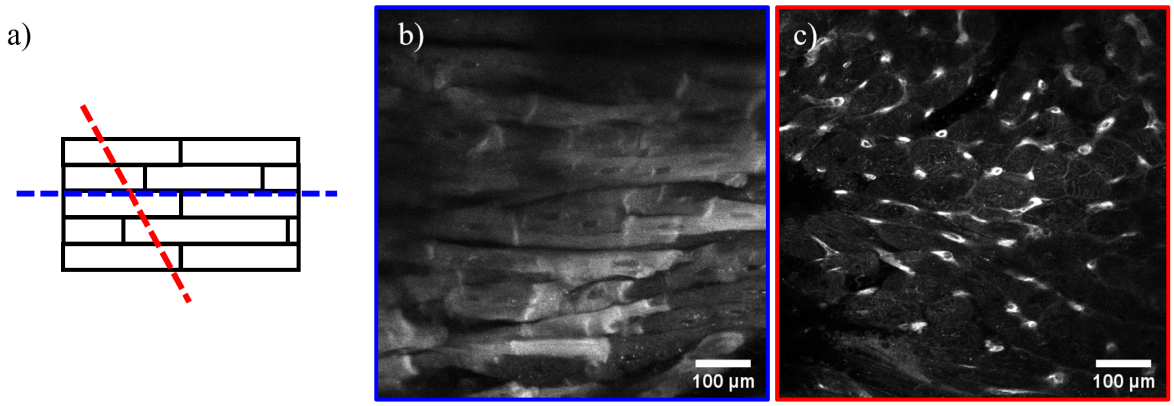

Figure 4.4: Examples of cardiac slice structure close to the plane of the cut (a). In b), 2P autofluorescence image shows periodic layout of intact cardiomyocytes, as the cut was along the plane of the cardiac cell layer (blue dashed line in a). In c), a Fluovolt-stained preparation is shown - the cut was diagonal to the cell axis (red dashed line in a). Here, the small bright structures are capillaries.

trimming the agarose sheet with respect to the blade ensures the sample is mounted in the correct plane.

Secondly, stainless steel blades are significantly less sharp than ceramic counterparts, often yielding a faulty cut. The resulting mechanical agitation and drag of the tissue could also cause disturbance in the alignment of layers and most slices cut with stainless steel blades were unviable. Therefore we discontinued the use of steel blades in favour of ceramic blades.

It should be noted that some studies suggest embedding the fresh tissue in agar, making it easier for the blade to advance through [69]. Nevertheless, temperature of the agar and complete isolation from salt-rich Tyrode's solution may damage these preparations. Importantly, when mounting the tissue block endocardium down [70], it is difficult to ensure the fibers are aligned with the blade, thus compromising the viability and reproducibility of slices [10, 64].

Finally, no additional oxygenation is taking place at any stage of the experiment; even as the gas escapes the pre-oxygenated Tyrode's solution, at room temperature the atmospheric oxygen level is sufficient to maintain the viability of slices.

4.3.2 TTC staining

Tetrazolium chloride (TTC) staining is an inexpensive method used to identify regions of metabolically active (viable) versus metabolically inactive (unviable) tissue, as it turns mitochondria of living cells deep red. For example, TTC staining is a widely applied method used to ascertain the locations of post-MI fibrotic patches. 1% TTC in Tyrode's solution was used to assess the viability of slices produced from different

locations in the ventricular section (Figure 4.5a). Control slice was submerged in pure isopropanol for 10 minutes, rendering the tissue dead. Both the viable (N = 7) and the control slices were submerged in the 37°C TTC-Tyrode's at the same time and incubated for 20 minutes for uniform colour development. As shown in Figure 4.5b and c, viable slices turned deep red while the control slice remained unstained. Importantly, the deep red stain across slices 1 - 6 evidence the absence of a hypoxic core in the middle of the ventricular section, although in slice 5, the cut was imperfect and damaged tissue structures are visible in the middle of the slice. The slice edge colour is faded, as around the cut of the ventricular section the cells are damaged and any aligned fiber sections should be chosen from the central regions of the slice.

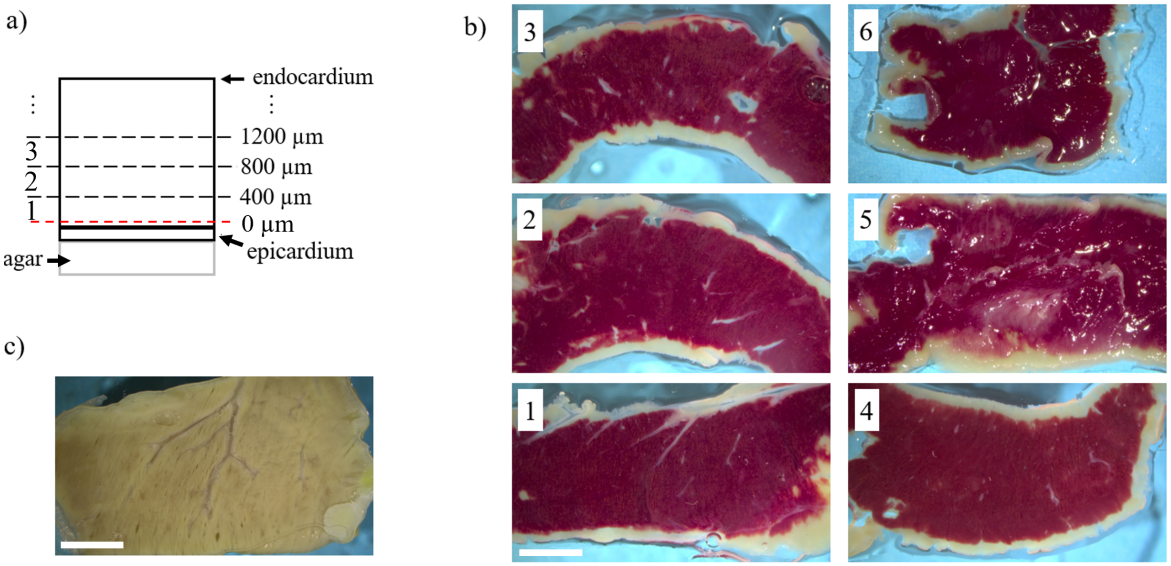

Figure 4.5: TTC staining of cardiac slices throughout the tissue block. a): Position of each slice with respect to the epicardium. b): Images of TTC stained viable slices corresponding to positions in a). The red dashed line denotes the last cut before the epicardium, the distance between which is less than 400 µm. In c), a control slice submerged in isopropanol for 10 min prior to TTC stain is shown; as the tissue was dead, the slice did not stain. All pictures were obtained with Axiocam 208 Colour camera on a Zeiss Stemi 508 dissection microscope with uniform illumination using the same exposure and white balance settings. The reflections on slices 5 and 6 are because the slice was laid on a petri dish. Images of slices 4-1 were taken with the petri dish flipped over. Scale bars denote 0.5 cm.

4.3.3 Electrical stimulation of acute cardiac slices

The following section describes the electrical stimulation of acute slices used throughout the study. To begin with, it is used to verify slice viability in every slicing session by visual confirmation of contraction under a dissection microscope. Furthermore, triggered voltage signals at an appropriate frequency were utilised during contractility

studies (Section 4.8) and optical mapping (Section 4.3.5) with the CellOPTIQ system, as well as during 2P-RF imaging (Chapter 6). In all the outlined cases, the slices are paced with a Digitimer MK-2DSA voltage stimulator and Grass platinum electrodes placed parallel to the long fibre orientation (Figures 4.3g-h and 4.6). The slices and the electrodes are secured with a custom 3D printed mount in a standard 6-well plate.

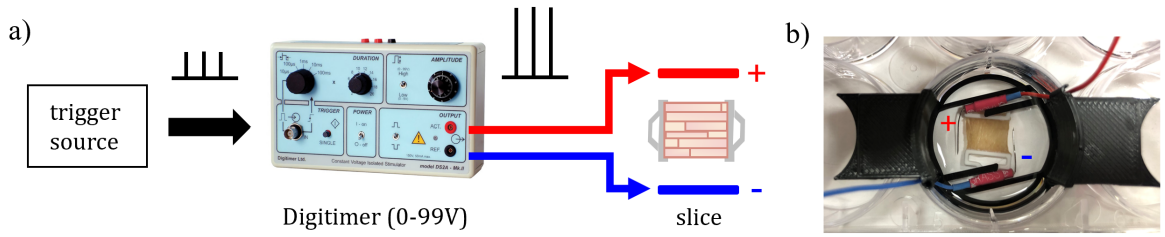

Figure 4.6: Electrical stimulation of acute slices. a) Signals from the trigger source (for example, the DAQ board in the case of 2P-RF microscope) trigger the stimulator which imparts a voltage difference between two platinum electrodes positioned across the slice. A representative photo of the system is shown in b).

During the stimulation, the slices are submerged in Tyrode's recording solution (Section 4.2.2) at room temperature and generally most slices are paced with a pulse duration of 12 ms with an aplitude of approximately 40-50 V. The voltage amplitude setting is highly experiment dependent, and in some slicing sessions the preparations contracted at lower potential differences (20 V). This also depends on the distance between the electrodes and how close they are to the tissue, which differs slightly for each slice mounted. In general, the slice should be stimulated at an increasingly higher voltage, until the contraction becomes apparent. After that, the voltage setting should only be raised by a couple of volts. If the optimal amplitude is exceeded significantly (the range of 80-90 V), the slice will stop contracting when paced. While a longer pulse duration differs from the physiological 3 ms pacing for rabbit models, at room temperature it helped the slices to respond to lower voltage amplitudes and was therefore chosen. The reader should note that the elevated calcium concentration in the recording solution is critical for the muscle to respond to electrical stimulation. Furthermore, for initial viability checks under the dissection microscope as well as contractility studies, the recording solution does not contain BDM; a contraction is observed and the slice is placed in BDM-enriched recording Tyrode's for AP imaging only. At least 10 minutes are required for the slices to adapt to a change of solution.

4.3.4 Slice contractility assessment

As discussed in Section 2.2.1, cardiac muscle contracts when the intracellular calcium binds to the troponin-C protein, causing the sliding of the actin filament along the

myosin filament. The strength of this contraction is described by contractility; it considers the generated mechanical force and velocity of sarcomere shortening and subsequent relaxation. The key parameters defining this process are the interval or beating frequency, Up90 and Dn90 (muscle contraction and relaxation times, respectively), and Cd50 (contraction duration at 50% of contraction amplitude), as shown in Figure 4.7. Consistent measurements of the aforementioned quantities from different slices and hearts ensure reproducibility. Additionally, the variation of these quantities across separate slices and different ROIs within a particular slice allows contextualising sample quality and electro-mechanical behaviour consistency, or a lack of thereof. Therefore, a quantitative investigation of contractile properties is an important step in establishing a cardiac model. This is especially true as the hearts from which the slices are produced are first used in another experimental protocol on a Langendorff perfusion rig. The resulting natural denaturation of the organ's viability over time is expected to influence the contractile properties. Additionally, the hearts may have been subjected to slightly different protocols prior to slicing, contributing to the variability.

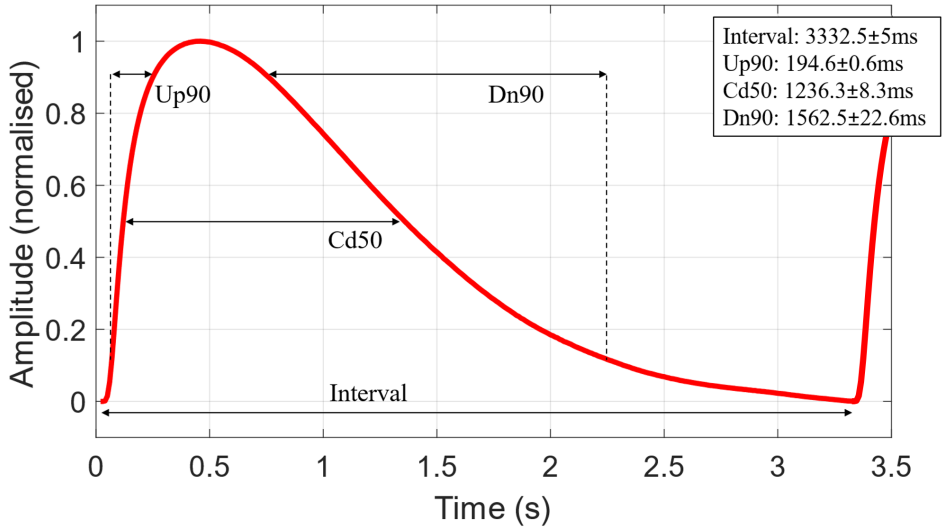

Figure 4.7: Average contraction profile from slice in Figure 4.8. Graphical explanation for key quantities describing contraction, namely the interval, Up90 (contraction time), Dn90 (relaxation time) and Cd50 (Contraction duration at 50% of the contraction amplitude) is provided, with the results for this particular slice shown in top right corner. Note that by convention, Up90 and Dn90 times are calculated from 10% to 90% of contraction amplitude. *Adapted from:* [71].

Importantly, the reader should note that the following analysis is of data acquired during two separate experiments (from two hearts). Ideally, slices from more hearts would be investigated, which was not possible due to a limited number of animals available. During the testing phase of the 2P-RF microscope and initial phase of establishing the cardiac slice model, in accordance with the University's mitigation strategy for animal research [11], only hearts that had already been used in other

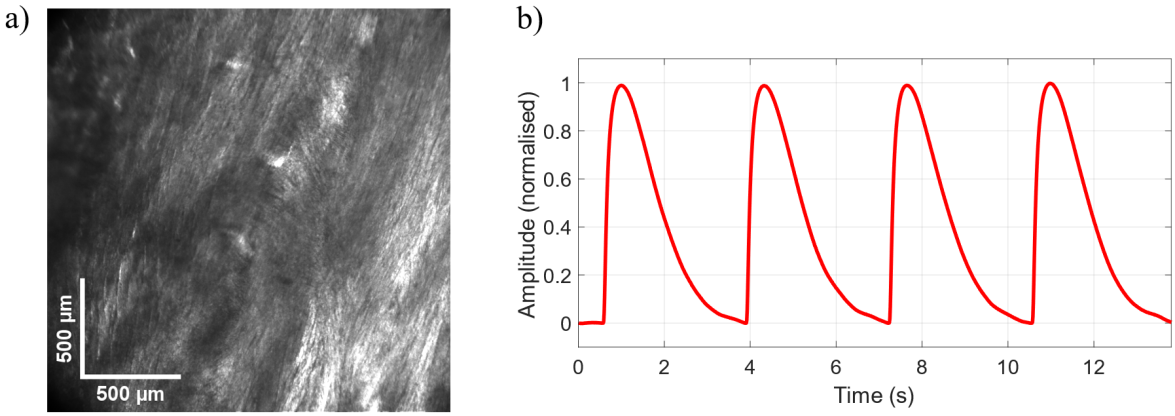

Figure 4.8: Slice contractility assessment. A sample FOV within the central region of the preparation (a). A recording of this region was acquired with the slice paced at 0.3 Hz. The resulting contractility trace is shown in b), where the y-axis denotes the normalised amplitude of motion (proportional to velocity of slice motion).

experiments were utilised for slicing. Nevertheless, the imaging and analysis protocol would be identical with a larger sample size. Furthermore, for the purpose of the 2P-RF experiment, this quality of assay is sufficient, as the crucial considerations such as whether the slice is uniformly viable at room temperature and what electrical stimulation should be applied for optimal function can be addressed.

In the following section all slices were submerged in room temperature Tyrode's recording solution with elevated calcium concentration (Section 4.2.2) and without electromechanical uncoupler (0 mM BDM). This enabled contraction under electrical stimulation, facilitated as described Section 4.3.3. An inverted epi-fluorescence microscope and a multiwell screening platform (CellOPTIQ, Clyde Biosciences Ltd) was used [72]. Spatio-temporal contractility analysis was performed with ContractilityTools software (Clyde Biosciences Ltd). A high frame rate CMOS camera (Hamamatsu ORCA-flash 4.0 V2, 6.5×6.5 µm pixel size) was used to acquire brightfield video recordings from the central region of electrically stimulated slices at 100 fps. A 4X air objective (Olympus UPlanFLN, NA 0.13) yielded a FOV of 2×2 mm (Figure 4.8a). In ContractilityTools, the video files were converted to .tiff stacks of 16 bit depth and the open-source MUSCLEMOTION algorithm was utilised [73]. In MUSCLEMOTION, the intensity of each frame of interest is compared to to a reference frame by computing the absolute difference in pixel values. This yields a new image where unchanged regions are rendered dark and contracting regions appear bright. The mean intensity of this difference image provides a single measure of movement for each frame. Therefore, a profile of contraction over time can be obtained by repeating this process over a time lapse. Note that with a fixed reference frame, MUSCLEMOTION measures total displacement, whereas when the reference frame depends on the frame of interest (for

example, with a rolling reference frame) contraction velocity profile can be acquired [73]. Using MUSCLEMOTION on a time lapse of an electrically stimulated cardiac slice yields a contractility trace as shown in Figure 4.8b. It can be seen that the shortening of the muscle fiber is rapid, whereas the subsequent lengthening or relaxation is slower. To obtain the average motion profile, the traces were time-averaged for each interval, where the beginning of each event was identified by the peaks in the time derivative of the trace. The mean interval, Up90, Dn90 and Cd50 were calculated. Note that change in illumination conditions (and therefore the pixel intensity) yields different magnitudes of contraction amplitude, without affecting the temporal parameters describing mechanical motion. Therefore, for the purpose of this experiment, all contractility traces are normalised. The average contraction profile for slice from Figure 4.8 is shown in Figure 4.7. For the representative slice, the mean interval, Up90, Cd50 and Dn90 were 3332±5 ms, 194±0.6 ms, 1236±8.3 ms and 1562.5±22.6 ms, respectively. As the uncertainties make up only a small percentage of the total value (e.g. 1.44% for Dn90), the estimation of the aforementioned quantities is robust. This is because MUSCLEMOTION algorithm is applied to the whole FOV of the representative slice (shown in Figure 4.8), 4 contraction traces were averaged and their shape was consistent throughout the time lapse.

To determine how the mean interval, Up90, Cd50 and Dn90 vary between slices obtained from the same heart as well as the variability of the aforementioned properties between different slicing sessions, data from two hearts were analysed (N_1=5 and N_2=4 slices), as shown in Figure 4.9a-d). Note that in the first experiment, 4 out of 6 slices were were viable, 2 showed no contraction. In the second experiment, 1 out of 6 imaged slices showed almost no contraction and ContractilityTools analysis failed. Overall, neither of the samples displayed spontaneous contraction. Under stimulation of 0.3 Hz, the mean intervals were I_1=3328±6 ms and I_2=3327±10 ms, reflecting the pacing frequency. The difference in measured interval between the two experiments and the uncertainty of results is negligible (for example, the standard deviation (σ_1) constituted 0.3% of the mean). This indicates consistent response to stimuli with negligible variation. The mean contraction time $Up90_1$ was 159±35 ms (σ_1: 22.01% of the mean), $Cd50_1$ was 803±170 ms (σ_1: 21.17% of the mean) and the relaxation time $Dn90_1$ was 1165±168 ms (σ_1: 6.93% of the mean). All of these quantities were longer in the second experiment: the mean contraction time $Up90_2$ was 220±81 ms (σ_2: 36.82% of the mean), $Cd50_2$ was 971±286 ms (σ_2: 29.45% of the mean) and the relaxation time $Dn90_2$ was 1231±298 ms (σ_2: 24.21% of the mean). The resulting differences between Up90, Cd50 and Dn90 (61 ms, 168 ms and 66 ms, respectively) are within the uncertainty range for both experiments and are small compared to the mean values. This could have occurred due to biological variation between the hearts or unintentional

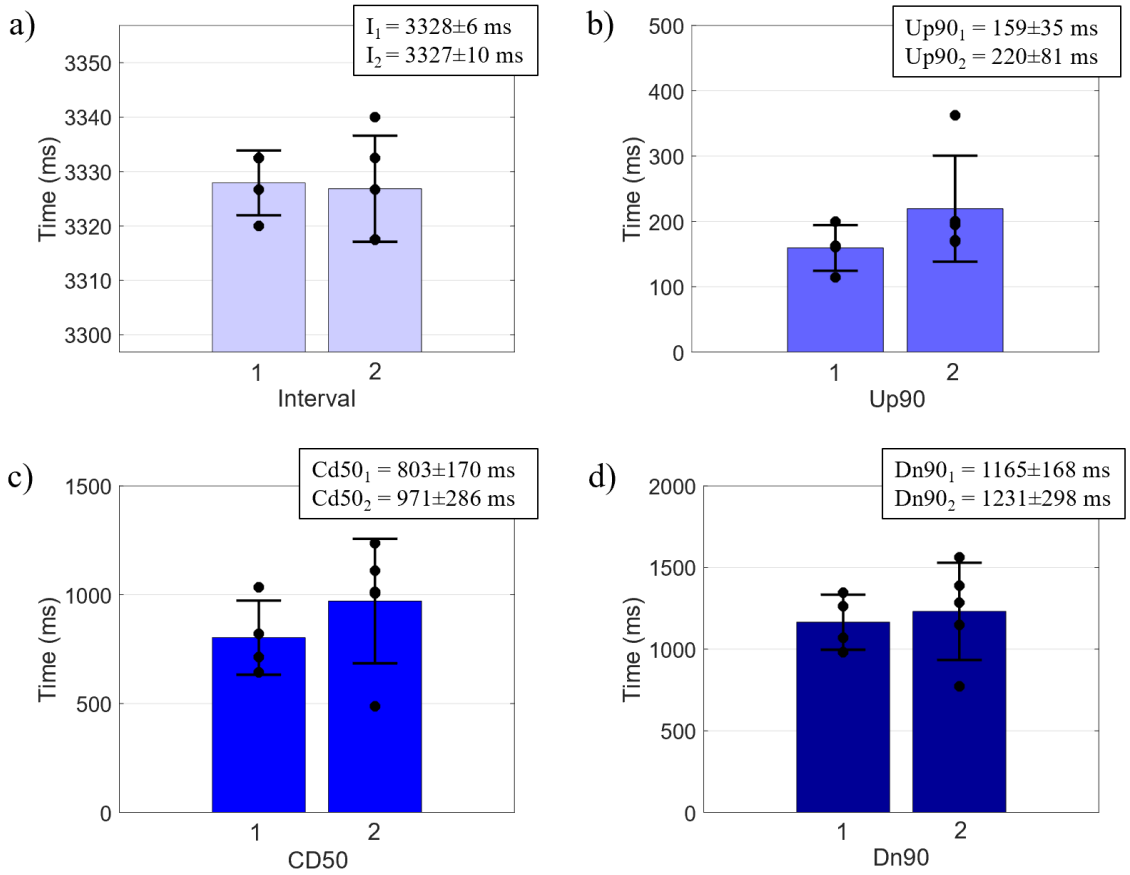

Figure 4.9: Variation of key contraction descriptors in room temperature acute rabbit cardiac slices from two hearts (bar plots 1 and 2). There were N_1=5 and N_2=4 slices in the two experiments. In some plots the corresponding number of data points is not visible as they are spaced very close together. The error bar is ± standard deviation (σ).

differences between the experimental protocols. The standard deviation from the mean was larger in the second experiment for all quantities, indicating the the variability of Up90, Cd50 and Dn90 among slices from the first heart was lower. However, it should be noted that in the second experiment, a significant contribution to σ is from an outlier trace, which displayed a twofold shorter contraction-relaxation profile than the rest of the slices, falling outside the error bars in Figure 4.9a-d). A larger sample size is needed to estimate the mean and variation with more confidence.

To assess the spatial variation of contractile properties across the sample, the recorded FOV was divided into a 19×19 grid, yielding 361 ROIs, which were then analysed in ContractilityTools via the previously outlined framework. The reader should note that for one slice from heart 2, the analysis algorithm in the ContractilityTools software failed. An example for one representative preparation (the slice from Figures 4.8 and 4.7) is shown in Figure 4.10a-d). In this particular slice, a total number of 339 ROIs out of 361 (93.9%) were successfully analysed. Analysis failure (corresponding

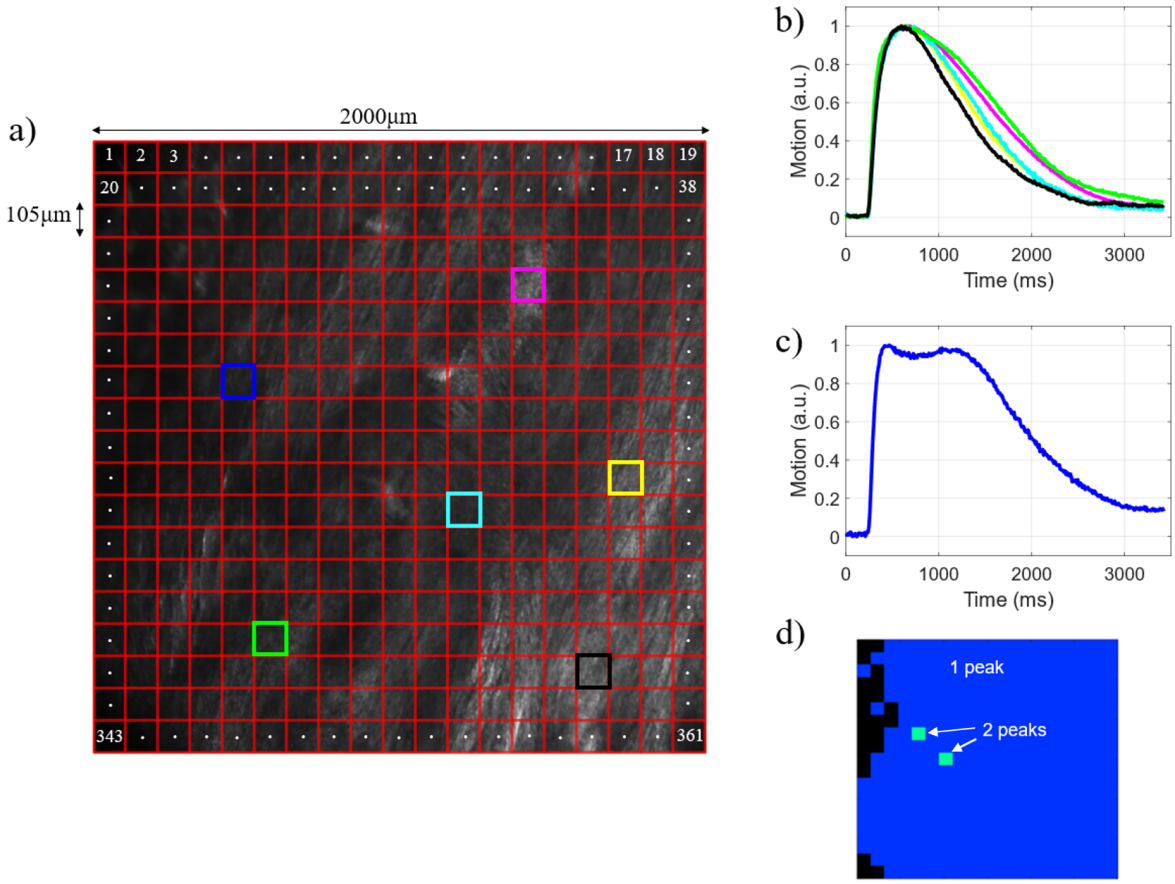

Figure 4.10: Sub-division of the FOV into a 19×19 grid (a). In b) and c), the average contractile profiles from various selected locations (corresponding to coloured squares in a) are shown. The vast majority of the profiles have a single peak and a similar contraction profile (b). Within the slice there are also instances of contractile profiles with 2 peaks (c). A map of the 19×19 grid in terms of the number of contractile peaks is shown in d). Black squares correspond to analysis failure.

to black squares in Figures 4.10d and 4.11a,b,d,e could have occurred due to blur at the edges of the FOV. Alternatively, due to imperfections in slice mounting, certain parts of the preparation may have been out of focus. From the averaged profiles of selected ROIs (Figure 4.10b) it can be seen that the muscle contraction is mostly consistent in shape and has a single peak, with an exception of the ROI highlighted in blue (Figure 4.10c), in which the contraction profile has two peaks. In Figure 4.10d, a map of the 19×19 grid is shown with blue and green corresponding to 1 and 2 peaks in the contraction profile, respectively. Across the slice, 99.4% of the ROIs (337 traces) had one peak, highlighting that the preparation displays almost no complex contractile behaviour.

The spatial variation of two properties across the imaged slice FOV is mapped: the change in contraction duration (previously defined in Figure 4.7 as Cd50) and the contraction start time. Contraction start time or activation time denotes when the

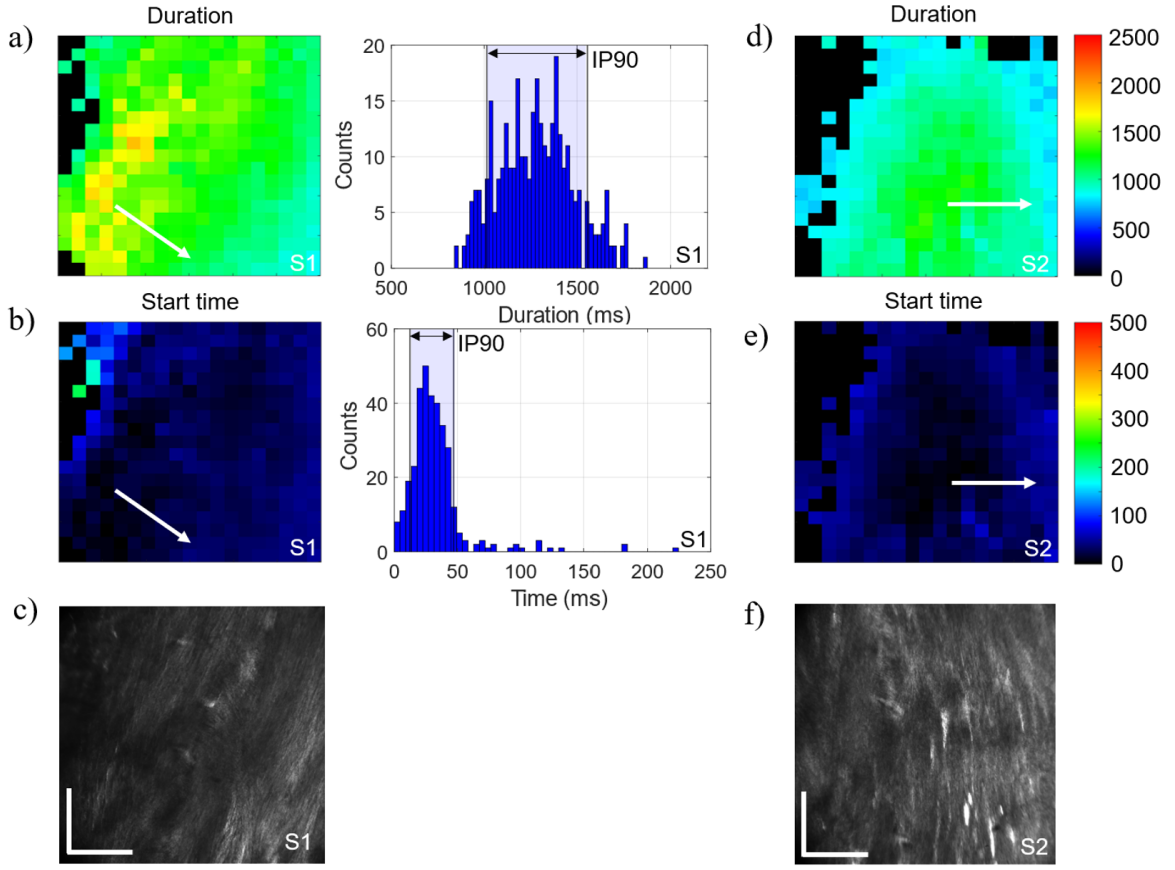

Figure 4.11: Spatial variation of contractile properties in slices S1 (a-c) and S2 (d-f). Contraction duration across the FOV for S1 and S2 is shown in a) and d), respectively, with the colour bar values in milliseconds. b, e): Heat-maps of activation times for S1 and S2, respectively, with the colour bar values in milliseconds. White arrows in the aforementioned plots signify the direction of change in values of Cd50 and start time. Black squares correspond to ROIs where the analysis failed. The distributions of Cd50 and activation time are displayed in the histograms for S1 only (a and b, right), with the highlighted blue area denoting the IP90 range (10^{th}-90^{th} inter-percentile difference). In c) and f) the recorded S1 and S2 FOVs are shown with the horizontal and vertical scale bars corresponding to 500 µm.

different ROIs in the 19×19 grid started contracting with reference to the region that contracted the earliest. This allows to investigate whether certain regions within the slice responded earlier or later to the electrical stimulation. The corresponding maps for two representative slices S1 and S2 are displayed in Figure 4.11. For S1, the mean activation time across the ROIs was 32.4 ms and the mean Cd50 was 1277.5 ms. The 10^{th}-90^{th} inter-percentile difference (IP90) as shown in the histograms for S1 in Figure 4.11 denotes the range of valid contraction start time and duration values within the slice. In other words, the values that fall outside the region are outliers that could have occurred due to analysis errors. Furthermore, the larger the IP90 value, the broader is the distribution of the values in question within the slice ROIs. For S1, the IP90

of activation time and Cd50 was 34.6 and 541.9 ms, respectively. The mean activation time and Cd50 of S2 were 30 ms and 978.5 ms, respectively, with the corresponding IP90 of 38.8 and 361 ms. As the IP90 range of contractile duration is lower for S2, it suggests a narrower distribution of Cd50 values across the slice FOV. Furthermore, in Figure 4.11a, it can be seen that for S1, the contractile duration changes from longer (approximately 1650 ms, orange-yellow) on the leftmost side of the FOV to shorter (approximately 1000 ms, green) towards the lower right-hand side of the FOV, along the direction of the white arrow. Curiously, in Figure 4.11b, the contraction activated earlier in the region corresponding to longer Cd50 (lower left corner). In the lower right region, the contraction started approximately 70 ms later. This change follows the same trend as the change in duration (white arrow direction). In Figure 4.11d and e, it can be seen that S2 displays similar behaviour (although the gradual change in Cd50 and activation time across the FOV is radial). While to make conclusions of statistical significance a larger sample size and a rigorous statistical analysis is necessary, it is evident that the change in the aforementioned values is gradual across the slice; there are no regions with sudden discontinuities. Note that the outliers in Figure 4.11b distribution hinting at late activation (past 100 ms) are outside the IP90 range and close to the regions where the analysis failed, suggesting poor reliability of those values.

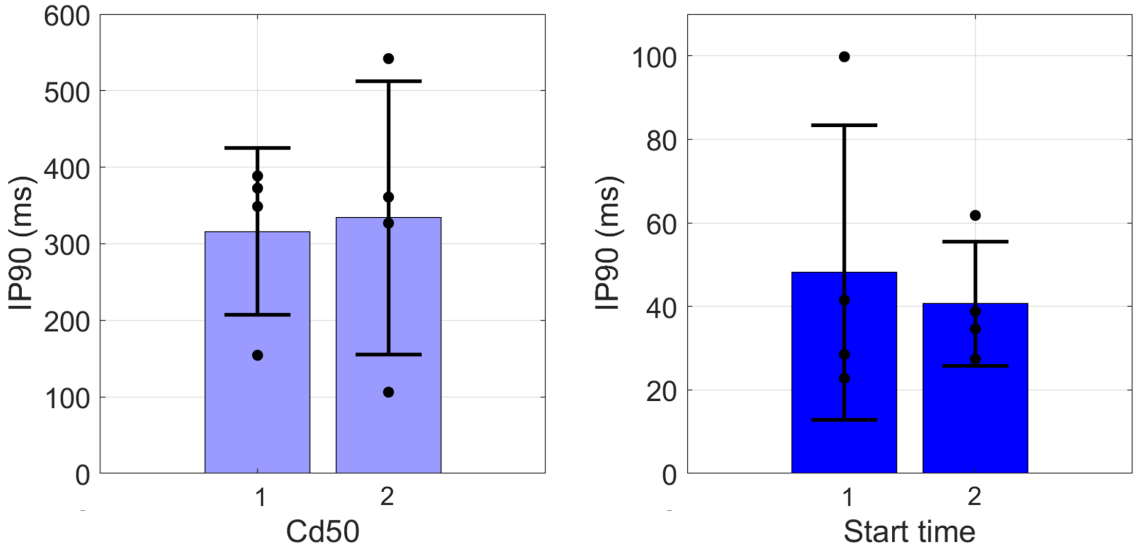

Figure 4.12: Variability of Cd50 a) and activation time b) across the FOV of N=4 slices in two experiments (bar plots 1 and 2 representing different hearts), expressed as IP90 (10^{th}-90^{th} inter-percentile difference). The data points correspond to IP90 of individual slices and the error bar is $\pm\sigma$ of the IP90 values. The reader should note that for one slice from heart 2, the analysis algorithm in the ContractilityTools software failed.

Considering all slices in the aforementioned two experiments, the same conclusion about the regular single-peak contraction profile can be reached. The mean percentage of ROIs with a single peak was 99.1±0.7% and 98.7±1.12% in the first and second

slicing sessions, respectively. The lack of complex contractile behaviour is an advantage of the cardiac slices as intact, 3D preparation where the vast majority of the cells are within their native environment. Monolayers of human induced pluripotent stem cell-derived cardiomyocytes, a lab-grown 2D preparation, exhibit significant spatially varying difference in contractile behaviour. In particular, a large amount of traces from such preparations show multi-peak behaviour. Additionally, the method of plating the monolayers has an impact on their contractile properties [71].

Regarding the range of contractile duration and the activation time values across the FOV for preparation from two slicing sessions, the mean IP90 for Cd50 and activation time across the slices was 316.23 ms (σ=108.79 ms) and 47.15 ms (σ=33.36 ms) in the first experiment and 334 ms (σ=178.8 ms) and 40.6 ms (σ=14.8 ms) in the second experiment, respectively (Figure 4.12). The relative large standard deviation of IP90 values between the slices suggests that the range of contractile durations and activation times of separate slices within the same preparation can be quite different. Nevertheless, neither of the slices showed discontinuities in Cd50 or activation time, only a gradual directional change, as discussed for examples in Figure 4.11a,b and d,e. It should be noted that the sample mounting is important and the slice should lay as flat as possible across the FOV. Folding tissue will result in parts of the slice being out of focus, impacting the results on contractility analysis more significantly, when smaller regions (not the full FOV average) are considered.

4.3.5 Optical mapping of cardiac slices with CellOPTIQ

The same microscope and multiwell screening platform with proprietary software (CellOPTIQ, Clyde Biosciences Ltd) was used to record FluoVolt intensity spikes in acute slices under electrical stimulation to visualise the AP and allow contextualising traces acquired with the 2P-RF system. A blue LED (λ =470 nm) illuminated the central region of the preparation and a 40X Olympus LUC PlanFlN 0.6 NA air objective was used to image a 200×200 µm area. Fluorescence was collected with a PMT tube sensitive to 510–560 nm wavelengths and digitised at 10 kHz [72]. The slices were stimulated at 1 Hz with 12 ms pulses of 50 V amplitude during the first and 30 V amplitude during the second experiment, respectively (electrical stimulation parameter choice is discussed in Section 4.3.3). All slices were submerged in Tyrode's recording solution with elevated calcium concentration (Section 4.2.2) to facilitate electrical activity. 30 mM BDM concentration was used for electro-mechanical uncoupling and motion artifact prevention in the AP traces [10].

The steps in CellOPTIQ analysis protocol are shown in Figure 4.13. For the time-averaged AP to be computed, more than 3 events have to be identified in the trace. Firstly, the decaying signal baseline due to photobleaching is subtracted from the raw

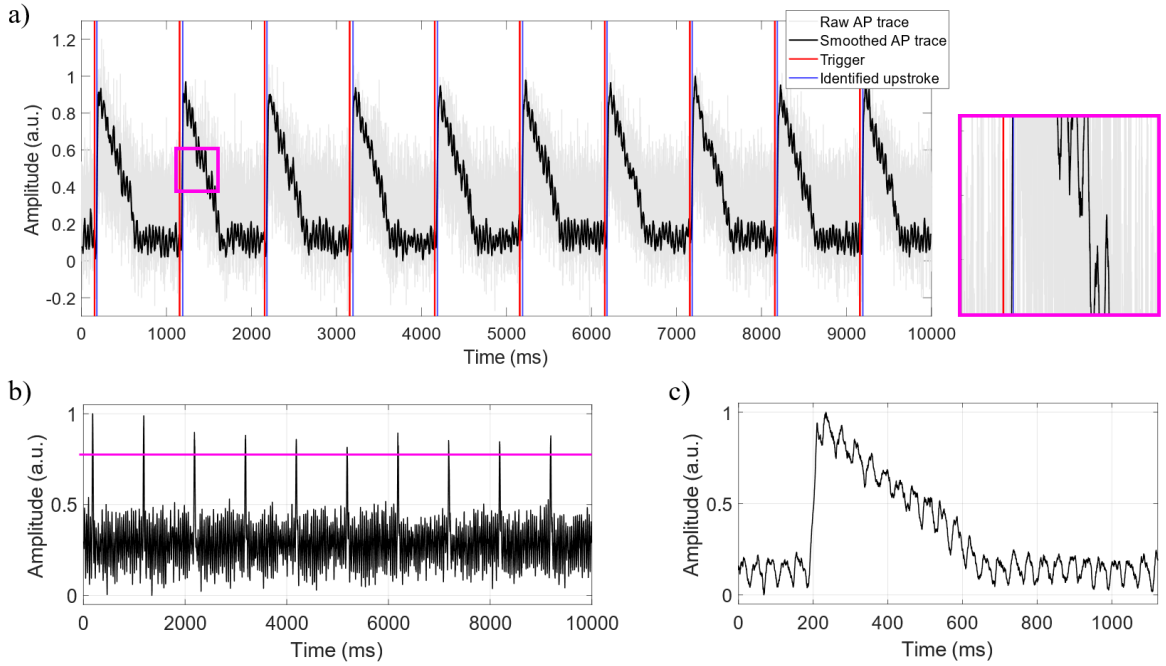

Figure 4.13: Steps of CellOPTIQ analysis protocol. a) AP trace (black) after baseline subtraction and smoothing with electrical stimulus (red lines) applied at 1 Hz. Raw trace is shown in light grey. There is a delay between the voltage impulse and the upstroke of an AP (magenta ROI). The upstroke time needs to be precisely identified (blue lines), which is done by taking the time derivative of the trace. b) Derivative of trace in a). The sharp peaks correspond to rapid depolarisation. Aggressive smoothing is needed to pick out all events in the trace from the noise by applying a threshold (magenta line). The average AP trace is shown in c). Note that the trace exhibits electrical noise which is impossible to notch-filter in CellOPTIQ software, therefore complicating further analysis.

trace. As there is a delay between the electrical stimulus (red lines) and the upstroke, identification of individual event times is needed (blue lines), which is done by smoothing the raw trace (Figure 4.13a) and taking the time derivative, as shown in Figure 4.13b. The peaks correspond to rapid depolarisation (upstroke). This is then used to find the upstroke and average the AP interval-wise after re-loading the original trace and applying minimal filtering (Figure 4.13c). From the average AP trace, quantities such as the depolarization time (TRise, time from 10 to 90% of amplitude) and AP duration (APD) at 90%, 75% and 50% repolarisation are calculated. In CellOPTIQ boxcar or moving average filter is used. Aggressive filtering before taking the derivative does not change the estimated upstroke times significantly, and a higher degree of filtering can be used when it is difficult to differentiate the events from the noise. Nevertheless, even relatively gentle boxcar smoothing before retrieving the time-averaged AP impacts the estimated APDs and TRise, therefore it should be kept to a minimum. Generally, filtering setting of 200 and 50 is used before the derivative and to obtain the

average AP trace, respectively.

The mean interval, TRise and APDs as well as their variation within N_1=6 and N_2=5 slices from two hearts is displayed in Figure 4.14. APs were recorded at 30 mM BDM concentration.

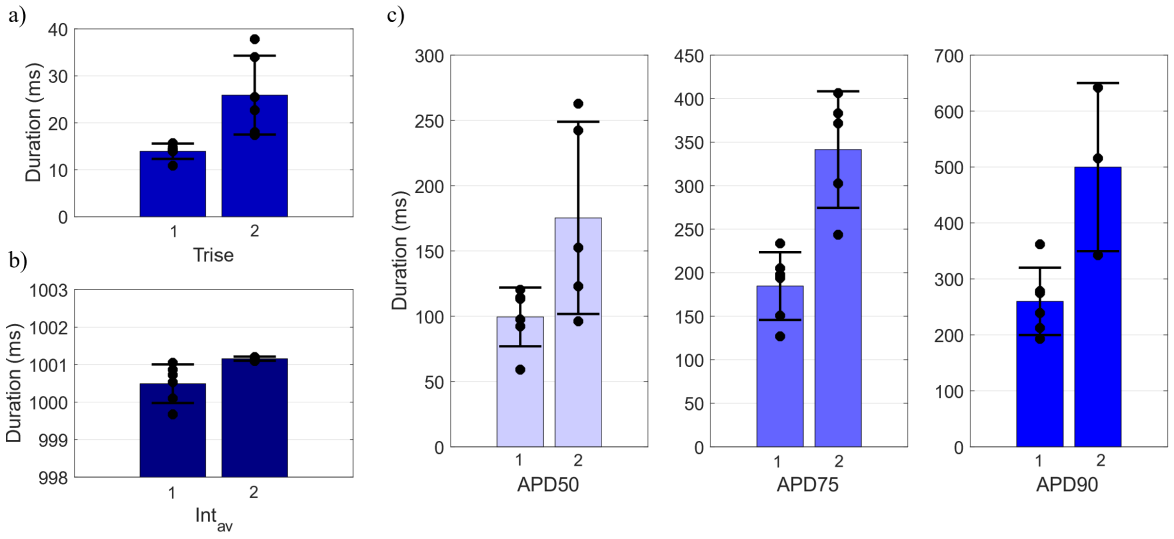

Figure 4.14: Variability of TRise (a), interval (b) and APD (c) in room temperature rabbit cardiac slices paced at 1 Hz in two slicing sessions (N_1=6 and N_2=5 in bar plots 1 and 2, respectively). Note that for 2 slices in the second experiment, APD90 was impossible to determine due to noise.The error bar is $\pm\sigma$.

As in the case with contractility assessment, the variation in mean interval was very low (1005.0±0.52 and 1001.1±0.05 ms in the first and second experiments, respectively), indicating that the slices respond to the electrical stimuli consistently. The mean TRise in the first experiment was by close to a factor of 2 shorter: 13.95±1.63 ms (σ_2: 11.67% of the mean) compared to 25.9±8.4 ms (σ_2: 32.4% of the mean). The lower variability of TRise in the first experiment could indicate either better sample quality or a more rigorous experimental protocol (slices were subjected to less experimental variation; for example, temperature during slicing, the optical recordings were consistently less noisy due to better sample mounting, the concentration of BDM well to well was more consistent). In general, all the measured quantities show lower variability in the first experiment. A larger number of hearts should be inspected to elucidate the variability of TRise and APDs between slicing sessions and to decouple genuine biological variation from discrepancies in following the experimental protocol. In particular, for the traces in CellOPTIQ software should be considered, a threshold on signal to background ratio could established to quality control the recordings.

The APD50, 75 and 90 (action potential duration at 50, 75 and 90% repolarisation, respectively), as shown in Figure 4.14c, are 99.46±22.51 ms (σ: 22.63% of the mean), 184.65±38.91 ms (σ: 21.07% of the mean) and 259.88±60.26 ms (σ: 23.19%

of the mean) for the first experiment. On the other hand, The APD50, 75 and 90 were measured to be 175.3±73.6 ms (σ: 42% of the mean), 341.5±67 ms (σ: 19.6% of the mean) and 499.9±150.3 ms (σ: 30.1% of the mean) for the second experiment, respectively. Overall, action potential duration was shorter in the first experiment. The variability of the aforementioned quantities is significant, partly due to the noise in optical recordings. For APD90, results from 2 slices had to be excluded, as the analysis failed, suggesting the APD90 value may be difficult to compute in the 2P-RF experiment as well, which is also susceptible to optical noise.

Comparing the obtained mean APD90 to that in a physiological rabbit model (200 ms), it is evident that the keeping the slices at room temperature can potentially prolong the action potential duration by approximately 2.5 times (if the result of the second experiment is considered). Nevertheless, the value from the first experiment is close to the physiological, although the experimental protocol was the same.

4.3.6 Effects of BDM concentration on AP properties

As discussed in Section 4.2.2, 2,3-Butanedione monoxime is used as an electromechanical uncoupler in order to immobilise the cardiac muscle without preventing electrical signal conduction. It is not necessary to have the slice completely stationary during optical mapping, where signal from a large FOV contributes to recording the AP at a high frame rate. Indeed, APs of 2D cardiac monolayers can be reliably measured with no BDM or Blebbistatin added [71]. It should be noted that intact tissue preparations are expected to move more than organoids or monolayers. Furthermore, it is critical to prevent motion artifacts during rapid line scanning in 2-photon imaging where the signal is expected to be acquired at a fixed depth in tissue from a specific population of cells. In [3, 57, 58], 10 mM of BDM together with 10 µM of Blebbistatin are used to render Langendorff-perfused hearts stationary. In the original publication detailing the preparation of cardiac slices, 30 mM BDM is proposed to immobilise the slices for calcium trace recordings. AP and contractility recordings were taken of 6 slices in 3 BDM concentrations: 15, 20 and 30 mM during one slicing session for 6 slices. Between the concentration changes, the slices were allowed at least 12 min incubation time. Generally, 4 recordings were obtained from different regions within the slice. Note that for a small percentage of those recordings (6.94%) the analysis failed due to poor SNR. An attempt was made to record APs also at 0 mM BDM, however the motion artifact prevented APs from being resolved correctly.

As shown in Figure 4.15, with increasing BDM concentration, the mean action potential duration across averaged slices is shortened. For example, the mean APD90 is 500.43±143.31 ms, 404.15±100.07 ms 262.42±67.48 ms at 15, 20 and 30 mM BDM, respectively. This is true for all APD90, APD75 and APD50, although the linear

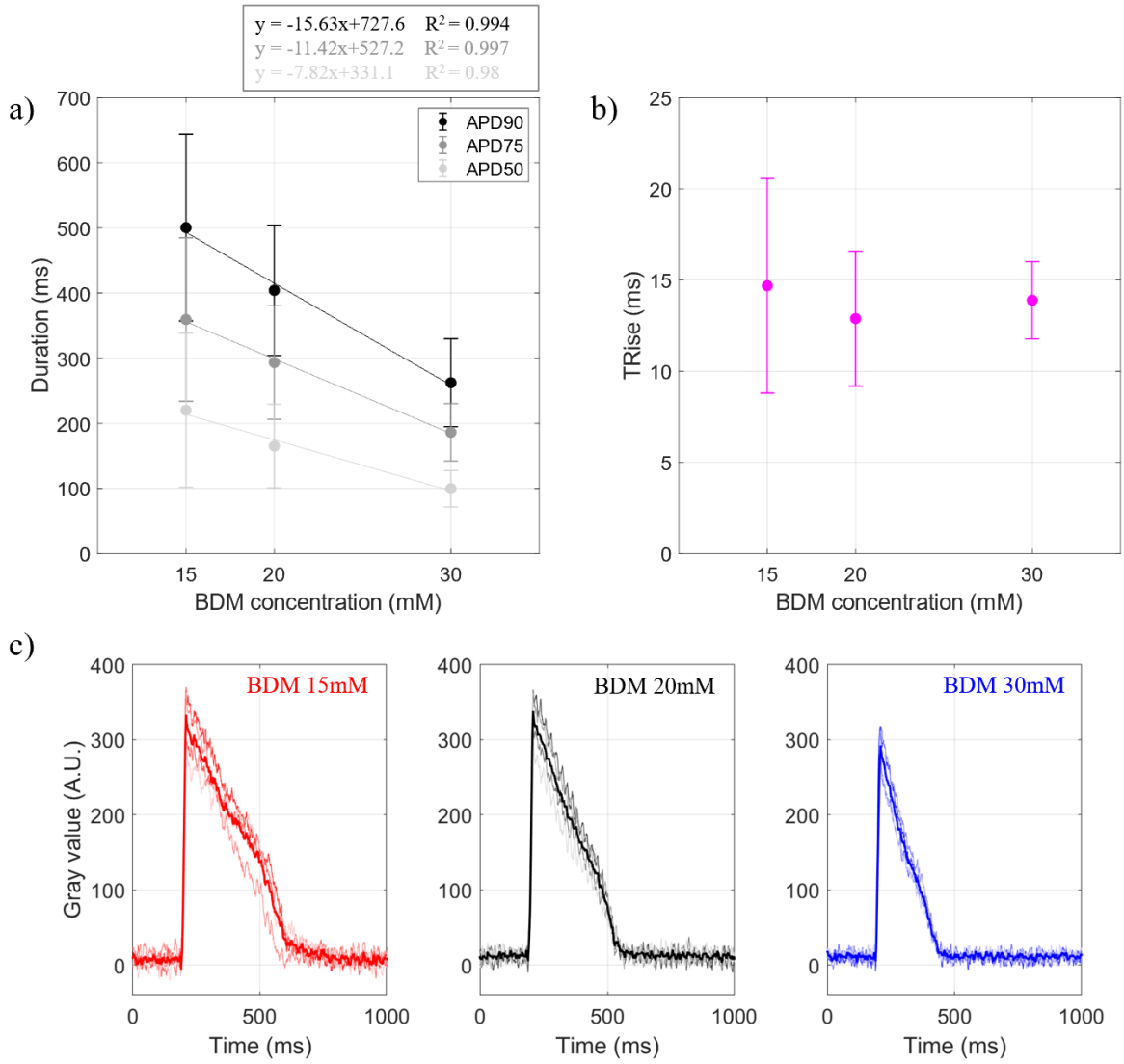

Figure 4.15: Impact of increase in BDM concentration on mean action potential properties of all 6 slices from one experiment. In a, the mean action potential duration at different degrees of repolarisation is shown to be shortened with larger BDM molarity. The mean APD values are obtained from traces from all 6 slices, with the error bar corresponding to $\pm\sigma$. The equations for linear fits and the goodness of fit metric is shown in the top right corner. An example of APs recorded from several regions within one slice is displayed in c). The thicker solid lines indicating the average APs. In b, the change in upstroke rise time with different BDM concentration is shown.

decrease of APD75 and 50 has a shallower gradient, as shown in the fits in Figure 4.15a. Note that the linear trend describes the change in duration with increasing BDM well, as the R^2 value of the linear fits exceeds 0.98 for all APDs. From the error bars it can be seen that the range of APD values is reduced with increased BDM concentration. This could be explained by a reduced impact of motion artifacts to FluoVolt spiking recordings. In Figure 4.15b, it can be seen that with increasing BDM concentration, TRise stays approximately constant. At 15, 20 and 30 mM BDM, TRise

was measured to be 14.68±5.88 ms, 12.89±3.71 ms and 13.89±2.11 ms, respectively, showing a difference of only a couple of ms. Importantly, the standard deviation of the mean is reduced by a factor of 2.79 from 15 mM to 30 mM BDM, again suggesting that reduced motion artifacts yield less variability in rise time. In Figure 4.15c, average AP traces are shown for one slice. It can be seen how the shape of the action potential is preserved, while its duration is shortened with increasing uncoupler concentration. It should be noted that the traces were recorded at a different point in time, and the measurements at 30 mM were taken approximately an hour later than those at 15 mM.

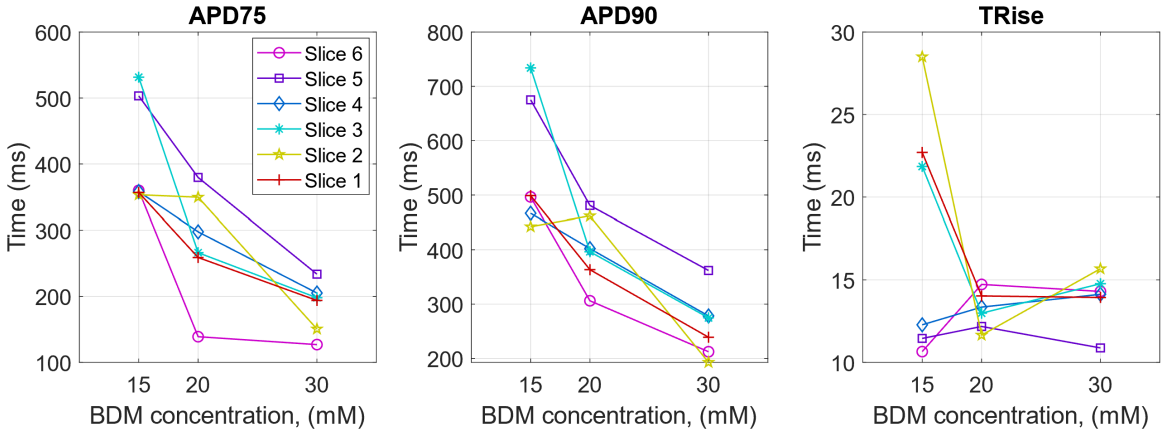

Figure 4.16: Impact of increase in BDM concentration on APD75, APD90 and TRise of individual slices. Slice 6 was cut from tissue that is furthest away from the epicardium and slice 1 is the slice closest to the epicardium.

To verify that the same trend is true also for individual slices, not just the overall average, APD75, APD90 and TRise values for each slice with varying BDM molarity was plotted, as shown in Figure 4.16. It is evident, that the same trend is observed in 5 out of 6 individual slices: increased BDM concentration shortens the AP. Only in slice 2, no significant change was observed from 15 mM to 20 mM BDM, although at 30 mM it was shorter. This could have occurred due to a missed well when changing solutions. The range of TRise values is large at low BDM concentration. While for slices 1-3 (epicardial slices) the value appears to be shortened with increased BDM, it is most likely due to residual motion artifact. For APD, no obvious trends arise with slice distance from the epicardium (slice 6 is 2 mm away and slice 1 was cut from tissue closest to the epicardium).

It should be noted that in contractility recordings with a 4X objective, residual motion was visible with 15 mM and 20 mM BDM. With 30 mM, when 40X was used to zoom into the sample, faint residual motion was picked up by ContractilityTools software in 4 out of 6 slices, suggesting that BDM molarity of at least 30 mM should be used in 2P imaging to prevent the motion artifacts fully, depending on the objective choice (20X in the 2P-RF system detailed in Chapter 3). Additional Blebbistatin

could be added if motion artifacts prove persistent in 2P line traces, to avoid toxicity associated with further increasing the molarity of BDM. In that case, the effect of Blebbistatin to the action potential duration in room temperature rabbit slices should be assessed. With high BDM concentration, the shortened AP duration should be taken into account (sampling rate and line scanning speed need to be sufficient to resolve TRise).

4.3.7 Effects of hypothermia on contractile and electrical properties

It should be noted that for a robust assessment of the contraction profile, the tissue needs to relax fully. In Figure 4.17, contractility traces of a slice stimulated at 1 Hz and 2 Hz are displayed. The muscle does not have enough time to relax under these conditions. Therefore, for slices at room temperature, the frequency of electrical stimulation needs to be low (e.g. 0.3 Hz, as shown in Figure 4.8b if a contractility assay is to be conducted. This is true even if the action potential propagation is normal at 1 Hz stimulation in room temperature (Figure 4.13a).

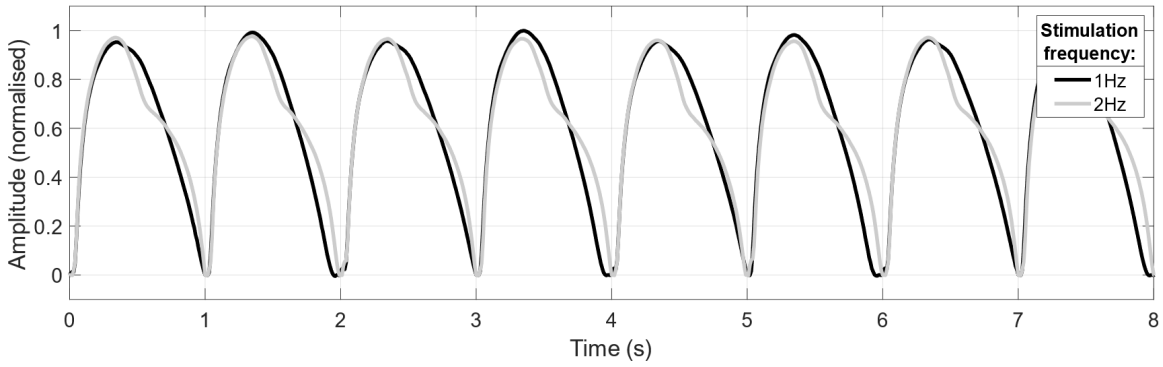

Figure 4.17: Slice contraction under 1 Hz (black) and 2 Hz (gray) electrical pacing frequencies. In both cases the cardiac fibers do not relax fully.

Because the blue LED is used in CellOPTIQ (or the pulsed IR laser in the 2P-RF system) it is important to pace the preparation at a frequency sufficiently high to acquire enough AP events to reliably time-average (prolonged exposure to light leads to photodamage and photobleaching of FluoVolt). However, very few slices kept at room temperature tolerate 2 Hz pacing; this translates to either a missed beat or a low amplitude AP during every other stimulus (alternans). Stimulation frequency and pacing no higher than 1 Hz should be employed for investigation of AP properties, allowing 9 events to be recorded within a 10 s acquisition time.

4.4 Summary

To summarise, we have successfully established a protocol to produce, mount and electrically stimulate acute rabbit ventricular slices at room temperature (Figure 4.4), modified from [10]. All preparations were obtained from hearts that were previously used in another experiment, in accordance with the University's mitigation and refinement strategy on animal research [11]. Because the tissue was re-used, multiple qualitative and quantitative methods to assess slice viability and quality were utilised. The reader should note that Langendorff perfusion is usually considered the end point of the tissue. The fact that acute slices can still be obtained and characterised as described in the optimisation protocol in this Chapter suggests that the cardiac tissue can enter another quantitative experimental pipeline. This is beneficial to our cardiovascular science collaborators and supports the reduction of animal research.

Firstly, live-dead TTC staining of tissue immediately after slicing showed that most of the central slice area remains viable and only the edge of the cut contains electrically inert and metabolically-inactive tissue (Figure 4.5b). This informed that any smaller area to be selected for mounting (Figure 4.4e,d) should be cut from this central region. Importantly, as slices from different depths within the ventricular block were stained uniformly, no hypoxic core was formed in the middle. This reinforces that the temperature control of the Tyrode's slicing solution (4-10 °C) successfully protects tissue viability.

Electrically stimulated acute slices responded with mechanical contraction, which allowed a quantitative investigation using the CellOPTIQ system [72]. The slices were submerged in Tyrode's recording solution with 0 mM BDM under 0.3 Hz pacing. Average contraction traces were acquired with ContractilityTools software and the mean interval, Up90, Cd50 and Dn90, as defined in Figure 4.7 were calculated for slices from two hearts (Figure 4.9). For example, the mean contraction time $Up90_1$ was 159±35 ms, $Cd50_1$ was 803±170 ms and the relaxation time $Dn90_1$ was 1165±168 ms in the first experiment. The resulting differences of these quantities (61 ms, 168 ms and 66 ms, respectively) between the two slicing sessions are within the uncertainty ranges for both experiments and could have occurred due to biological variation between the hearts or unintentional differences between the experimental protocols. In the two hearts, the variation in interval value was observed to be negligible, evidencing that the slice contraction follows electrical stimulation consistently. Performing further spatial analysis by subdividing the imaged FOV to a 19×19 grid (Figure 4.10a) showed that the spatial change in Cd50 is gradual in most slices (representative maps in Figure 4.11a,d). Overall, the consistency of contractile response within the individual slices evidenced preparation viability. Data from more hearts is needed to ascertain the variability of

Up90, Cd50 and Dn90 between different organs with more confidence.

Under electrical stimulation, the resulting action potentials within the slices were detected via optical mapping (by recording FluoVolt spiking) using the CellOPTIQ microscope (Figure 4.13); 1 Hz stimulation and 30 mM BDM was used. The mean interval, TRise and action potential durations at various degrees of repolarisation as well as their variation within slices from two hearts was assessed (Figure 4.14). As in the case with contractility, the variation in mean interval was low, indicating that the slices respond to the electrical stimuli consistently. Nevertheless, the difference between mean TRise and APDs measured across the two slicing sessions was more pronounced than that for contractility. Overall, both TRise and action potential durations were significantly (by approximately a factor of 2) shorter in the first experiment (Figure 4.14). For example, the mean TRise in the first experiment was 13.95±1.63 ms compared to 25.9±8.4 ms in the second experiment. The lower variability of TRise and APDs in the first experiment could indicate either better sample quality or that the slices were subjected to less experimental variation. More data is needed to ascertain the variation of mean TRise and APDs between different hearts.

Finally, the effect of 2,3-Butanedione monoxime concentration (15, 20 and 30 mM) on AP properties was investigated in N=6 slices from one heart (Section 4.3.6). It was found that a higher concentration of BDM consistently shortened the action potential duration (Figure 4.15a). For example, the mean APD90 was 500.43±143.31 ms, 404.15±100.07 ms 262.42±67.48 ms at 15, 20 and 30 mM BDM, respectively. Nevertheless, the increased uncoupler molarity did not affect the TRise of the upstroke (Figure 4.15b). This was true if the values were averaged for all slices in the study (Figure 4.15a,b as well as if the trend for individual slices was examined (Figure 4.16). Experimental data from more hearts is needed to ascertain whether this effect persists. Importantly, the effect of time (and the resulting natural denaturation of tissue) could be excluded by first imaging the slices submerged in the highest concentration of BDM.

Acute rabbit ventricular slices detailed in this Chapter will be used to test the capability of the 2P-RF microscope to image in highly scattering cardiac tissue (Chapter 5). Importantly, the preparations will also allow to assess whether the microscope is capable to probe action potential properties in longitudinal and transmural directions in electrically stimulated slices (Chapter 6). For the latter, the live-dead TTC staining (Section 4.3.2) as well as observing consistent, regular mechanical contraction patterns (Section 4.8) evidences uniform viability within the slices. Importantly, the preliminary characterisation of AP properties (4.3.5) such as the upstroke rise time and action potential duration at various stages of repolarisation will allow contextualising the corresponding results from the 2P-RF microscope. Although the mean TRise and APD values displayed in Figure 4.14 for preparations from two hearts differ by approximately

a factor of 2 (TRise was 13.95±1.63 and 25.9±8.4 ms and APD90 was 259.88±60.26 ms and 499.9±150.3 ms), if the values measured with the 2P-RF system fall significantly outside this range, troubleshooting will be pursued. In that case, effects of experimental or analysis errors as well as the impact of residual motion artifacts or laser-induced tissue damage will be considered. Importantly, despite its significant variability across the preparations, both longer and shorter TRise and APD values in room temperature slices are compatible with longitudinal (galvanometric mirror) as well as transmural (remote refocusing module) scanning speeds. Finally, the work described in this chapter will also inform the electrical stimulation protocol (for example, the optimal pacing frequency, as discussed in Section 4.3.7) as well as the BDM concentration needed to prevent motion artifacts (and any effect on the AP duration that it may have, as discussed in Section 4.3.6).

Chapter 5

Imaging of cardiac slice structure with 2P-RF system

The RF-2PM system detailed in Chapter 3, was first validated by performing fast imaging of FluoVolt labelled rabbit cardiac slice structure (Chapter 4). We demonstrate significant improvement in allowed imaging speed of z-y planes acquired with remote refocusing, compared to corresponding conventional microscope z-scan reslices. Therefore, the microscope can be used for faster transmural myocardium structure assessment. The purpose of this Chapter is to qualitatively validate that the 2P-RF microscope is capable of deep tissue imaging in highly scattering cardiac preparations and all work described is my own.

5.1 Enhanced cardiac slice structure imaging speed

The Scientifica 2PM is controlled with LabView implementation of SciScan 1.2 interface. The surface of the cardiac slice was identified with 2D live imaging mode. Firstly, a regular z-scan was facilitated where the objective was repositioned in z with the microscope's translation stage (step size of 0.5 µm). Frames with x-y FOV of 350 µm × 350 µm (512 × 512 pixels) were imaged with a total scan duration of 14 min; 4 frames per plane were acquired for averaging. The pixel dwell time was 2 µs and in total 175 z-planes were acquired. To probe the axial frames directly, the sample was moved so that the nominal RF mirror position was below the surface, corresponding to the middle of the z-stack scan range. The mirror was then actuated at 122 Hz using an attenuated triangular voltage waveform, originally generated by SciScan to drive the fast galvanometric mirror (x). The slow mirror (y) was scanning normally across the distance of 350 µm, consistent with x-y imaging dimensions. Note that as in Section 3.7, an appropriate start delay option was chosen. The pixel dwell time was 8 µs and the scan consisted of 512 × 512 pixels; therefore, 512 z-planes were acquired directly.

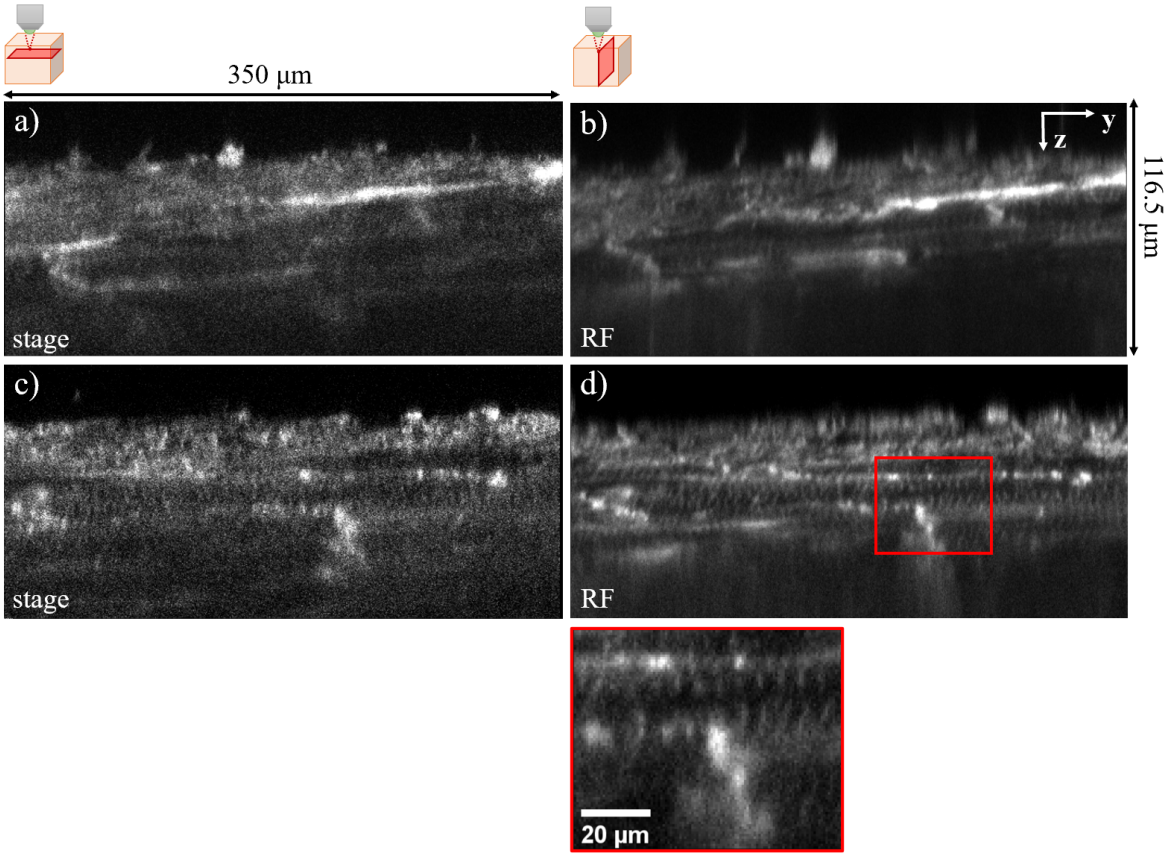

Figure 5.1: Fast imaging of transverse cardiac slice structure shows qualitative agreement of myocardium features. Furthermore, the time to obtain axial frames is reduced significantly with remote focusing. Fast (122 Hz refocusing speed) RF z-y frames (b, d) are comparable with corresponding regular z scan reslices (a, c). Stage z-stack required approximately 14 min to obtain while the averaged RF image required 8.4 s (4.09 ms / vertical line); averaging allows improved SNR. Demarcation of cardiac cell membranes and sarcomere spacing is resolved (lower right). Image contrast is adjusted to better display the features.

In Figure 5.1, cell structure of the ventricular preparation was imaged with the RF module (b, d) and compared with the corresponding reslices of conventional microscope scan (a, c) (λ=800 nm excitation wavelength and 22 mW average power at sample with RF). Both scans show qualitative agreement between the structures. Importantly, bright FluoVolt-stained boundaries between cardiomyocytes are observed in RF scan. These likely correspond to intercalated disks (which are key in facilitating the cell to cell electrical signalling), although further validation with a structure-specific stain is required to confirm this. The reslice of the conventional z stack (Figure 5.1a, c) took 14 minutes to obtain, while the 4 RF z-y frames summed in Figure 5.1b and d were acquired in 8.4 s (4.09 ms/vertical line in individual frame). Depending on the FOV size and other parameters, this timeframe could be either prolonged or reduced (e.g. by selecting an FOV of 100 µm × 350 µm). If a single x-z line was acquired convention-

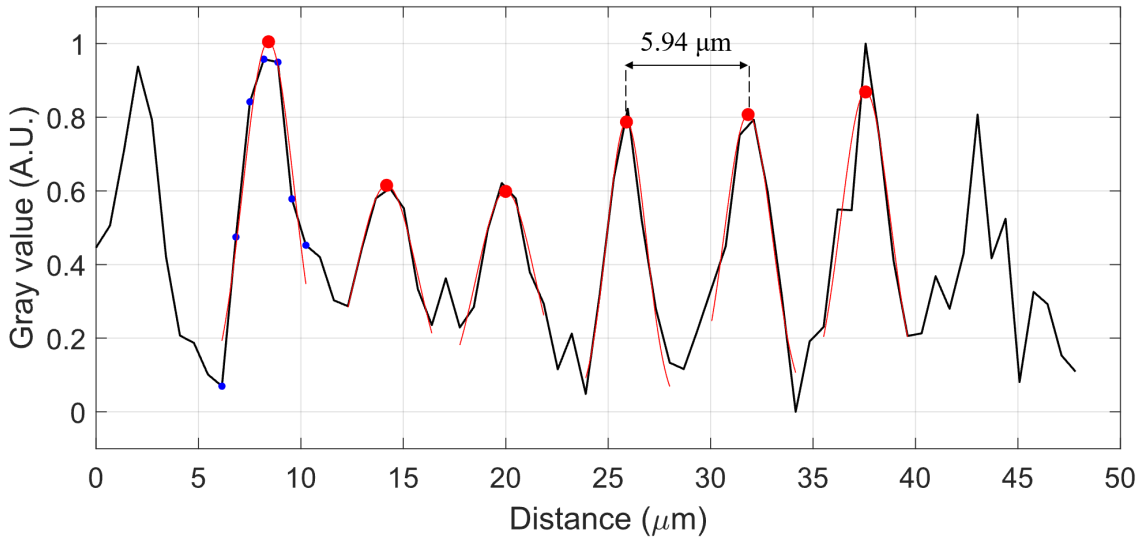

Figure 5.2: Sarcomere spacing deduced from a line profile in 2P-RF scan: gray value is plotted against distance in y (black). Fitting a Gaussian (red) over each peak (blue data points) allows evaluating the distance between the peak positions corresponding to sarcomere length.

ally, the time taken would be longer (approximately 17.5 s), due to the translation of the bulky sample objective prolonging the scan (with the stage repositioning time in z approaching 100 ms). In RF scans, recording several frames per plane in seconds allows improving the signal to noise ratio. In the conventional scan, without increasing the pixel dwell time, the SNR could be enhanced by increasing the average power instead; however, the exposure of the tissue region to the laser over the prolonged z-scan could lead to damage and reduced viability, critical in functional imaging of acute slices. In Figure 5.1, it can be seen that there is some mismatch in the features; this should be interpreted with reference to the distortion of the system, detailed in Section 3.6. While a hint at sarcomere striations appears in RF-2PM scan potentially due to autofluorescence, with a more suitable staining protocol, the contrast can be improved. Examining a line profile in y across the red ROI in Figure 5.1d, the variation of gray value allows identifying actin and myosin filament spacing, as shown in Figure 5.2.

The average spacing was estimated by fitting a Gaussian function over each peak (7 pixels wide, blue data points) in MATLAB and extracting the distance between each peak position (red dots). For instance, the distance between the 4th and the 5th gray value peak is 5.94 µm. The mean spacing among the evaluated peaks was 5.83±0.086 µm. The standard deviation and hence the uncertainty in the value is low across the line profile inspected. This spacing is larger than the physiological value (approx 2 µm), as the slices were arbitrarily stretched during sample mounting. While this is good for a quick assessment, with a more robust imaging and data analysis protocol, our microscope could be applied also for fast and precise measurement of

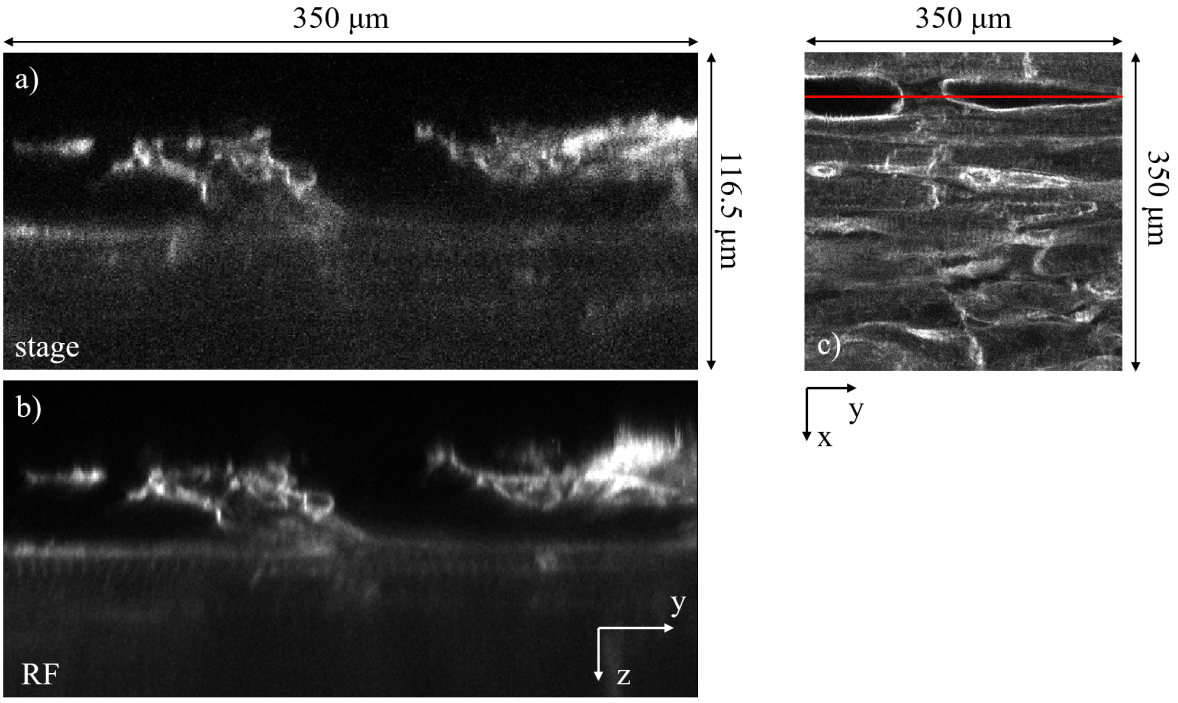

Figure 5.3: Fast imaging of transverse cardiac slice structure shows qualitative agreement of myocardium features. In c), the red line indicates the x coordinate of the frames in a) and b) (x=47.84 µm, if 0 position for the x axis was the top of the frame in c). Image contrast is adjusted to better display the features.

sarcomere length. Indeed, remote focusing has been used before with 2PM to assess filament spacing and correct for imprecision in the values due to variation in cell orientation within the cardiac preparation [8]. In the aforementioned study, rat hearts were Langendorff-perfused and loaded with di-4-ANEPPS VSD. Note that for precise investigation of structural features in the scale of several microns, our RF system should be better optimised across the whole FOV. As discussed in Section 3.3.3, the distortion introduced by the RF module can exceed 30 µm laterally at the extrema of the FOV imaged. While this is acceptable in functional imaging, where only cell-to-cell electrical signalling is in question, in precision sarcomere spacing measurements distortion like that would be detrimental. In the previously mentioned study [8], the 2P-RF microscope was calibrated using a specialised 3-dimensional sample to account for distortion and magnification mismatch effects [36], enabling a precision study on sarcomere spacing.

Our 2P-RF microscope can also be used to assess other large structural features within the slices that extend in the axial direction. For example, in slices produced from tissue close to the epicardium, blood vessels are often present. In Figure 5.3, visualisation of such a vessel is shown in slow scan (stage, a) and fast (RF, b) scan. The hollow regions in the slice surface correspond to the red line in Figure 5.3c), where

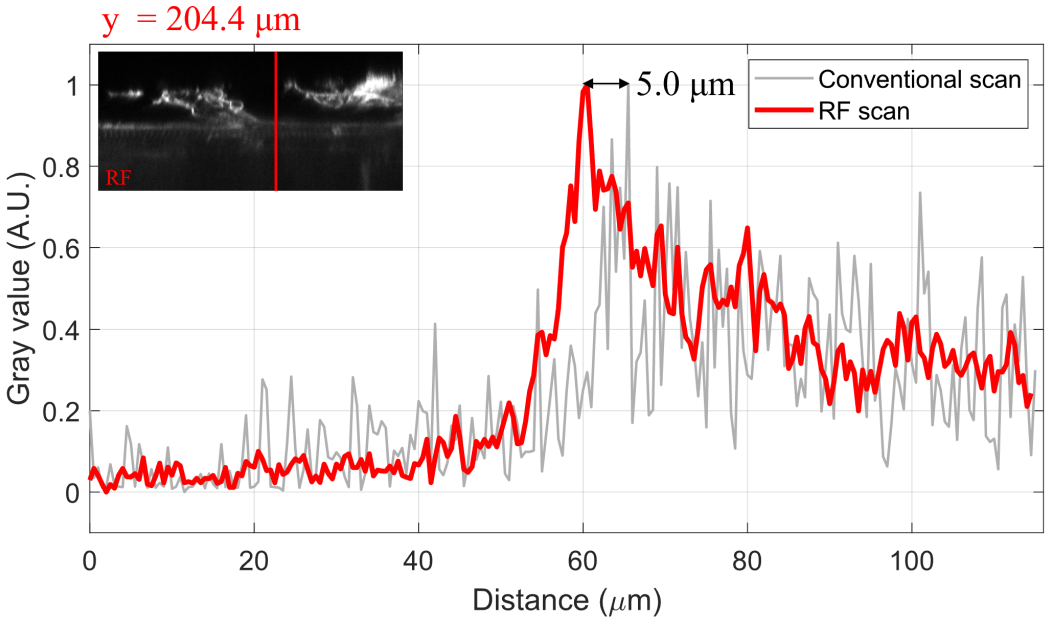

Figure 5.4: Comparison of vertical line profiles of RF (red) and conventional (gray) images of vessel structure from Figure 5.3 at y=204.4 µm (indicated at the top left corner). For the purpose of this comparison, gray values of both images were scaled between 1 and 0.

an x-y plane of the region is displayed. In particular, the red line denotes x=47.84 µm, if 0 position for the x axis was the top of the frame in Figure 5.3c.

A comparison of vertical line profiles of these images is displayed in Figure 5.4. It is evident that the line profile from RF scan (red trace) has significantly less noise than that from the conventional scan (gray trace). Furthermore, in the gray trace, the noise obscures the region where the vessel ends and cardiac cells begin (approximately 50-60 µm in z). This transition is much more clearly resolved in RF scan (red). As discussed before, increasing average power or exposure time could improve the noise profile in the conventional scan, although with a potential risk of reducing tissue viability with laser exposure during the long z-stack acquisition. It should be noted that there is a 5 µm mismatch between the exact onset of this transition between both scans. This discrepancy was discussed in Section 3.3.3 and the extent of it differs across the imaged FOV. As discussed before in relation to sarcomere spacing quantification, this is a significant mismatch if precision measurements of cardiac structure were to be carried out (similar to those in [8]). Nevertheless, as 5 µm constitutes only a quarter of the height of a typical cardiomyocyte, for functional imaging this discrepancy is acceptable. If system alignment (Section 3.3) was revisited and a calibration sample was used, together with post-processing as described in [36], the system could be improved to allow precision measurements in the micrometer scale. However, currently, the 2P-RF microscope enables rapid structure assessment in the scale of several micrometers,

which could help identifying blood vessels within the tissue and for example avoiding that region in 2P-line scanning as hollow vessels will not contribute to detected APs (FluoVolt spikes). This can be done within several seconds as opposed to minutes, which is especially beneficial when time sensitivity of experiments with live samples is considered.

5.2 Summary

The 2P-RF microscope was applied for fast cardiac slice structure imaging. Time required to obtain frames in the axial direction was reduced (from 17.5 s to 8.4 s), evidencing the microscope's capability for rapid scanning in the axial dimension. While the microscope was not optimised to precisely assess structural features of several microns in length, a fast measurement of sarcomere spacing could be made to inform sample mounting: the mean sarcomere length within one cell imaged was 5.83±0.086 µm, without accounting for its orientation. Additionally, the axial extent of larger structures such as blood vessels can be visualised rapidly with the 2P-RF system. In all frames acquired, the cell demarcation lines were clearly resolved with their structures being the most intense across the image. As these parts of the cell will contribute the most significantly to transmitting the electrical signal and hence the change in FluoVolt fluorescence intensity, the 2P-RF microscope holds potential for functional imaging and resolving the action potential in acute rabbit cardiac slices.

Chapter 6

Probing action potentials in acute cardiac slices with 2P-RF microscope

In the following sections, the 2P-RF microscope detailed in Chapter 3 is applied to study the action potential propagation in acute rabbit cardiac slices (Chapter 4). In Section 6.1, existing literature on investigating electrophysiology in cardiac models with 2-photon microscopy is reviewed. In Section 6.2, a 2PM protocol utilising fast galvanometric mirror line scanning is established to resolve APs in longitudinal planes within the slice, while RF module optics are bypassed. Then, the complete 2P-RF system is used to verify AP detection longitudinally with static remote refocusing and the associated deterioration of the resolution and power limitation at different depths. Finally, an attempt is made to probe the action potential properties transmurally along the short axis of the cells at 122 Hz refocusing frequency (Section 6.3). The reader should note that due to limited availability of rabbit heart samples, the data shown in this Chapter is preliminary. Nevertheless, potential improvements in experiment and data analysis are detailed throughout the Chapter. Furthermore, the established analysis protocol is transferable, if more data of better quality is collected.

In this Chapter, all the presented imaging and analysis work is my own.

6.1 Review of published 2PM protocols for cardiac electrophysiology studies

Cardiac action potential properties and their heterogeneity can be investigated with computer models [74], microelectrode arrays [75–78] and optical mapping [56, 79–83]. For a comprehensive review of methods to probe cardiac electrophysiology, the

interested reader should refer to [1].

Microelectrode recordings offer a direct and accurate voltage measurement. However, the insertion of the electrode to the intracellular medium inevitably damages the tissue and confines the measurement to the epicardial cell layers; alternatively, isolated, single-cell preparations are required [1, 3, 75]. Furthermore, it is challenging to maintain the electrode embedded in a contracting cardiac preparation, especially if an arrangement of multiple electrodes is required to visualise the propagating electrical wavefront. Importantly, for the purpose of understanding AP propagation in complex, 3-dimensional tissue volume, the use of such electrodes transmurally within the ventricular wall is difficult. On the contrary, optical mapping with a rudimentary widefield fluorescence microscope (Figure 1.3) allows investigating electrical wavefront change over large scale tissue non-invasively and indirectly, utilising voltage sensitive fluorescent dyes (described in Section 4.1.1). Both topographical and electrophysiological information can be obtained; employing high frame rate CCD or sCMOS cameras allows fast image acquisition. Nevertheless, widefield applications lack optical sectioning. In single-photon fluorescence microscopes, the detected signal is integrated over some tens or hundreds of micrometers under the epicardial surface and it is not possible to differentiate between individual cell layers, prohibiting any transmural AP propagation measurements. Confocal microscopy can be used to discern between different layers along the z axis, but is confined to 30-50 µm range in scattering biological samples [84, 85].

Due to its inherent optical sectioning, robustness to scattering and the ability to achieve cellular resolution in cardiac models closely resembling in-vivo conditions, 2-photon microscopy (detailed in Section 1.1.3) has been used to devise protocols to discern the role of AP heterogeneity and study patho-physiological preparations. Action potential propagation and calcium dynamics in deep layers of intact, Langendorff-perfused mouse, rat and rabbit hearts were investigated [3]; in [58], the efficacy, dynamic range, SNR and cardio-toxicity of Di-4-ANEPPS and FluoVolt VSDs in 2P modality was compared. Additionally, 2PM was also employed to probe AP and calcium wave properties in rat post-myocardial infarction model at different locations with respect to the developed scar [57].

In [3], AP and intracellular calcium traces (CaT) were probed throughout the transmural myocardium in perfused hearts of several species. Di-4-ANEPPs and Fura-2/AM dyes were excited at 920 nm for AP and at 760 nm for CaT, respectively, allowing crosstalk-free sequential recordings. To resolve the rapid depolarisation phase, a line scan of 2.6 kHz sampling frequency (0.382 ms per single line) was facilitated. As the intracellular calcium wave is slower and shallower in its upstroke, lower temporal resolution is needed for CaT recordings (1.93 ms per line; 0.52 kHz sampling frequency).

In both cases, cellular layers throughout the myocardium from 100 µm below the epicardium to 500 µm in steps of 100 µm were probed. For AP recordings, the SNR decreased in the ventricular wall, with their temporal properties in agreement to those from the layers closer to the epicardium [3]. Importantly, while no structural information can be obtained at large depths in tissue due to scattering and absorption, electrical wavefront shape is still resolved by monitoring the change in detected fluorescence intensity with time. The robustness of the protocol is evidenced as for all species (rat, mouse, rabbit) and the duration of the AP trace acquired optically was in close agreement with the microelectrode recordings. Additionally, the AP upstroke durations in rabbit samples were similar: 2.88±0.30 ms measured with 2PM compared to 2.54±0.24 ms measured with the microelectrodes. The limiting aspect of the 2PM protocol was the speed of the galvanometric scan mirror, resulting in upstroke undersampling with 2PM compared to the tenfold faster sampling rate of the microelectrodes. In rodent hearts, the difference in upstroke values was more substantial: 0.50±0.05 ms versus 0.92±0.13 ms in rat and 0.65±0.06 ms versus 1.18±0.23 ms in mouse, respectively [3].

While in [3] the preparations were healthy, in [57], post-MI intact rat hearts were studied with the same protocol. In particular, AP characteristics within and close to the border of the MI fibrosis were compared to those in healthy myocardium as well as to the corresponding results obtained with widefield optical mapping. With the latter, both the non-scarred regions and regions close to the border of the scar showed uniform electrical activity. Conversely, the infarcted zone showed very limited conduction in most areas. Evidently, within the border zone where the healthy cells and the scar intermix across the 3-dimensional tissue volume, widefield measurements confined to the epicardial surface offer only an incomplete picture. 2P line scanning was facilitated to obtain calcium and AP traces up to 500–600 µm below the epicardial surface in distinct cellular planes. In the shallow border zone, fibrotic structures were visible with no AP or CaT observed. However, below 300 µm in depth, electrical function was observed again, suggesting a distribution of healthy cells below the scar. No normal cardiac structures or CaT were observed directly in the infarcted region, however, in certain cellular layers, low amplitude AP traces were recorded, further reinforcing the hypothesis that there is residual electrically active tissue among the MI-induced fibrotic patch. Overall, the average AP upstroke duration was elongated from 2.23 ±0.28 ms in healthy region to 3.50±0.50 ms and 9.13±0.56 ms in the vicinity and directly in the scar region, respectively [57].

Finally, in [58], SNR, dynamic range in various transmural depths in intact mouse heart and toxicity of Fluovolt vs Di-4-ANEPPS were compared using the same protocol, as previously discussed in Section 4.1.1. At 50 µm, the SNR was 9.40±1.06 and at

400 µm, FluoVolt spike signal-to noise was 8.78±3.46.

From the aforementioned studies it is evident that 2P line scanning can offer a more complete picture of electrical conduction in various species, as distinct longitudinal cellular layers of healthy and infarcted myocardium can be probed. The limitations of this method may involve the maximum galvanometric mirror scan frequency. This is especially true for AP measurements, as its upstroke phase is only several milliseconds long. Smaller animal species (e.g. mouse) have shorter APs and undersampling can occur; a ground truth comparison with microelectrode measurement may prove useful. In case of undersampling, CaT recordings can be acquired instead of APs, as the transient is slower. For the case of transmural RF scans, undersampling of the AP upstroke is likely in the physiological conditions. With widefield optical mapping the mean TRise was measured to be 25.9±8.4 ms in room temperature acute rabbit cardiac slices (Section 4.3.5) and upstroke should be resolved by line scanning at 122 Hz.

Interestingly, cellular demarcation lines or any other structural information is not needed to obtain the FluoVolt intensity spikes with high SNR and infer AP properties in deep tissue. In the aforementioned studies, 2PM signals were obtained as deep as 500 µm within the myocardium [3, 57, 58]. Therefore, the entire depth of the myocardial slice can be probed (400 µm). Importantly, compared to the 100 µm optimum RF range for our microscope (Section 3.4), the effects to the SNR due to absorption and scattering should be manageable across this distance.

6.2 AP properties in longitudinal ventricular planes

In the following section, 2P longitudinal line scanning protocol is facilitated and the SNR of FluoVolt spikes at 30-120 µm depth in acute ventricular slices is assessed. This corresponds to the approximate range at which a vertical RF scan will be employed. TRise and AP durations at various degrees of repolarisation are quantified. Remote focusing optics are bypassed in this experiment, as the purpose is to simply validate AP detection with 2P line scanning modality.

6.2.1 2P line scanning protocol

Acute rabbit ventricular slices are prepared according to the protocol in Section 4.2. Viability is verified before 2P imaging by observing contraction of electrically stimulated preparation in room temperature Tyrode's recording solution without BDM under a dissection microscope. The slice is then incubated in Tyrode's recording solution with 30 mM BDM for 10-15 minutes. It is verified under the 2P microscope that the sample remains stationary despite electrical stimulation.

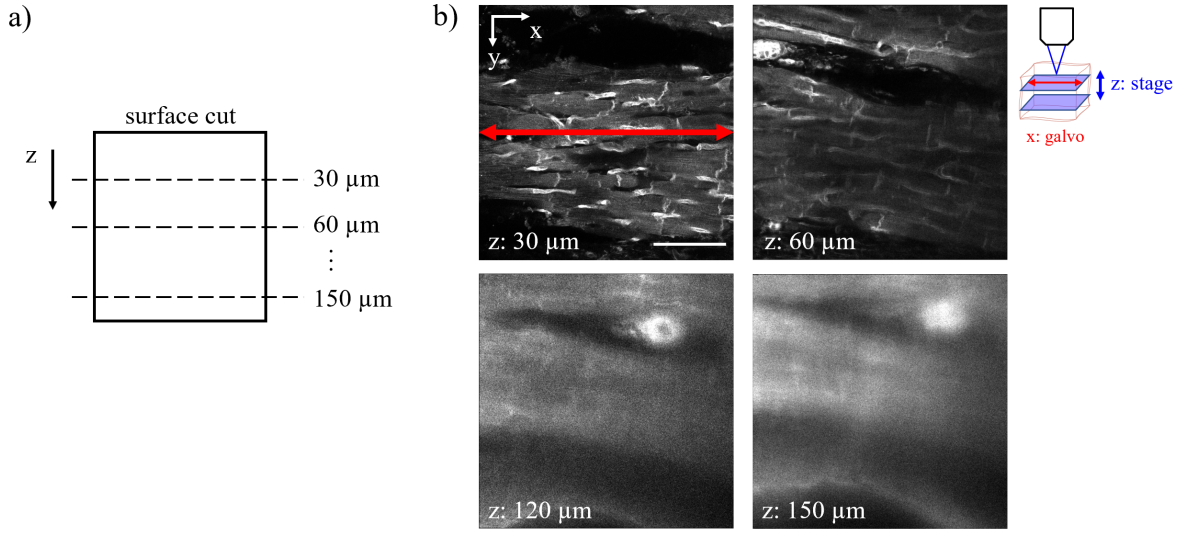

Figure 6.1: Schematic of transmural depths within the slice at which line scanning is facilitated (a). In b), representative x-y frames are shown. Close to the top of the slice, cardiac structure and cell demarcation lines are clearly visible, while in deeper tissue cell borders can no longer be resolved. Scale bar is 200 µm. Red line indicates scanning trajectory of the fast galvanometric mirror.

Live 2D imaging mode is used to find the surface of the cardiac slice and adjust the orientation of the well plate so that the long axis of the cell is approximately along the x galvanometric mirror (fast) scan direction (although it should be noted that the orientation of the cells changes with depth). The positioning is also adjusted so that the x line in the middle of the FOV (700 µm × 700 µm) crosses as much of the brightly stained cellular borders as possible (Figure 6.1b). The y galvanometric mirror (slow) is then unplugged. Line scanning is facilitated along the junctions of 2-3 cells (700 µm range) with a pixel size of 2.74 µm, starting from depths approximately 30 µm below the slice surface to avoid cells damaged by the cut, as shown in Figure 6.1. Each line is obtained in 0.51 ms. Electrical stimulation was set to 2 Hz, 12 ms in duration and 40-50 V amplitude. The latter may be adjusted preparation to preparation as some slices need higher voltage to respond. Scan duration is generally set to 10-15 s, as that allows recording a sufficient number of individual APs to average over. Longer exposure times are avoided due to possibility of tissue damage. The reader should note that the experiment was carried out before it was established with CellOPTIQ system that 1 Hz should be the maximum pacing frequency and that the AP trace of hypothermic slices becomes chaotic in room temperature at 2 Hz (Section 4.3.7). The irregular 2P traces shown in this chapter were the motivation for the quality assessment study in the aforementioned section.

Background-subtracted frames are rotated and concatenated appropriately in MATLAB to form a time lapse (Figures 6.2a and 6.3a). The average value of each column

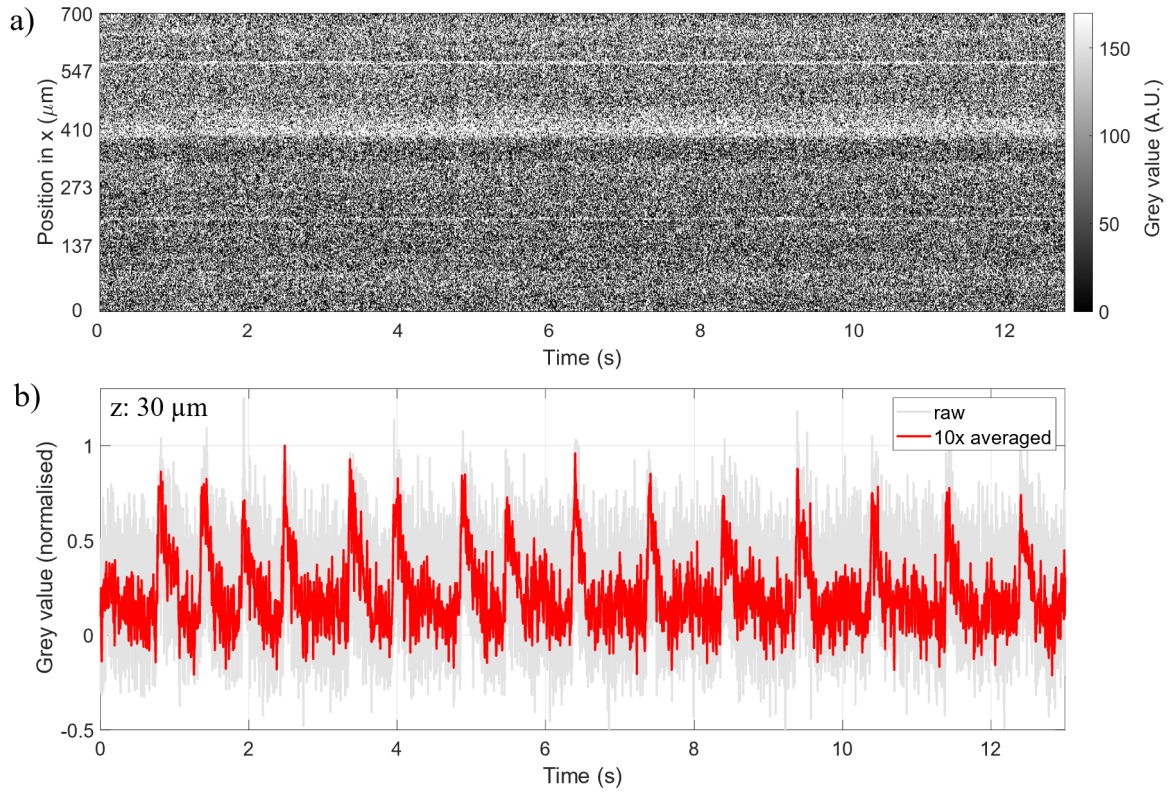

Figure 6.2: Longitudinal line scanning across cardiac cells to visualise APs z=30 µm. In a), a 25600 line timelapse is shown (13.1 s; 0.51 ms per line). Contrast is adjusted (intensity values are thresholded to limits in the colourbar). Faint intensity increase is visible in the time lapse corresponding to FluoVolt spiking. In b), raw trace is displayed in light gray while. Each data point in the trace corresponds to the average of one column in the time-lapse in a).

The red trace corresponds to $\times 10$ time binning of the raw trace.

is calculated (0.51 ms sampling, light gray traces in Figures 6.2b and 6.3b). To reduce the effect of the noise, time binning of 10 columns is performed (5.1 ms per data point). The mean value of TRise was measured to be approximately 25.9±8.4 ms and 13.95±1.63 ms in slices from two different hearts with the CellOPTIQ system (Section 4.3.5). As per Nyquist sampling theorem, the time binning chosen is sufficient to resolve AP upstroke for both of these durations. The time-binned AP traces at 30 µm and 120 µm depths are shown in Figures 6.2b and 6.3b in red and blue, respectively. While the structural features of the myocardium are almost completely blurred at a depth of 120 µm below the slice cut (exemplified by a lack of features in the time lapse of Figure 6.3a compared to 6.2a), both AP traces acquired have a comparable SNR. This agrees with [3, 57, 58], where signals were obtained from deep myocardium with no structures resolved. The spiking in AP trace is irregular and some beats are missed (e.g. after 6 s in Figure 6.2b). This is because, as discussed in Section 4.3.7, slices kept in room temperature cannot cope with 2 Hz pacing. Due to limited heart sample

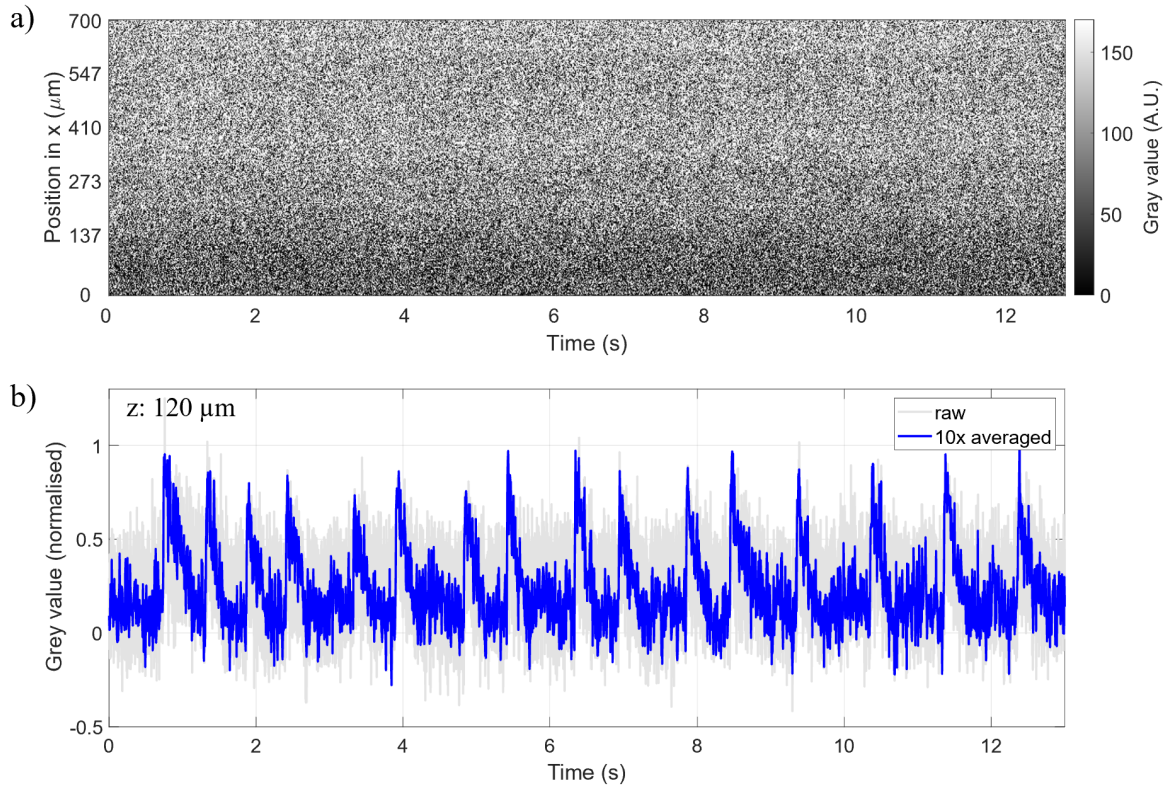

Figure 6.3: Longitudinal line scanning across cardiac cells to visualise APs at z=120 µm. In a), a 25600 line timelapse is shown (13.1 s; 0.51 ms per line). Contrast is adjusted (intensity values are thresholded to limits in the colourbar). Faint intensity increase is visible in the time lapse corresponding to FluoVolt spiking. In b), raw trace is displayed in light gray. Each data point in the trace corresponds to the average of one column in the time-lapse in a).
The red trace corresponds to ×10 time binning.

availability only the preliminary data was obtained. Nevertheless, SNR can still be quantified.

To evaluate the SNR and action potential properties (TRise and APD), a similar protocol to that in CellOPTIQ (Section 4.3.5) is utilised. A gradient of the time-binned and smoothed (MATLAB's smoothdata() function) trace is taken. Using the findpeaks() function, locations of most prominent derivative change, corresponding to the rapid upstroke are identified. An appropriate degree of smoothing before derivative as well as function parameters such as 'MinPeakProminence' and 'MinPeakDistance' allow accurate identification of upstroke locations and exclusion of gradient peaks resulting from noise. The individual APs in the un-smoothed trace are then averaged (Figure 6.4). It should be noted that the irregularity of traces with 2 Hz pacing may contribute to errors in aligning the individual APs for averaging.

SNR as well as signal-to-background ratio (SBR) can be calculated for the average AP profiles. SNR is defined as

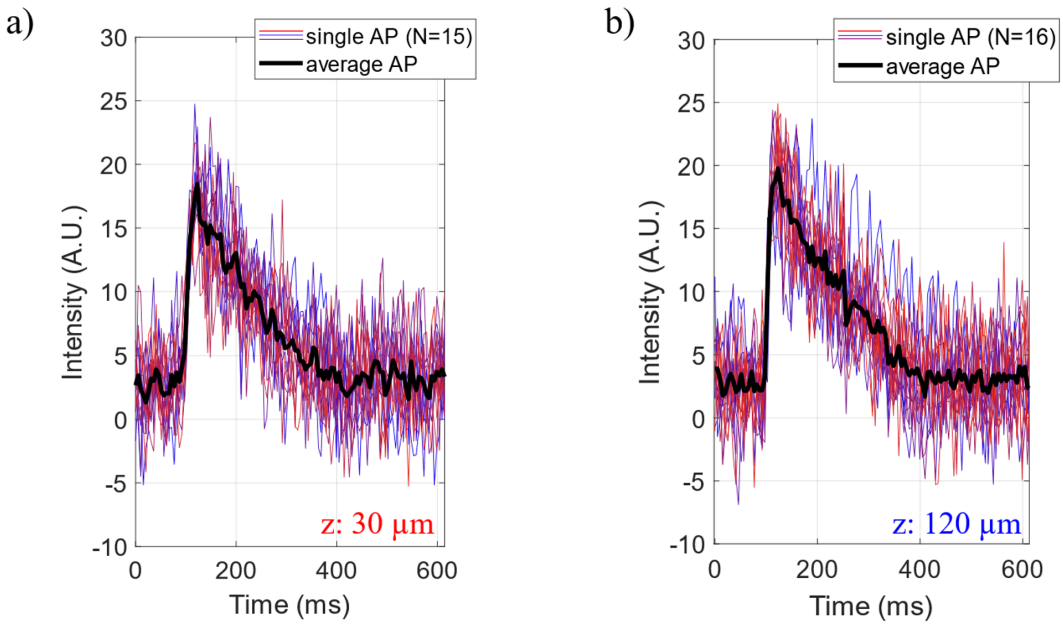

Figure 6.4: Average APs (black) at a) 30 µm and b) 120 µm depth in tissue. The thin lines in colour gradient from blue to red denote individual action potentials identified from the traces in Figures 6.2b and 6.3b.

$$\mathrm{SNR} = \frac{\mathrm{I_{Peak}} - \mathrm{mean_{Bg}}}{\Delta\mathrm{noise}}. \tag{6.1}$$

SBR, on the other hand, is simply $\frac{I_{Peak}}{mean_{Bg}}$. Here, $mean_{Bg}$ is mean background, I_{Peak} is peak intensity and $\Delta noise$ is magnitude of noise band. The noise band $\Delta noise$ is chosen to be $\pm\sigma$ (region enclosed by dashed blue lines in Figure 6.5). Additionally, in Figure 6.5, the peak intensity of the average AP is marked in red while the mean noise (or mean diastolic signal, obtained from the grey regions bounded by the intersection of the smoothed trace with the mean background) is shown in solid blue line. The corresponding SNR and SBR values for average APs at different depths (Figure 6.6a) are shown in Figure 6.6b and 6.6c, respectively.

To calculate APDs and TRise, the average AP trace was divided into two phases - upstroke, on the left of the peak intensity and downstroke, on the right of the peak. As the average AP is noisy, smoothing is necessary. The fast depolarisation and slow repolarisation processes are filtered separately. The filtering parameters and protocol routinely used in the CellOPTIQ system's (Section 4.3.5) software was utilised. An example of an average AP trace is shown in Figure 6.5 (black trace). AP duration values at different stages of repolarisation (using the same definition as in Section 4.3.5) are then inferred from the intersections of horizontal lines with this smoothed trace. In particular, APD90, APD75 and APD50 correspond to the solid, dashed and dotted magenta lines in Figure 6.5, respectively. TRise is calculated from the top of the

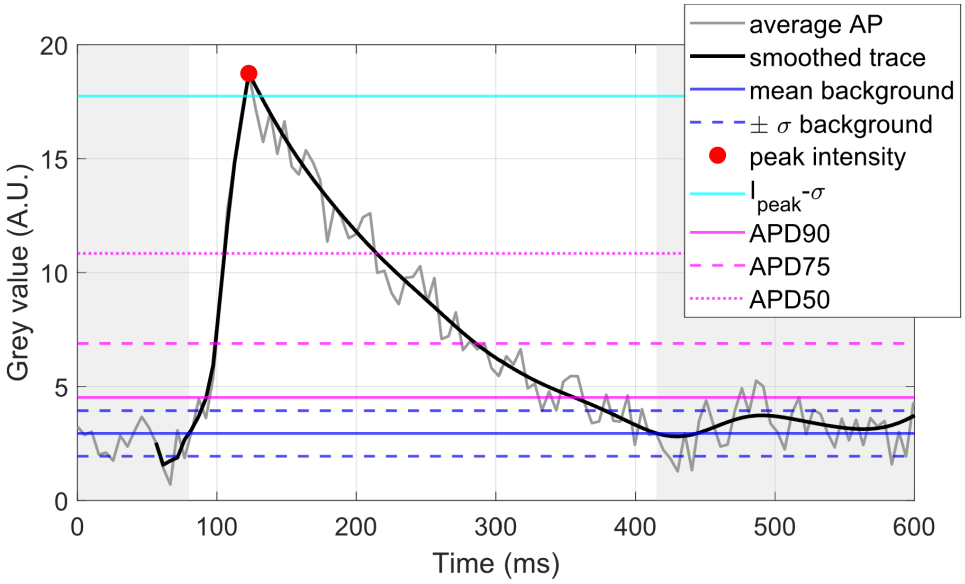

Figure 6.5: Relevant quantities for analysis of the average AP profile.

noise band to $I_{Peak} - \sigma$. The upstroke rise times and AP durations at various degrees of repolarisation are shown in Figure 6.7.

6.2.2 Results

The average APs retain a similar shape throughout the depth of the slice and the SNR increases from 7.46±1.41 at 60 µm to 10.74±1.02 at 120 µm. The SNR increase with depth is because the excitation power was increased with depth (by adjusting the Pockels cell bias by 1%). At shallow depths within the myocardium, this more than compensates for losses due to scattering and the SNR, which is encouraging for potential 2P-RF experiments. This agrees with [58], where FluoVolt AP SNR was found to change minimally even in larger depths (at 50 µm, the SNR was 9.40±1.06 and at 400 µm, FluoVolt spike signal-to-noise was 8.78±3.46) and power at sample was increased during the scan. Evidently, the SNR values are also in a similar range to those reported in [58]. These cannot be directly compared due to differences in animal model (mouse vs. rabbit) as well as the microscope. Nevertheless, it should be noted that the experimental parameters are similar (excitation λ=840 nm vs. λ=800 nm with the same objective). Additionally, in our study the heart is re-used after another experiment and sliced. Therefore, FluoVolt loading takes place several hours before the 2P experiment. This further reinforces that the SNRs obtained in the preliminary AP traces are satisfactory. Signal-to-background ratio remains almost constant with a slight increase throughout the depths of 30 µm to 120 µm (Figure 6.6).

As in Figure 6.7, the mean TRise is calculated to be 31.05±6.42 ms (sigma is 20.66% of mean). The mean APD90, APD75 and APD50 values are 262.91±18.1 ms,

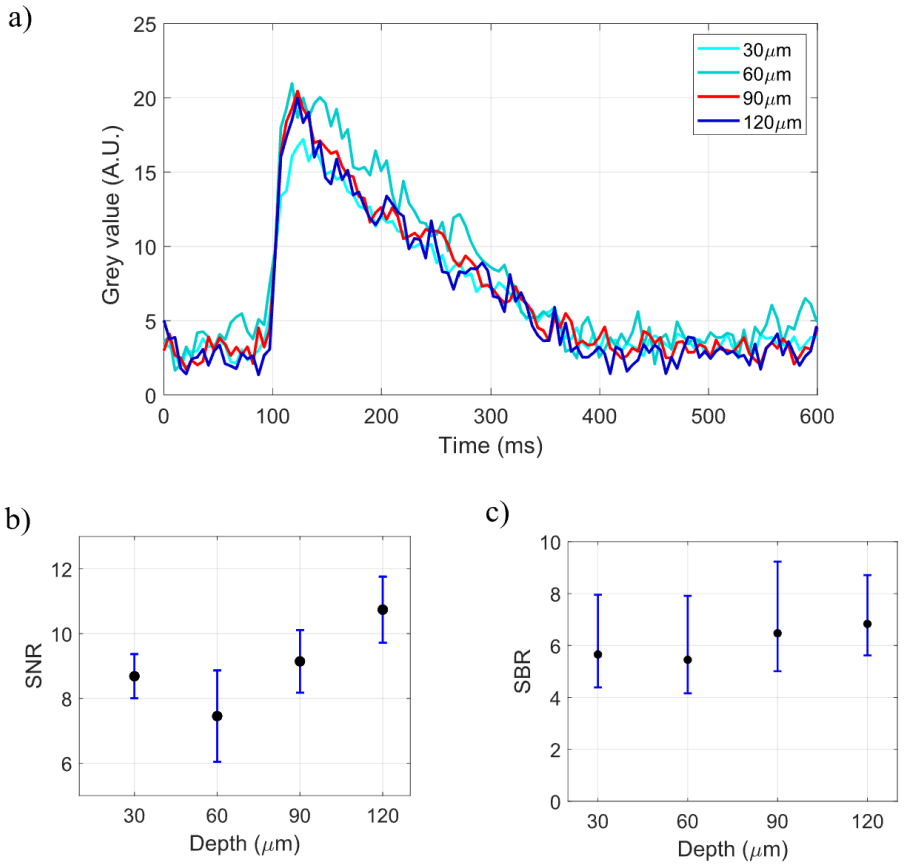

Figure 6.6: Average APs (a) and the corresponding SNR (b) and SBR (c) of conventional 2P traces at different depths within the slice. Note that raw intensity values are plotted, meaning deeper layers may appear to have reduced AP amplitudes due to depth-dependent scattering losses. The uncertainty in SNR values is $\pm\sigma$ of values from different line scans acquired within the corresponding depth. The uncertainty in SBR is due to division of peak amplitude by the lower and upper bounds of the noise floor.

202.69±15.85 and 112.5±12.21 ms, respectively; the standard deviations make 6.88%, 7.82% and 10.85% of the means, respectively. As the pacing was set to 2 Hz and the traces were chaotic (Figure 6.3) these results cannot be compared to those in Section 4.3.5 with confidence, where TRise and the corresponding APDs were determined with optical mapping in slices stimulated at 1 Hz. Nevertheless, as shown in Figure 4.14c, the mean APD50, APD75 and APD90 values were measured to be 99.46±22.51 ms, 184.65±38.91 ms and 259.88±60.26 ms for the first experiment, respectively. These results are close to those obtained with the 2P line scanning protocol: the differences between APD50, APD75 and APD90 are 13.04ms, 18.04 and 3.03ms, respectively. While this agreement is promising, the aforementioned quantities were approximately by a factor of two longer in optically mapped slices in the second slicing session (Figure 4.14c). The long TRise value obtained with 2P line scanning could have occurred due to discrepancies in identification of upstroke in chaotic line scanned traces. Overall, more

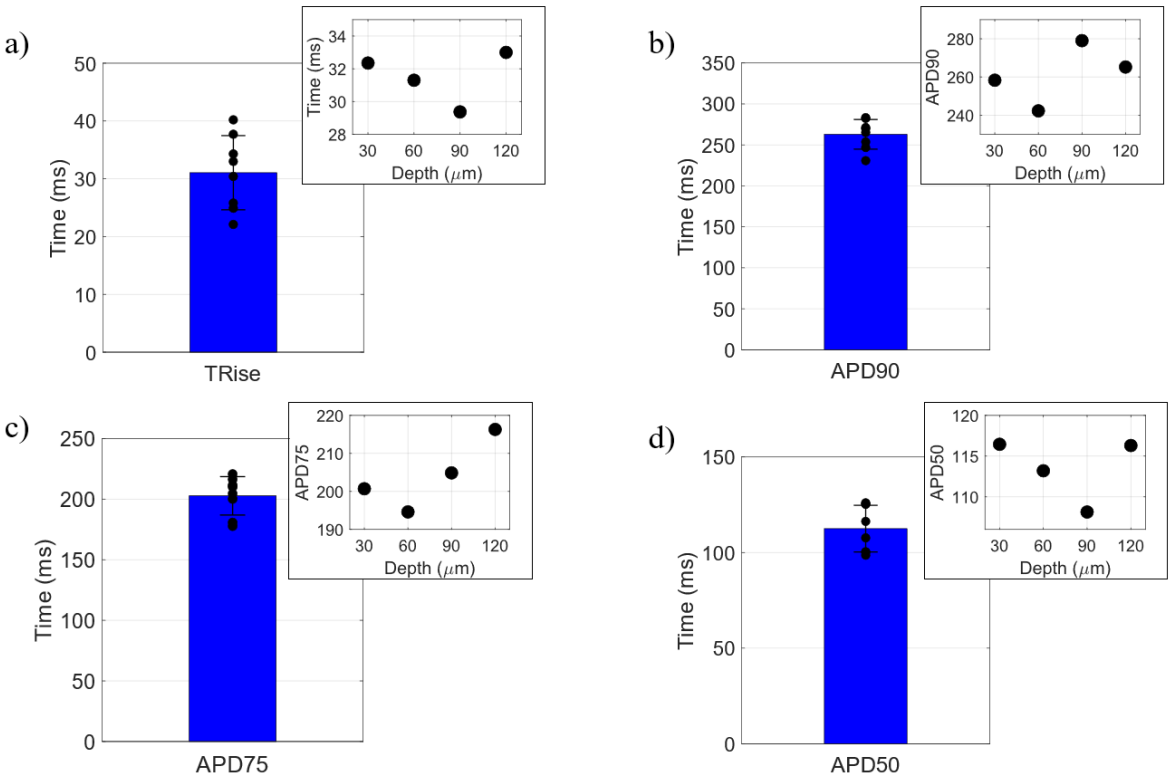

Figure 6.7: TRise (a) and APD90 (b), APD75 (c) and APD50 (d) values obtained from 2P longitudinal line scans at different depths. Upper right graphs show change of the aforementioned quantities with depth.

experiments at appropriate stimulation frequency need to be carried out with both 2P line scanning and CellOPTIQ optical mapping to establish whether measurements with the two modalities agree. In Figure 6.7, the upper right graphs show the change of the corresponding quantities in depth. Currently, no trends can be hypothesised due to the variability of the results, although more experiments and probing a larger depth within the sample would allow verifying that APDs and TRise are constant with changing depth (as established in [58]).

6.3 Towards resolving AP properties transmurally with Remote Focusing

The following section discusses attempts to incorporate RF optics in AP imaging.

6.3.1 Static remote focusing with fast longitudinal scanning

In Section 6.2, RF module optics were bypassed and imaging was not affected by the resolution degradation with refocusing (detailed in Section 3.4) nor the limitations in power (Section 3.5). To verify that APs can still be visualised under the aforementioned

conditions, static remote refocusing to different depths was facilitated and longitudinal line traces were obtained with the fast galvo mirror using the protocol described in Section 6.2.1. The traces are shown in Figure 6.8. The design focal plane of the system (0 µm refocus) was approximately at the first intact cellular layer below the sample surface cut. While at −30 µm refocus (negative direction points out of the sample) there is no signal, refocusing deeper in the slice (30 µm) in the slice allows visualising FluoVolt spikes. To further quantify the SNR and SBR of the preliminary data, the same method was applied as described in Section 6.2.1, with results shown in Figure 6.9.

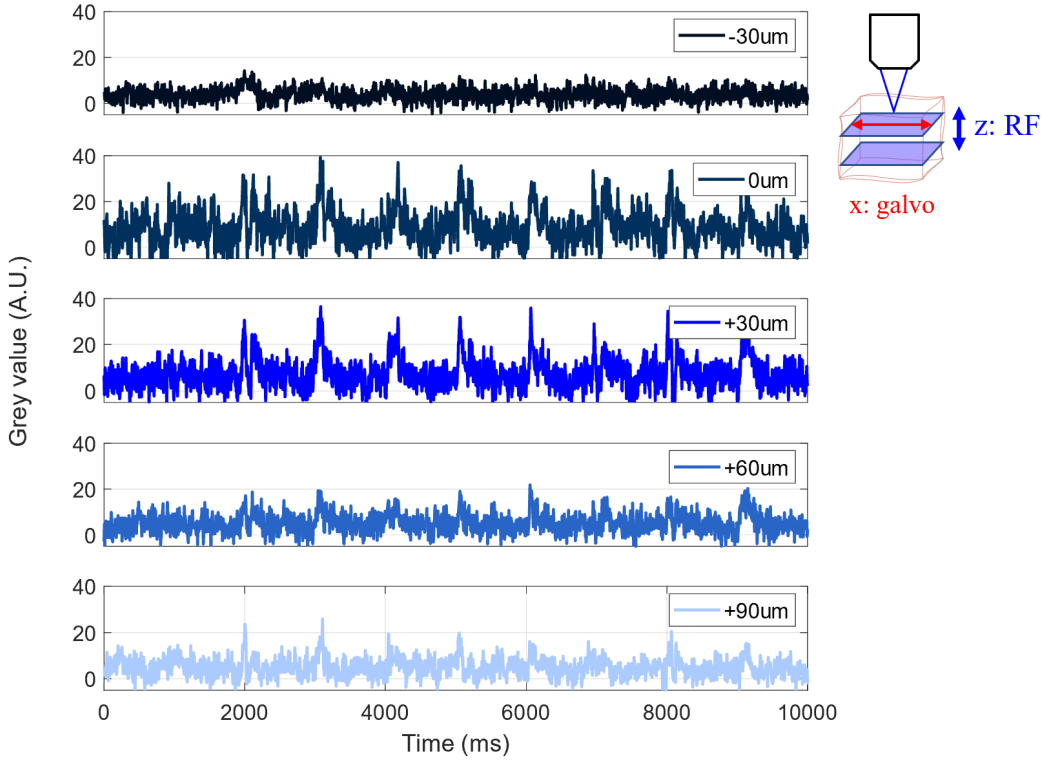

Figure 6.8: AP traces obtained by longitudinal galvanometric mirror line scanning (x) where static refocusing to different depths in tissue (z) was facilitated with the RF module. Galvanometric mirror scanning was facilitated at, 0.51 ms per line, ×10 time binning is applied in the traces shown (5.1 ms per data point). Some signal appears at refocusing of 0 µm. At 90 µm refocus the signal is almost completely diminished, albeit with appropriate smoothing or averaging with respect to the pacing cycle the trace could potentially be recovered.

From Figure 6.8 it can be seen that the sample was not positioned optimally - the position where the RF mirror is in the focal plane of the remote objective should have coincided with a plane deeper in tissue. It would likely also allow resolving APs over the 0 µm to −60 µm range, yielding a total distance of around 120 µm over which APs are visible with static RF. As in Figure 6.9b, the SNR is decreasing quite significantly from 7.57 at 30 µm to 3.09 at 90 µm, irrespective of increased power allowed by the Pockels

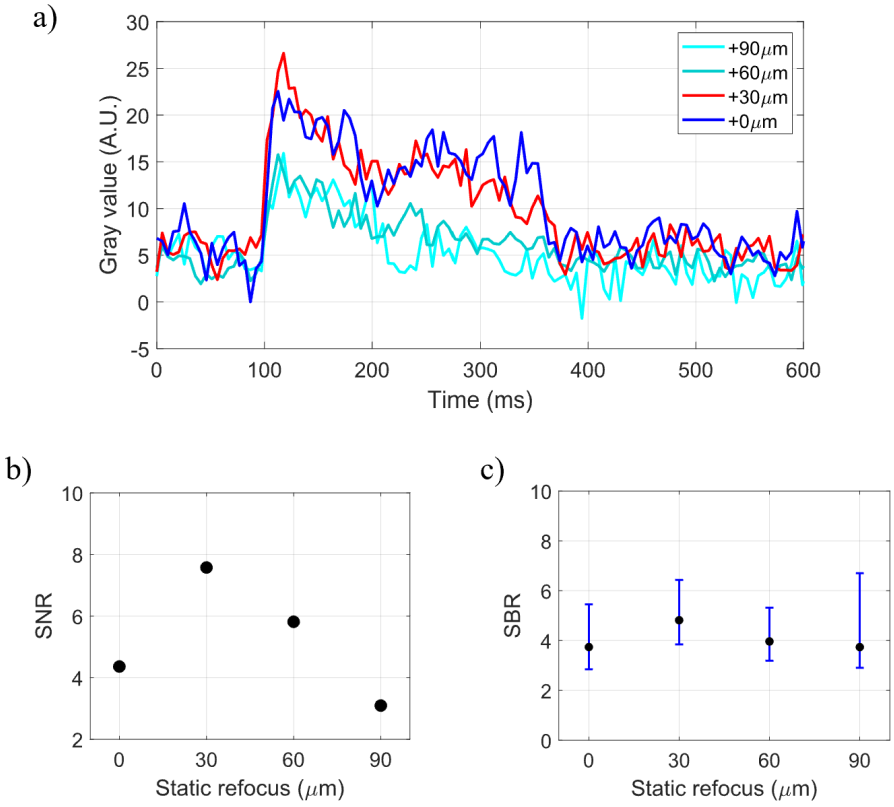

Figure 6.9: Average APs (a) and the corresponding SNR (b) and SBR (c) of 2P line scans obtained at different statically remote refocused depths. The uncertainty in SNR values is not quantified as only one trace per depth was acquired in the experiment. The uncertainty in SBR is due to division of peak amplitude by the lower and upper bounds of the noise floor.

cell. This could have been due to the degradation of resolution through the RF range, which was detailed in Section 3.4, but is expected to be more pronounced in tissue where the refractive index differs from that of water (for which RF system is optimised) and is heterogenous. Additionally, higher order spherical aberration could have contributed to this effect at larger extents of refocusing. If the sample was repositioned so that the nominal mirror position was deeper in the tissue, refocusing in both positive and negative directions with respect to the nominal mirror position could have been utilised instead of only using the positive direction to refocus the same range, which incurs more higher order aberrations deteriorating the SNR. Furthermore, the maximum power allowed before the RF mirror is etched at each position should be established and used to improve the SNR of traces. Nevertheless, this preliminary result verifies that even with the power and resolution limitations imposed by the RF module, APs can be resolved in highly scattering cardiac tissue. Note that as in the case for simple 2P line scanning. the SBR stayed approximately constant with RF depth (Figure 6.9c).

6.3.2 Fast transmural RF line scan

As action potentials could be resolved with static refocusing, preliminary attempts at fast transmural RF line scanning were made, as shown in Figure 6.10. Currently, averaged traces show no FluoVolt spikes. The scan amplitude was in the range of z=155.44 µm, with a single line scanned in 4.1 ms. A representative time lapse (Figure 6.10a) and an averaged intensity trace (Figure 6.10b) with ×5 time binning (20.5 ms per datapoint) are displayed. This time binning was chosen despite the undersampling of AP features such as the upstroke rise time in order to see if any FluoVolt spikes can be visualised. Nevertheless, the scan currently yields a negative result and only noise is visible in the trace.

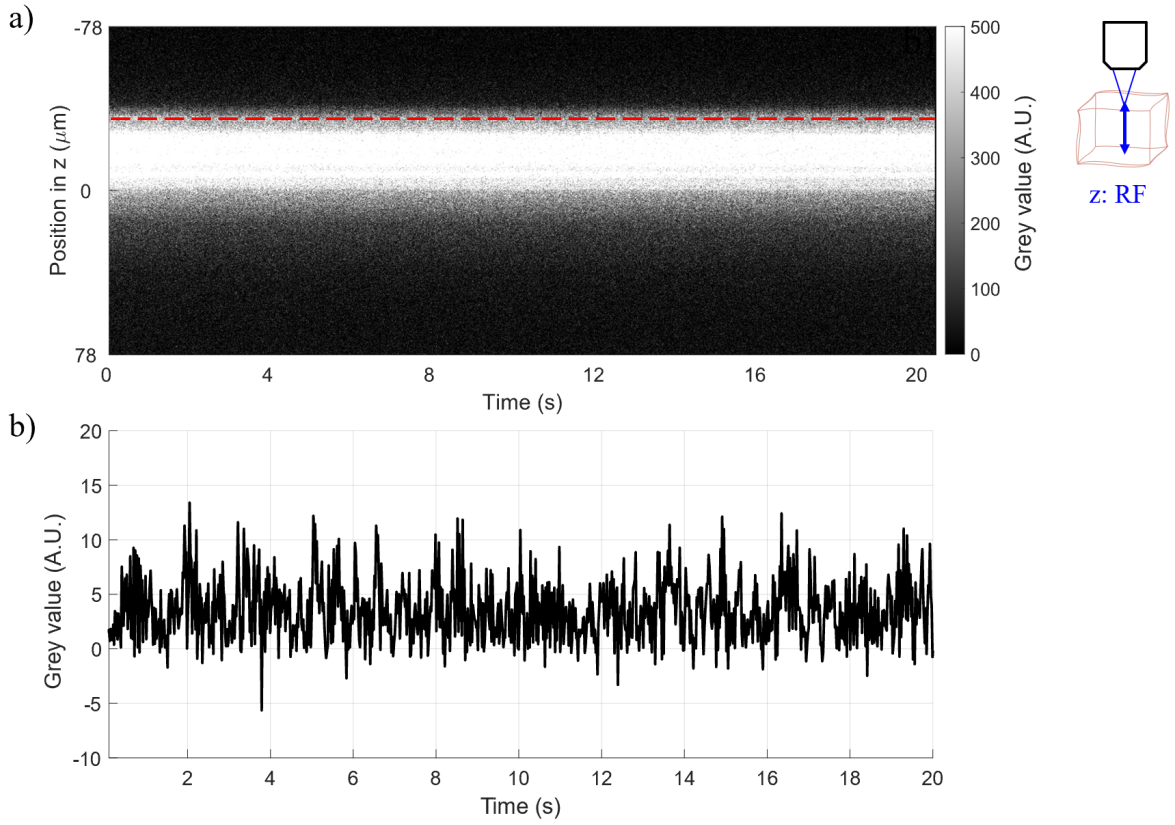

Figure 6.10: 122 Hz transmural RF scan in electrically stimulated slice. The timelapse is shown in a. Red dashed line indicates slice surface. The color bar indicates gray values (a.u.). In b, an averaged, ×5 time-binned intensity trace is shown. No AP features can be discerned through the noise; this is also true if narrower z range (excluding regions outside the slice) is chosen for averaging. Compared to the gray values in the colourbar, the averaged trace counts are in the range from 0-15, because of the baseline subtraction (facilitated with MATLAB's msbackadj() function) to account for the fluorescence bleaching.

Multiple adjustments will be considered in order to resolve FluoVolt spikes in the transmural RF trace in future experiments.

Firstly, it is imperative that the sample is repositioned so that the nominal RF mirror position corresponds to deeper tissue layers and area outside the slice as well as that the cell layer within the sample surface is omitted from the scan. In the attempt in Figure 6.10a, z=0 µm is close to the tissue surface (approximately 30 µm to the dashed red line) where the cardiomyocytes are likely damaged by the surface cut. Additionally, approximately 50 µm of the scan is outside of the slice. Therefore, the entire negative refocusing range of the scan is not in regions where AP is propagating and is not contributing to the detected Fluovolt intensity change. Furthermore, as the optical recording is noisy, the aforementioned is likely to impair the averaging the lines and further drown out any residual FluoVolt signal.

Secondly, in addition to better sample positioning, a larger scan amplitude should be chosen. In the longitudinal scans (for example, Figure 6.2 and 6.8), the distance traversed in x was 700 µm. This potentially allows more pixels to overlap with the brightly stained cell membranes and gap junctions connecting the cardiomyocytes. As these regions are primarily responsible for cell-to-cell electrical signaling, traversing more of these areas within the line scan could increase the SNR of detected APs. Nevertheless, in RF scans, the approximate amplitude of 100 to 200 µm could mean that fewer regions of the cardiac cell membrane are imaged. This is especially true for the attempted scan in Figure 6.10, as only half of the refocusing range was in the region of the tissue where APs propagate, further reducing the likelihood of refocusing through the cellular membrane. Additionally, it could be beneficial to image the Z-Y planes and visualise tissue structure prior to the line scan. As was shown in Chapter 5, brightly stained cell membranes are resolved with RF module. Although the cells in Figure 5.1 are very close to the slice surface and may be damaged by the cut, imaging Z-Y planes deeper and detecting brighter regions, even if almost entirely blurred, could increase the chance of traversing cell membrane in the transmural scan. This check, if proved beneficial, could also be facilitated with traditional z-stack scan (not subject to RF resolution degradation), as although blurred, brighter regions corresponding to cell membranes can be identified as deep as 120-150 µm in tissue (Figure 6.1b). The sample could then be positioned to ensure that the bright region overlaps approximately within the transmural scan trajectory.

Furthermore, to acquire more signal at each refocused position, optical integration could be performed. A conical shaped lens or axicon (AX255M-B, Thorlabs) can be incorporated within the optical system to generate a Bessel beam [86]. Alongside their self-healing properties, Bessel beams have a bright central core that is not subject to diffraction effects. A pattern of cocentric rings surround this core, with their intensity decreasing towards the edges of the beam. Importantly, when focused, Bessel beams exhibit a significantly elongated depth of focus (DOF) compared to Gaussian

beams, while maintaining a relatively high intensity along this extended focal region. Therefore, they have applications in microscopy where extension of the useful DOF is beneficial [87]. The elongated sharp DOF could allow the signal detected at each refocusing position be a sum of signal over the extended DOF, potentially enhancing the 2P-RF system's capability to detect FluoVolt spikes. Nevertheless, optical losses associated with the introduction of the axicon lens should be considered.

Furthermore, a power modulation gradient could be applied on the Pockels cell (Model 350-80, Conoptics) as the voltage bias across the crystal can be changed rapidly and device response time is significantly faster than remote refocusing frequency. Currently, the power when the remote mirror is positioned in focus is just below its etching threshold and this power level is maintained constant throughout the scan. Nevertheless, at defocused remote mirror positions, lower power density is incident onto the mirror surface, allowing increasingly larger average power at sample than the 22 mW limit at z=0 µm. A power modulation gradient would allow gradually increasing the power when approaching the positive and negative extrema of the refocusing range so that it either stays just below the mirror etching threshold or, if that exceeds the tissue damage threshold, the power should be increased so that it doesn't exceed tissue-safe levels. This would require to measure the powers at which the mirror is etched at different degrees of refocusing and also establishing an average power level at sample which does not affect tissue viability and function. Alternatively, a method similar to that in [47] could be used where the coverslip required by the remote objective is moved from the remote arm to the imaging arm (the symmetry of RF systems implies preserved resolution at the sample objective). This results in worsening the resolution of the focal spot at the remote mirror and in turn decreasing the incident power density, allowing more average power at sample before remote mirror is etched.

Finally, Cal520 (AAT Bioquest) dye could be used to probe the slower calcium wave (Section 2.2.1) within the slice tissue. In the hands of our collaborators, Cal520 was found to be approximately 10 times brighter than FluoVolt under similar experimental conditions [88]. Moreover, slower electro-physiological dynamics would allow increasing the pixel dwell time (and reducing the scan speed) to collect more signal. The reader should note that despite these benefits, Cal520 was not tested as the hearts from our colaborators are always pre-stained with FluoVolt for their experiments. The fluorescence emission range of FluoVolt overlaps with that of Cal520. Therefore, Cal520 cannot be utilised if the FluoVolt loaded hearts were to be re-used (in accordance with the University's strategy for mitigation of animal research [11]). Other variants of calcium reporters are incompatible with the optical losses of RF module (Section 3.5), as the tunable Chameleon laser power decreases towards longer wavelengths. Furthermore, the objectives used in the system have reduced transmission at longer

wavelengths. If even after the aforementioned optimisation strategies are implemented, RF transmural scans yield a negative result in FluoVolt stained tissue, we will opt for Cal520 staining in hearts from animals dedicated for this experiment.

6.4 Summary

FluoVolt intensity change allows visualising APs in longitudinal planes throughout the slice with 2PM modality of our system, when line scanning is facilitated with the fast galvanometric mirror (0.51 ms/line over 700 µm) (Section 6.2.1). When RF optics were included in the beam path, FluoVolt spiking was recorded over a range of approximately 90 µm with static remote refocusing (Figure 6.8). Here, longitudinal galvanometric mirror line scanning was facilitated at 0.51 ms/line during which the voice coil actuator was stationary, however, RF optics are used to switch from one lateral plane to the next (z refocusing). Including RF optics as well as remote refocusing introduces power limitations (Section 3.5) and aberrations (degradation in resolution with refocusing is detailed in Section 3.4, although it is expected to be more pronounced in cardiac tissue due to the refractive index heterogeneity). The 90 µm range could be further extended by better sample positioning, as traces from 30 µm in Figure 6.8 were likely obtained from cells damaged by the surface cut of the slice. Fast RF line scanning at 122 Hz throughout the sample currently yields a negative result (Figure 6.10), potentially because a cell demarcation line where most of the FluoVolt is concentrated was missed. Because static RF refocusing still allows detection of longitudinal APs with the resulting deterioration of resolution and power limitation (albeit at a larger scan range that covers more cellular demarcation lines: 700 µm instead of approx. 100 µm in tissue in the case of RF), we believe that with further optimisation strategies discussed in Section 6.3.2 the 2P-RF microscope will be able to resolve transmural ventricular APs.

Chapter 7

Outlook and conclusion

The 2P-RF system developed and characterised (Chapter 3) managed to achieve fast transmural cardiac structure imaging (Chapter 5). During functional imaging, longitudinal APs were still resolved (albeit at a lower SNR) with static remote refocusing, although the rapid transmural scan currently yields a negative result (Chapter 6). Regarding sample preparation, we have successfully established a protocol to produce, mount and electrically stimulate acute rabbit ventricular slices from re-used hearts at room temperature and assessed their viability and electro-mechanical properties (Chapter 4). Provided the optimisation detailed in Section 6.3.2 allows resolving acute slice AP traces with remote refocusing, the following Chapter discusses potential improvements of the 2P-RF method in this context. Importantly, the potential method and feasibility for preparation of acute cardiac slices under physiological conditions is detailed, considering how the 2P-RF microscope could be made compatible with imaging these preparations of physiological relevance in terms of enhanced speed and sufficient SNR. Finally, a strategy of functional-structural correlative imaging is proposed, where the electrophysiological 2P-RF data from post-myocardial infarction slices could be used to infer arrhythmogenic pathways resulting from chaotic scar microstructures, uncovered within the same slices by optical clearing and mesoSPIM light sheet microscopy.

7.1 2P-RF microscope to follow the AP under physiological conditions

Two key aspects of the experiment need to be modified to allow 2P-RF imaging under physiological conditions: the microscope system itself and the acute cardiac slice preparation and maintenance.

7.1.1 Acute cardiac slice preparation and maintenance under physiological conditions

Chapter 4 detailed acute rabbit cardiac slice preparation and maintenance in room temperature. The choice to keep the slices "cold" was made to reduce the cardiac conduction velocity and prolong the AP in order to ease the imaging for proof-of-concept trials of the 2P-RF system, discussed in Chapter 6. Furthermore, the complexity of the system was reduced as neither heating nor oxygenation is is required for room temperature preparations.

Nevertheless, slices kept under physiological conditions hold a much stronger promise for informative and relevant electrophysiological data; the results of such experiments could translate to clinical studies, drug testing or organoid-myocardium electromechanical coupling assays. To ensure this, the cardiac slices need to be warmed up from room temperature to 37 °C. This can be done in an incubator chamber (Okolabs, Bold Line Top Stage Incubator) where the humidity as well as oxygenetation need to also be controlled. This, however, would require an inverted microscope set-up to accommodate an enclosed incubator. Alternatively, a sample chamber with a heating plate to warm up the Tyrode's solution fully submerging the slice would provide a more straightforward solution. The solution needs to be recirculated and oxygenated with medical grade oxygen; bubbling the sample bath directly will cause motion artifacts. The bubbling should therefore take place in a separate chamber and the flow of the oxygenated solution to the bath should be very slow. A peristaltic pump could be used to recirculate the solution at the optimal flow rate (e.g. Gilson MiniPuls 3 Pump). It is important to consider that with the increase in temperature, the metabolic needs of the sample will also increase and maintaining viability will require more rigorous control of experimental conditions.

Furthermore, the slices will denature if no tension is applied, which will in turn affect their electrical properties. For rabbit preparations, the slices should be stretched so that their resulting sarcomere spacing is 2.2 µm.

7.1.2 Pushing the capabilities of the 2P RF approach

When heated to 37 °C the APD will shorten to roughly 200 ms for rabbit preparations and the cardiac conduction velocity will increase (75 cm/s and 25 cm/s longitudinally and transmurally, respectively) when compared to room temperature. Consequently, this will significantly increase the refocusing speed and SNR requirements of the 2P-RF microscope in order to resolve the AP.

To keep up with the increased cardiac conduction velocity, a faster voice coil actuator will be needed (due to the -3 dB point of our device being at around 250 Hz, as

discussed in Section 3.7.2). A model used in [43], namely Rapp Optoelectronic GLP-V1, could be used as it supported up to 1 kHz and 0.5 kHz scanning for 50 µm and 150 µm refocusing range, respectively. It should be noted that the refocusing distance will correspond to physical translation of the voice coil differently based on the optics used; however, it is evident that faster devices are available. Resonant VC systems can go faster, however they are bound to a given frequency and the precision of motion can be compromised due to the lack of feedback. Making a custom actuator as was done in [6] would complicate the set up although would potentially allow precise higher frequency scanning, but require extensive engineering expertise and complex characterisation to ensure stability of motion.

With increasing refocusing speed, the SNR of 2P-RF scans will decrease, which is likely to be a fundamental limitation when imaging highly scattering cardiac tissue under physiological conditions. Additionally, the axial distance scanned with the RF module (1.1) is smaller than the distance of the galvanometric mirror line scan facilitated across longitudinal planes (100-200 µm versus 700 µm, respectively). As a result, more regions corresponding to cellular membranes are likely scanned across in longitudinal planes, potentially increasing the FluoVolt signal collected. Furthermore, SNR becomes particularly concerning when the power limitations discussed in Section 3.5 are considered. Remote focusing is most prominently facilitated before the lateral scanning units in multiphoton fluorescence excitation path [39, 41, 42]. However, placing it after the galvanometric mirrors would reduce the number of optical surfaces between the remote and sample objectives, thus allowing more average power at the sample. The deviation of the beam from the optical axis is likely to reduce the imaging quality across the FOV. However, if a lens that is well-corrected off-axis is used for RF, this effect will be mitigated. Additionally, a high NA aspheric lens could be used instead of a microscope objective, which, with the correct anti-reflection coating would have over 95 % transmission efficiency as opposed to a much lower one yielded by objective lenses. This would aid in ensuring there is sufficient average power at the sample. Alternatively, the method proposed in [47] could be used where the coverslip is moved from the remote arm to the imaging arm, thus reducing the resolution of the focal spot at the remote mirror and in turn the incident power density. Finally, a brighter Cal-520 AM (AAT Bioquest) dye to probe a slower calcium wave within the slices could be employed to mitigate both the SNR and the speed requirements. In the hands of our collaborators, Cal520 was found to be approximately 10 times brighter than FluoVolt under similar experimental conditions [88].

7.2 Post-myocardial infarction slice electrophysiology assessment

In addition to investigating cardiac preparations under physiological conditions, probing the electrical signal propagation of pathological preparations can provide crucial insights into arrhythmia formation. A significant cause of mortality occurring post MI is arrhythmia [89]. The scar that forms after the myocardial infarction is not homogenous or uniform; the districution of the fibrotic microstructure is often chaotic and complex with areas of healthy cardiac cells intermixing with the scar (Figure 7.1). The heart as a whole is incredibly capable of finding and establishing new electrical conduction pathways in presence of obstructions. Due to the complexity of the scar geometry, these border zones are particularly prone to arrythmias as these new conduction pathways develop. The fibrosis and abnormal repolarization gradients within the region create a substrate for re-entry arrhythmia, which is a persistent, re-occurring closed-loop abnormality in the heart's rhythm. Unlike the natural healthy propagation from the Sinoatrial node to the ventricles, in the case of re-entry arrythmias the heart's electrical network does not pause and move on as it should, but instead loops back around within the region and stimulates the atria or ventricles repeatedly.

Ventricular slices prepared from hearts that undergo myocardial infarction could reveal how the action potential properties are altered by the fibrotic scar, especially in the border zone where healthy myocytes and scar tissue intermix. In the New Zealand White rabbit model, the myocardial infarction can be induced by percutaneous coronary occlusion through microcatheter tip deployment or coronary ligation, with the former yielding lower procedural trauma. The animals then undergo a period of recovery lasting approximately 6-8 weeks and allowing the scar to fully remodel. For more details the interested reader should refer to [89]. The excision, dye loading and slicing of the heart would then follow a procedure almost identical to that described in Chapter 4. Optimisation of the vibratome settings would likely be required, as the density of within the ventricular block would be non-uniform due to the fibrotic microstructures intermixed with the healthy cardiac tissue. This will likely mean reducing the speed at which the blade is advanced from 0.3 mm/s to 0.1 mm/s (minimum setting on Leica VT1200 S vibratome), thus prolonging the slicing time three fold. Careful temperature maintenance is important to ensure the slices remain viable during this period.

Curiously, the standard treatment to prevent border zone arrythmias is catheter ablation of the fibrosis. This makes it more regular and homogenous in shape by ablating the healthy tissue, intentionally generating more scar to block abnormal conduction pathways [90]. Nevertheless this does not completely prevent re-entry arrythmias. Regenerative medicine approach, utilising organoids and spheroids grown from human

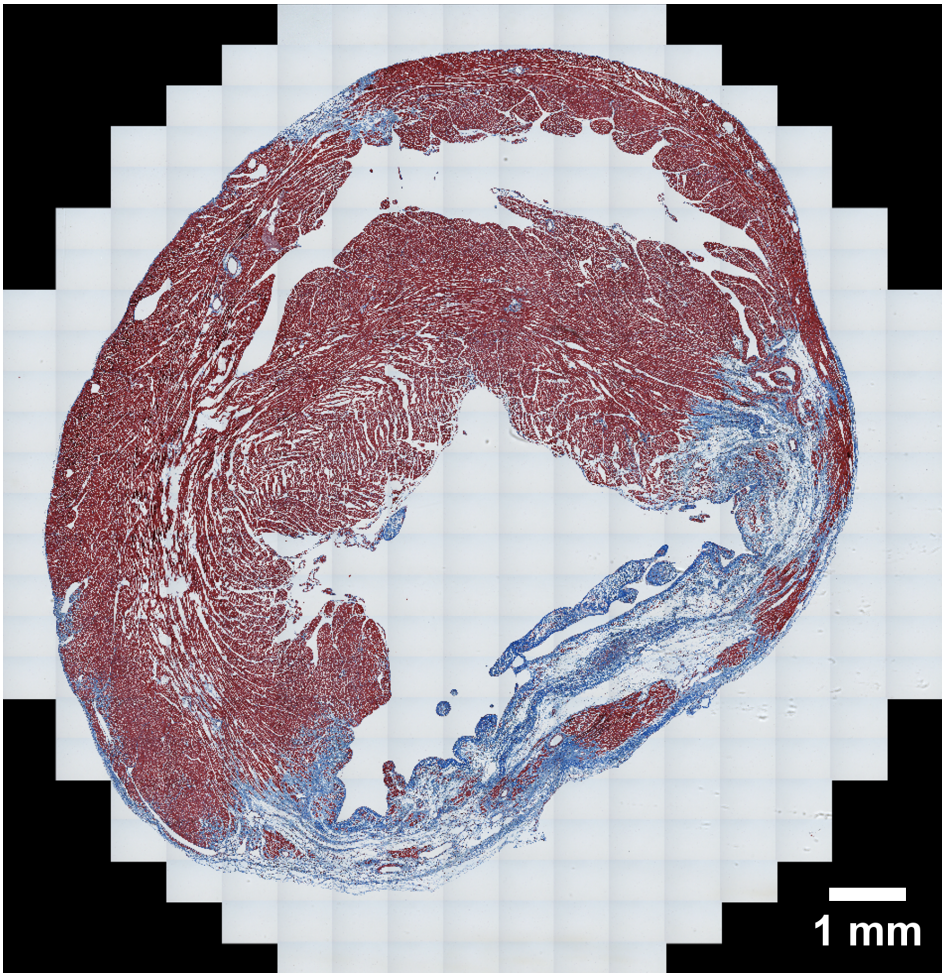

Figure 7.1: A histology assay of a cross section of an infarcted mouse heart. Masson's trichrome staining was facilitated to differentiate between collagen fibers and cardiac muscle. Post-MI scar tissue is highlighted in blue with the healthy cells visualised in red. The majority of the scar is located within the left ventricle wall and its distribution is chaotic with areas of healthy tissue intermixed with the fibrosis. *Histology assay example supplied by Prof. Godfrey Smith's laboratory.*

induced pluripotent stem cells proposes injection of such cardiac preparations into the border region following MI to aid the heart in recovery and prevent the development of arrythmogenic pathways. 2P-RF microscope could be used to first assess the electromechanical coupling after microinjection of such spheroids into healthy slices across all dimensions and then how they aid electrical propagation in infarcted preparations.

7.2.1 Precise structure assessment of optically cleared slices

The aforementioned studies could be further informed by correlative function - structure imaging. Visualisation and precise quantification of the post-MI fibrosis (e.g. volume, border zone area) is crucial to determine the impact of MI remodelling on electrical propagation which in turn will aid the development of diagnostic and therapeutic interventions. Quantitative assay of the slice structure the function of which was previously investigated with the 2P-RF system is essential to establish the cause-effect relationship. Histology is invasive and require tissue fixing and segmentation into slices of around 2 µm which yields artifacts. Ultrasound or magnetic resonance imaging does not have sufficient resolution for quantification of cellular precision.

On the other hand, optical clearing protocols could be applied on the cardiac slices, such as SHIELD or Clarity [91]. These tissue transformation based methods remove the lipid bi-layers within the cells, after covalent linking of proteins and nucleic acids to an acrylamide-based matrix, in the case of Clarity, and the use of a flexible epoxide to form multiple intra-molecular bonds in the case of SHIELD [91]. Both methods preserve structural integrity. Importantly, this selective and uniform lipid removal eradicates the refractive index mismatch and scattering, rendering the slices optically transparent as they are immersed in a refractive index matching medium. For a comparative study of SHIELD and Clarity protocols for to cardiac tissue clearing, the interested reader should refer to [91]. Importantly, when mounted appropriately, these cleared preparations can be imaged with a LSM, in particular, the open source mesoSPIM light sheet microscope in our laboratories [26]. This method allows cellular resolution without the need to further section the slices. Number of cells as well as cardiac fibre orientation can also be quantified [92]. With optical clearing of a post-MI slice after 2P-RF imaging, the function at the border zone could be correlated quantitatively to the structure of the fibrotic patch, aiding the understanding of electrical dysfunction which will aid the development and testing of new drugs and diagnostics.

	Refocusing frequency	Recommended RF range	Axial resolution (NA, excitation wavelength)	Pulse duration	Cost / availability of parts	Sample	Power transmission / power at sample
Rupprecht et al., (2016) [42]	6 Hz	300 µm	300 µm RR with axial FWHM <7 µm (1.0 NA)**	N/A	N/A, off-the-shelf parts	Calcium imaging in adult zebrafish brain (function)	N/A
Weissenburger et al., (2019) [39]	17 Hz	150 µm	15 µm at 0 RR (0.8 NA, 960 nm)	90 fs, not measured at sample	N/A	In vivo mouse cortex (function)	N/A
Sofroniew et al., (2016) [41]	N/A*	1 mm	approx. 4 µm through 800 µm RR range, >0.8 Strehl ratio over 400 µm range*** (970 nm)	106 fs at sample	N/A, custom RF optics, commercialised system	In vivo mouse cortex (function)	13%
Botcherby et al., (2012) [6]	<2.7 kHz (for 25 µm displacement)	200 µm	Strehl ratio >0.85across 200 µm range; measured FWHM of PSF not quoted, (0.8 NA, 850 nm)	100 fs, not measured at sample	NA, custom axial scanner	Murine cortical slab and slice preparations (function)	120 mW at back aperture of imaging lens
Botcherby et al., (2013) [8]						Langendorff perfused-rat heart (structure)	N/A
This work	<250 Hz (for 100 µm displacement)	100 µm	100 µm RR with under 5 µm axial resolution (1 NA, 800 nm)	156 fs at sample	<£9000, off-the-shelf parts	Living rabbit cardiac slices (function)	15.9% (22 mW)

Table 7.1: Comparison of the properties and performance of the 2P-RF system implemented in this work and published literature. N/A: not applicable or not explicitly stated in the study. *: the RF frequency was not quoted, however the VC actuator used was the same as in this work. **: the study presented two RF module configurations; these specifications are for configuration 2, where an additional relay telescope was introduced in the module. The specifications marked with *** are approximate and were obtained from Figure 4 in the publication.

7.3 Summary and conclusion

The 2P-RF system which was developed and characterised in Chapter 3 managed to achieve fast transmural cardiac structure imaging (Chapter 6). During functional imaging, longitudinal APs were still resolved albeit at a lower SNR with static remote refocusing, although the rapid transmural scan currently yields a negative result (Chapter 6). The current limitations on electrophysiology imaging include the etching of the remote mirror due to high power densities (and in turn the SNR achieved) as well as the voice coil scanning speed. If the system is modified so that more average power is available at the sample and a faster voice coil is used, AP propagation in both longitudinal and transmural directions could be probed under physiological conditions where the slices are heated and oxygenated. Correlative function-structure imaging could then be facilitated using optical clearing and light sheet imaging to infer cause-effect relationship between post-MI fibrosis and abnormal AP properties at the arrhythmia prone infarct-healthy myocardium border zone.

In Table 7.1, the quantitative metrics describing the performance of the remote refocusing module implemented in this work are compared to other published multiphoton-RF systems (static multiplane imaging microscopes [7, 40] are excluded from this com-

parison). The work in this Thesis therefore adds to the sparse literature on implementation of remote refocusing in multiphoton microscopy. As summarised in Table 7.1, the system built allows for refocusing frequency in the range of up to 250 Hz; the systems documented in [42] and [39] utilise RF at 6 Hz and 17 Hz, respectively. While the microscope developed in Botcherby et al., (2012 and 2013) allowed 2.7 kHz refocus, the scanner was custom built [6]; in the present study off-the-shelf Equipment Solutions VC actuator was chosen, increasing the accessibility of the system. The recommended effective remote refocusing range of this system was comparable, although shorter than the published systems (100 µm, considering we aim to maintain <5 µm axial resolution and avoid distortion, as discussed in Chapter 3, Sections 3.3 and 3.4). For example, the microscope in [5, 8] maintains acceptable performance (Strehl ratio >0.8 µm) over close to double our recommended range. Nevertheless, our system is operational for over 200 µm range (Figure 3.8), if degradation of optical resolution is to be accepted (<7 µm), comparable to the allowed range in [42] (300 µm). In [41], the largest RF range is achieved with 4 µm axial resolution maintained over close to 800 µm range of refocus. Nevertheless, custom-manufactured (JenOptik) microscope objective lens optics were used, increasing the price and complexity of the remote refocusing microscope presented. Attempts to measure the pulse duration at the sample are stated only in [41]; Other compared studies only present the laser output pulse specifications. Importantly, in this Thesis, the full optical design and a wide range of relevant operational parameters (average power at sample and pulse duration at sample) required for functional imaging and resolving action potential with remote refocusing in highly scattering native cardiac tissue samples are identified and documented. Most multiphoton-RF systems have been applied to study less scattering neural tissue [6, 39, 41], or zebrafish brain that is significantly less opaque [42]. The work in [8] details investigation of cardiac structure with 2P-RF microscope, which has less stringent requirements than resolving deep cardiac APs. In this work, the full and complete experimental pipeline from the preparation of acute cardiac slices to the subsequent 2P-RF imaging is established and detailed. To the best of our knowledge, the work in this Thesis is the furthest the application of remote refocusing in cardiac electrophysiology imaging has been advanced. Together with the implementation of RF module with off-the-shelf opto-mechanical parts, this work paves the way for successful implementation of transmural cardiac action potential tracing with remote refocusing.

References

[1] M. C. Müllenbroich *et al.*, "Novel Optics-Based Approaches for Cardiac Electrophysiology: A Review," *Frontiers in physiology*, vol. 12, no. Journal Article, pp. 769 586–769 586, 2021. DOI: 10.3389/fphys.2021.769586.

[2] W. W. Webb, W. R. Zipfel, and R. M. Williams, "Nonlinear magic: Multiphoton microscopy in the biosciences," *Nature biotechnology*, vol. 21, no. 11, pp. 1369–1377, 2003. DOI: 10.1038/nbt899.

[3] I. A. Ghouri, A. Kelly, F. L. Burton, G. L. Smith, and O. J. Kemi, "2-photon excitation fluorescence microscopy enables deeper high-resolution imaging of voltage and Ca2+in intact mice, rat, and rabbit hearts: Cardiac live 2-photon microscopy," *Journal of biophotonics*, vol. 8, no. Journal Article, pp. 112–123, 2013. DOI: 10.1002/jbio.201300109.

[4] E. J. Botcherby, R. Juškaitis, M. J. Booth, and T. Wilson, "An optical technique for remote focusing in microscopy," *Optics communications*, vol. 281, no. 4, pp. 880–887, 2008. DOI: 10.1016/j.optcom.2007.10.007.

[5] E. Botcherby, R. Juškaitis, M. Booth, and T. Wilson, "Aberration free refocusing for high numerical aperture microscopy," in *Proceedings of SPIE*, vol. 6861, SPIE, 2008, pp. 686 110–6 861 112. DOI: 10.1117/12.771419.

[6] E. J. Botcherby *et al.*, "Aberration-free three-dimensional multiphoton imaging of neuronal activity at kHz rates," *Proceedings of the National Academy of Sciences - PNAS*, vol. 109, no. 8, pp. 2919–2924, 2012. DOI: 10.1073/pnas.1111662109.

[7] K. T. Takasaki, D. Tsyboulski, and J. Waters, "Dual-plane 3-photon microscopy with remote focusing," *Biomedical optics express*, vol. 10, no. 11, pp. 5585–5599, 2019. DOI: 10.1364/BOE.10.005585.

[8] E. J. Botcherby *et al.*, "Fast Measurement of Sarcomere Length and Cell Orientation in Langendorff-Perfused Hearts Using Remote Focusing Microscopy," *Circulation research*, vol. 113, no. 7, pp. 863–870, 2013. DOI: 10.1161/CIRCRESAHA.113.301704.

[9] S. Akturk, X. Gu, M. Kimmel, and R. Trebino, "Extremely simple single-prism ultrashort- pulse compressor," *Optics express*, vol. 14, no. 21, pp. 10 101–10 108, 2006. DOI: 10.1364/OE.14.010101.

[10] S. A. Watson, M. Scigliano, I. Bardi, R. Ascione, C. M. Terracciano, and F. Perbellini, "Preparation of viable adult ventricular myocardial slices from large and small mammals," *Nature protocols*, vol. 12, no. 12, pp. 2623–2639, 2017. DOI: 10.1038/nprot.2017.139.

[11] *University of Glasgow - Research - Strategy and policies - Our policies - Openness in animal research [Online].*

[12] J. Mertz, "Fluorescence, Chapter 13," English, in *Introduction to optical microscopy*, Book, Whole, Second, Cambridge: Cambridge University Press, 2019, pp. 263–286.

[13] A. Ettinger and T. Wittmann, "Chapter 5 - Fluorescence live cell imaging," *Methods in cell biology*, vol. 123, no. Journal Article, pp. 77–94, 2014. DOI: 10.1016/B978-0-12-420138-5.00005-7.

[14] Y. Xiao, P. Deng, Y. Zhao, S. Yang, and B. Li, "Three-photon excited fluorescence imaging in neuroscience: From principles to applications," *Frontiers in neuroscience*, vol. 17, no. Journal Article, p. 1 085 682, 2023. DOI: 10.3389/fnins.2023.1085682.

[15] M. Göppert-Mayer, "Elementary processes with two quantum transitions," *Annalen der Physik*, vol. 18, no. 7-8, pp. 466–479, 2009. DOI: 10.1002/andp.200910358.

[16] W. Kaiser and C. G. B. Garrett, "Two-Photon Excitation in CaF2:Eu2," *Physical review letters*, vol. 7, no. Journal Article, pp. 229–231, 1961. DOI: 10.1103/physrevlett.7.229.

[17] W. Denk, J. H. Strickler, and W. W. Webb, "Two-Photon Laser Scanning Fluorescence Microscopy," *Science (American Association for the Advancement of Science)*, vol. 248, no. 4951, pp. 73–76, 1990. DOI: 10.1126/science.2321027.

[18] J. Platisa *et al.*, "High-speed low-light in vivo two-photon voltage imaging of large neuronal populations," *Nature methods*, vol. 20, no. 7, pp. 1095–1103, 2023. DOI: 10.1038/s41592-023-01820-3.

[19] J. Mertz, "Multiphoton Microscopy, Chapter 16.," in *Introduction to optical microscopy*, Second, Cambridge: Cambridge University Press, 2019, pp. 329–349.

[20] J. B. Pawley, "Multi-Photon Molecular Excitation in Laser-Scanning Microscopy, Chapter 28," in *Handbook of biological confocal microscopy*, Book, Whole, 3rd, New York, NY: Springer, 2006, pp. 535–549.

[21] J. D. Pickering, "Bandwidth and dispersion. Chapter 2.," English, in *Ultrafast lasers and optics for experimentalists*, Second, Bristol [England] (Temple Circus, Temple Way, Bristol BS1 6HG, UK): Institute of Physics Publishing, 2024.

[22] U. Keller, "Linear Pulse Propagation," in *Ultrafast Lasers: A Comprehensive Introduction to Fundamental Principles with Practical Applications*, Cham: Springer International Publishing, 2021, pp. 25–71. DOI: 10.1007/978-3-030-82532-4_2.

[23] E. Hecht, "More on Geometrical Optics. Aberrations, Chapter 6.3," in *Optics*, Book, Whole, 5 Global, Boston: Pearson Education, Inc, 2017, p. 253.

[24] K. SeungYeon, D. Martí, and C. B. Arnold, "Variable optical elements for fast focus control," *Nature photonics*, vol. 14, no. 9, pp. 533–542, 2020. DOI: 10.1038/s41566-020-0684-z.

[25] D. Koyama, R. Isago, and K. Nakamura, "Three-dimensional focus scanning by an acoustic variable-focus optical liquid lens," in *AIP Conference Proceedings*, AIP, 2012. DOI: 10.1063/1.4749368.

[26] F. F. Voigt *et al.*, "The mesoSPIM initiative: Open-source light-sheet microscopes for imaging cleared tissue," *Nature methods*, vol. 16, no. 11, pp. 1105–1108, 2019. DOI: 10.1038/s41592-019-0554-0.

[27] M. Žurauskas, O. Barnstedt, M. Frade-Rodriguez, S. Waddell, and M. J. Booth, "Rapid adaptive remote focusing microscope for sensing of volumetric neural activity," *Biomedical optics express*, vol. 8, no. 10, pp. 4369–4379, 2017. DOI: 10.1364/BOE.8.004369.

[28] W. J. Shain, N. A. Vickers, B. B. Goldberg, T. Bifano, and J. Mertz, "Extended depth-of-field microscopy with a high-speed deformable mirror," *Optics Letters*, vol. 42, no. 5, pp. 995–998, 2017. DOI: 10.1364/OL.42.000995.

[29] F. Anselmi, C. Ventalon, A. Bègue, D. Ogden, and V. Emiliani, "Three-dimensional imaging and photostimulation by remote-focusing and holographic light patterning," *Proceedings of the National Academy of Sciences - PNAS*, vol. 108, no. 49, pp. 19 504–19 509, 2011. DOI: 10.1073/pnas.1109111108.

[30] W. Hong *et al.*, "Adaptive light-sheet fluorescence microscopy with a deformable mirror for video-rate volumetric imaging," *Applied physics letters*, vol. 121, no. 19, p. 193 703, 2022. DOI: 10.1063/5.0125946.

[31] L. Dvinskikh, H. Sparks, K. T. MacLeod, and C. Dunsby, "High-speed 2D light-sheet fluorescence microscopy enables quantification of spatially varying calcium dynamics in ventricular cardiomyocytes," *Frontiers in physiology*, vol. 14, no. Journal Article, pp. 1 079 727–1 079 727, 2023. DOI: 10.3389/fphys.2023.1079727.

[32] L. Dvinskikh, H. Sparks, L. Brito, K. T. MacLeod, S. E. Harding, and C. Dunsby, "Remote-refocusing light-sheet fluorescence microscopy enables 3D imaging of electromechanical coupling of hiPSC-derived and adult cardiomyocytes in co-culture," *Scientific reports*, vol. 13, no. 1, pp. 3342–3342, 2023. DOI: 10.1038/s41598-023-29419-w.

[33] H. Sparks *et al.*, "Development a flexible light-sheet fluorescence microscope for high-speed 3D imaging of calcium dynamics and 3D imaging of cellular microstructure," *Journal of biophotonics*, vol. 13, no. 6, e201960239–n/a, 2020. DOI: 10.1002/jbio.201960239.

[34] M. Gintoli *et al.*, "Spinning disk-remote focusing microscopy," *Biomedical optics express*, vol. 11, no. 6, pp. 2874–2888, 2020. DOI: 10.1364/BOE.389904.

[35] S. Mohanan and A. D. Corbett, "Sensitivity of remote focusing microscopes to magnification mismatch," *Journal of microscopy (Oxford)*, vol. 288, no. 2, pp. 95–105, 2022. DOI: 10.1111/jmi.12991.

[36] A. D. Corbett *et al.*, "Quantifying distortions in two-photon remote focussing microscope images using a volumetric calibration specimen," *Frontiers in physiology*, vol. 5, no. Journal Article, pp. 384–384, 2014. DOI: 10.3389/fphys.2014.00384.

[37] W. Hong, H. Sparks, and C. Dunsby, "Alignment and characterization of remote-refocusing systems," *Applied Optics*, vol. 62, no. 28, pp. 7431–7440, 2023. DOI: 10.1364/AO.500281.

[38] B. Yang *et al.*, "Epi-illumination SPIM for volumetric imaging with high spatial-temporal resolution," *Nature methods*, vol. 16, no. 6, pp. 501–504, 2019. DOI: 10.1038/s41592-019-0401-3.

[39] S. Weisenburger *et al.*, "Volumetric Ca2+ Imaging in the Mouse Brain Using Hybrid Multiplexed Sculpted Light Microscopy," *Cell*, vol. 177, no. 4, 1050–1066.e14, 2019. DOI: 10.1016/j.cell.2019.03.011.

[40] E. Z. Chong, M. Panniello, I. Barreiros, M. M. Kohl, and M. J. Booth, "Quasi-simultaneous multiplane calcium imaging of neuronal circuits," *Biomedical optics express*, vol. 10, no. 1, pp. 267–282, 2019. DOI: 10.1364/BOE.10.000267.

[41] N. J. Sofroniew, D. Flickinger, J. King, and K. Svoboda, "A large field of view two-photon mesoscope with subcellular resolution for in vivo imaging," *eLife*, vol. 5, no. Journal Article, 2016. DOI: 10.7554/eLife.14472.

[42] P. Rupprecht, A. Prendergast, C. Wyart, and R. W. Friedrich, "Remote z-scanning with a macroscopic voice coil motor for fast 3D multiphoton laser scanning microscopy," *Biomedical optics express*, vol. 7, no. 5, pp. 1656–1671, 2016. DOI: 10.1364/BOE.7.001656.

[43] Urs L. Böhm and Benjamin Judkewitz, "Fast and light efficient remote focusing for volumetric voltage imaging," *bioRxiv*, p. 2023.11.28.568783, Jan. 2023. DOI: 10.1101/2023.11.28.568783.

[44] C. Dunsby, "Optically sectioned imaging by oblique plane microscopy," English, *Optics express*, vol. 16, no. 25, pp. 20 306–20 316, 2008, Place: United States. DOI: 10.1364/OE.16.020306.

[45] M. B. Sikkel *et al.*, "High speed sCMOS-based oblique plane microscopy applied to the study of calcium dynamics in cardiac myocytes," English, *Journal of biophotonics*, vol. 9, no. 3, pp. 311–323, 2016, Place: Weinheim Publisher: WILEY-VCH Verlag. DOI: 10.1002/jbio.201500193.

[46] S. Kumar, D. Wilding, M. B. Sikkel, A. R. Lyon, K. T. MacLeod, and C. Dunsby, "High-speed 2D and 3D fluorescence microscopy of cardiac myocytes," English, *Optics express*, vol. 19, no. 15, pp. 13 839–13 847, 2011, Place: United States. DOI: 10.1364/OE.19.013839.

[47] B. Yang *et al.*, "DaXi-high-resolution, large imaging volume and multi-view single-objective light-sheet microscopy," *Nature methods*, vol. 19, no. 4, pp. 461–469, 2022. DOI: 10.1038/s41592-022-01417-2.

[48] G. Sirinakis, E. S. Allgeyer, D. Nashchekin, and D. St Johnston, "User-friendly oblique plane microscopy on a fully functional commercially available microscope base," *Biomedical optics express*, vol. 15, no. 4, pp. 2358–2376, 2024. DOI: 10.1364/BOE.518856.

[49] Wapcaplet, *Diagram of the human heart [Online]*, Jun. 2006.

[50] A. J. Pappano and W. Gil Wier, "1 - Overview of the Circulation and Blood," in *Cardiovascular Physiology (Tenth Edition)*, A. J. Pappano and W. Gil Wier, Eds., Philadelphia: Elsevier, Jan. 2013, pp. 1–9. DOI: 10.1016/B978-0-323-08697-4.00001-0.

[51] OpenStax, *Cardiac Muscle. OpenStax book 'Anatomy and Physiology', Figure 10.22*, Apr. 2022.

[52] OpenStax, *The T-Tubule. OpenStax book 'Anatomy and Physiology', Figure 10.7*, Apr. 2022.

[53] V. Jana, *Electrical conduction system of the heart [Online]*, May 2022.

[54] A. J. Pappano and W. Gil Wier, "2 - Excitation: The Cardiac Action Potential," in *Cardiovascular Physiology (Tenth Edition)*, A. J. Pappano and W. Gil Wier, Eds., Philadelphia: Elsevier, Jan. 2013, pp. 11–30. DOI: 10.1016/B978-0-323-08697-4.00002-2.

[55] D. M. Bers, "Cardiac excitation-contraction coupling," *Nature (London)*, vol. 415, no. 6868, pp. 198–205, 2002. DOI: 10.1038/415198a.

[56] V. Biasci *et al.*, "Optogenetic manipulation of cardiac electrical dynamics using sub-threshold illumination: Dissecting the role of cardiac alternans in terminating rapid rhythms," *Basic research in cardiology*, vol. 117, no. 1, pp. 25–25, 2022. DOI: 10.1007/s00395-022-00933-8.

[57] I. A. Ghouri *et al.*, "Characterization of Electrical Activity in Post-myocardial Infarction Scar Tissue in Rat Hearts Using Multiphoton Microscopy," *Frontiers in physiology*, vol. 9, no. Journal Article, p. 1454, 2018. DOI: 10.3389/fphys.2018.01454.

[58] S. Salerno, K. Garten, G. L. Smith, T. Stølen, and A. Kelly, "Two-photon excitation of FluoVolt allows improved interrogation of transmural electrophysiological function in the intact mouse heart," *Progress in biophysics and molecular biology*, vol. 154, no. Journal Article, pp. 11–20, 2020. DOI: 10.1016/j.pbiomolbio.2019.08.007.

[59] E. Z. Chong, T. F. Watson, and F. Festy, "Autocorrelation measurement of femtosecond laser pulses based on two-photon absorption in GaP photodiode," *Applied physics letters*, vol. 105, no. 6, p. 062 111, 2014. DOI: 10.1063/1.4893423.

[60] M. N. Polyanskiy, "Refractiveindex.info database of optical constants," en, *Scientific Data*, vol. 11, no. 1, p. 94, Jan. 2024. DOI: 10.1038/s41597-023-02898-2.

[61] A. M. Bill Black Mike Lopez, *Basics of Voice Coil Actuators*, Jul. 1993.

[62] S. W. Teare and Society of Photo-optical Instrumentation Engineers, "Proportional-Integral-Derivative Controllers, Chapter 10.," in *Practical electronics for optical design and engineering*, Book, Whole, vol. TT 107;TT107.; Bellingham, Washington: SPIE Press, 2016. DOI: 10.1117/3.2243367.

[63] F. G. Pitoulis, S. A. Watson, F. Perbellini, and C. M. Terracciano, "Myocardial slices come to age: An intermediate complexity in vitro cardiac model for translational research," *Cardiovascular research*, vol. 116, no. 7, pp. 1275–1287, 2020. DOI: 10.1093/cvr/cvz341.

[64] S. A. Watson, C. M. Terracciano, and F. Perbellini, "Myocardial Slices: An Intermediate Complexity Platform for Translational Cardiovascular Research," *Cardiovascular drugs and therapy*, vol. 33, no. 2, pp. 239–244, 2019. DOI: 10.1007/s10557-019-06853-5.

[65] P. Montero *et al.*, "Cells, Materials, and Fabrication Processes for Cardiac Tissue Engineering," *Frontiers in bioengineering and biotechnology*, vol. 8, no. Journal Article, pp. 955–955, 2020. DOI: 10.3389/fbioe.2020.00955.

[66] L. M. Loew, "Potentiometric dyes: Imaging electrical activity of cell membranes," *Pure and applied chemistry*, vol. 68, no. 7, pp. 1405–1409, 1996. DOI: 10.1351/pac199668071405.

[67] E. W. Miller, J. Y. Lin, E. P. Frady, P. A. Steinbach, W. B. J. Kristan, and R. Y. Tsien, "Optically monitoring voltage in neurons by photo-induced electron transfer through molecular wires," *Proceedings of the National Academy of Sciences - PNAS*, vol. 109, no. 6, pp. 2114–2119, 2012. DOI: 10.1073/pnas.1120694109.

[68] D. A. Rusakov, "Avoiding bias in fluorescence sensor readout," English, *Nature reviews. Neuroscience*, vol. 25, no. 1, pp. 1–2, 2024. DOI: 10.1038/s41583-023-00768-9.

[69] K. Wang *et al.*, "Cardiac tissue slices: Preparation, handling, and successful optical mapping," *American journal of physiology. Heart and circulatory physiology*, vol. 308, no. 9, H1112, 2015. DOI: 10.1152/ajpheart.00556.2014.

[70] X. Cao-Ehlker *et al.*, "Optimized Conditions for the Long-Term Maintenance of Precision-Cut Murine Myocardium in Biomimetic Tissue Culture," *Bioengineering*, vol. 10, no. 2, p. 171, 2023. DOI: 10.3390/bioengineering10020171.

[71] E. Huethorst *et al.*, "Conventional rigid 2D substrates cause complex contractile signals in monolayers of human induced pluripotent stem cell-derived cardiomyocytes," *The Journal of physiology*, vol. 600, no. 3, pp. 483–507, 2022. DOI: 10.1113/JP282228.

[72] M. P. Hortigon-Vinagre, V. Zamora, F. L. Burton, J. Green, G. A. Gintant, and G. L. Smith, "The Use of Ratiometric Fluorescence Measurements of the Voltage Sensitive Dye Di-4-ANEPPS to Examine Action Potential Characteristics and Drug Effects on Human Induced Pluripotent Stem Cell-Derived Cardiomyocytes," *Toxicological sciences*, vol. 154, no. 2, pp. 320–331, 2016. DOI: 10.1093/toxsci/kfw171.

[73] L. Sala *et al.*, "MUSCLEMOTION: A Versatile Open Software Tool to Quantify Cardiomyocyte and Cardiac Muscle Contraction In Vitro and In Vivo," *Circulation research*, vol. 122, no. 3, e5–e16, 2018. DOI: 10.1161/CIRCRESAHA.117.312067.

[74] V. E. Bondarenko and R. L. Rasmusson, "Transmural heterogeneity of repolarization and Ca2+ handling in a model of mouse ventricular tissue," *American journal of physiology. Heart and circulatory physiology*, vol. 299, no. 2, H454, 2010. DOI: 10.1152/ajpheart.00907.2009.

[75] G. Iachetta, G. Melle, N. Colistra, F. Tantussi, F. De Angelis, and M. Dipalo, "Long-term in vitro recording of cardiac action potentials on microelectrode arrays for chronic cardiotoxicity assessment," *Archives of Toxicology*, vol. 97, no. 2, pp. 509–522, 2023. DOI: 10.1007/s00204-022-03422-y.

[76] S. Sicouri and C. Antzelevitch, "A Subpopulation of Cells With Unique Electrophysiological Properties in the Deep Subepicardium of the Canine Ventricle: The M Cell," *Circulation research*, vol. 68, no. 6, pp. 1729–1741, 1991. DOI: 10.1161/01.RES.68.6.1729.

[77] M. N. Hicks and S. M. Cobbe, "Effect of glibenclamide on extracellular potassium accumulation and the electrophysiological changes during myocardial ischaemia in the arterially perfused interventricular septum of rabbit," *Cardiovascular research*, vol. 25, no. 5, pp. 407–413, 1991. DOI: 10.1093/cvr/25.5.407.

[78] J. M. Di Diego, S. Sicouri, R. C. Myles, F. L. Burton, G. L. Smith, and C. Antzelevitch, "Optical and electrical recordings from isolated coronary-perfused ventricular wedge preparations," *Journal of molecular and cellular cardiology*, vol. 54, no. Journal Article, pp. 53–64, 2013. DOI: 10.1016/j.yjmcc.2012.10.017.

[79] B. Choi and G. Salama, "Simultaneous maps of optical action potentials and calcium transients in guinea-pig hearts: Mechanisms underlying concordant alternans," *The Journal of physiology*, vol. 529, no. 1, pp. 171–188, 2000. DOI: 10.1111/j.1469-7793.2000.00171.x.

[80] P. Lee, P. Yan, P. Ewart, P. Kohl, L. M. Loew, and C. Bollensdorff, "Simultaneous measurement and modulation of multiple physiological parameters in the isolated heart using optical techniques," *Pflügers Archiv*, vol. 464, no. 4, pp. 403–414, 2012. DOI: 10.1007/s00424-012-1135-6.

[81] A. Klimas, G. Ortiz, S. C. Boggess, E. W. Miller, and E. Entcheva, "Multimodal on-axis platform for all-optical electrophysiology with near-infrared probes in human stem-cell-derived cardiomyocytes," *Progress in biophysics and molecu-*

lar biology, vol. 154, no. Journal Article, pp. 62–70, 2020. DOI: 10.1016/j.pbiomolbio.2019.02.004.

[82] B. Cathey *et al.*, "Open-Source Multiparametric Optocardiography," *Scientific reports*, vol. 9, no. 1, pp. 721–721, 2019. DOI: 10.1038/s41598-018-36809-y.

[83] C. O'Shea *et al.*, "Cardiac optical mapping – State-of-the-art and future challenges," *The international journal of biochemistry & cell biology*, vol. 126, no. Journal Article, pp. 105 804–105 804, 2020. DOI: 10.1016/j.biocel.2020.105804.

[84] F. Helmchen and W. Denk, "Deep tissue two-photon microscopy," *Nature methods*, vol. 2, no. 12, pp. 932–940, 2005. DOI: 10.1038/nmeth818.

[85] V. E. Centonze and J. G. White, "Multiphoton Excitation Provides Optical Sections from Deeper within Scattering Specimens than Confocal Imaging," *Biophysical journal*, vol. 75, no. 4, pp. 2015–2024, 1998. DOI: 10.1016/S0006-3495(98)77643-X.

[86] D McGloin and K Dholakia, "Bessel beams: Diffraction in a new light," *Contemporary Physics*, vol. 46, no. 1, pp. 15–28, Jan. 2005.

[87] R. Lu *et al.*, "Video-rate volumetric functional imaging of the brain at synaptic resolution," *Nature neuroscience*, vol. 20, no. 4, pp. 620–628, 2017. DOI: 10.1038/nn.4516.

[88] E. Huethorst, "Development of small, engineered heart tissues and their acute response to implantation," PhD Thesis, University of Glasgow, Feb. 2022.

[89] M. Freeman *et al.*, "A novel method for the percutaneous induction of myocardial infarction by occlusion of small coronary arteries in the rabbit," *American journal of physiology. Heart and circulatory physiology*, vol. 326, no. 3, H735–H751, 2024. DOI: 10.1152/ajpheart.00657.2023.

[90] J. W. Holmes, Z. Laksman, and L. Gepstein, "Making better scar: Emerging approaches for modifying mechanical and electrical properties following infarction and ablation," *Progress in biophysics and molecular biology*, vol. 120, no. 1-3, pp. 134–148, 2016. DOI: 10.1016/j.pbiomolbio.2015.11.002.

[91] C. Olianti *et al.*, "Optical clearing in cardiac imaging: A comparative study," *Progress in biophysics and molecular biology*, vol. 168, no. Journal Article, pp. 10–17, 2022. DOI: 10.1016/j.pbiomolbio.2021.07.012.

[92] F. Giardini *et al.*, "Dissecting the role of structural remodeling on trans-scar conduction in arrhythmogenic mouse hearts by advanced optical methods," *Biophysical journal*, vol. 123, no. 3, 435a–435a, 2024. DOI: 10.1016/j.bpj.2023.11.2633.